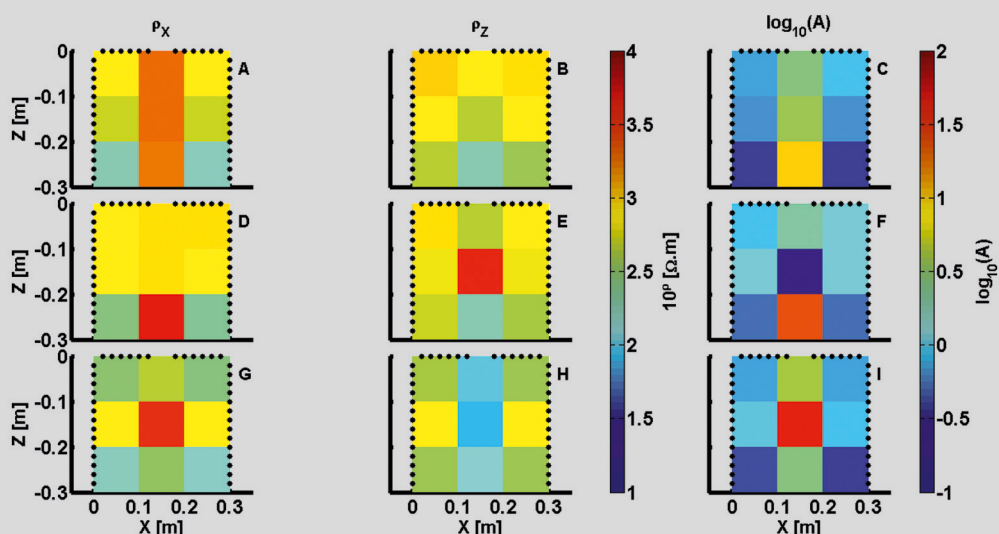# Using the anisotropy of electrical properties for the characterization of sedimentological structures and preferential flow processes

Sadam Al-Hazaimay

JÜLICH
FORSCHUNGSZENTRUM

Using the anisotropy of electrical properties for the characterization of sedimentological structures and preferential flow processes

Sadam Al-Hazaimay

Acknowledgment

I owe my gratitude to all the people who have made this thesis possible and because of whom my graduate experience has been one that I will cherish forever.

First and foremost, I'd like to thank my supervisor, Prof. Dr. Johan A. Huisman for giving me an invaluable opportunity to work on challenging and extremely interesting project over the past years. He has always made himself available for help and advice and there has never been an occasion when I've knocked on his door and he hasn't given me time. It has been a pleasure to work with and learn from such an extraordinary individual. I gratefully acknowledge Prof. Dr. Jan van der Kruk that he accepts being my promoter at the RWTH Aachen university. I would like to deeply thank Prof. Dr. Andreas Kemna for being part of my examination board.

My colleagues at the Institute of Bio- and Geosciences (IBG3, Agrosphere) in Forschungszentrum Jülich have enriched my graduate life in many ways and deserve a special mention. My interaction with Dr. Khan Zaib Jadoon, Dr. Anja Klotzsche, Matthias Kelter, Odilia Esser and Dr. Egon Zimmermann and his team from Das Zentralinstitut für Engineering, Elektronik und Analytik (ZEA2) has been very fruitful and helpful. Special thanks go to Jürgen Meyhöfer for helping with the german text translation.

I would like to acknowledge financial support from the Transregional Collaborative Research Centre (TR32) of the Deutsche Forschungs Gemeinschaft (DFG), for all the projects discussed herein. I would like to thank SIBELCO Deutschland GmbH for providing the clay material.

I owe my deepest thanks to my family - my mother SETA, and my father HUSSEIN, who have always stood by me and guided me through my career, and have pulled me through against impossible odds at times. Words cannot express the gratitude I owe them. I am very thankful to my brothers Ali, Firas, Mohammad, Yousef, and Suliman, and sisters Kawthar, Muna, Enas, and Nassem for their care. My nephews and nieces for their funny conversations. I thank my family very deeply for their supports and love and I will always appreciate all they have done.

I will not forget my friends, either whom I knew in Germany or in Jordan for their friendship and support. Our scientific dialogues, funny conversations, and interesting situations we created day by day, have made me feel at home. It is impossible to remember all, and I apologize to those I've inadvertently left out. Lastly, thank you all and thank ALLAH!

Abstract

Detailed information about subsurface structures (e.g. layering) and processes (e.g. flow and solute transport) in the vadose zone is important for the characterization and protection of soil and groundwater. Unfortunately, such information is not easily accessible due to the complexity of the soil system that exhibits considerable spatial variation in subsurface structure, which introduces significant uncertainty when attempting to improve system understanding. Because of layering structures and macropores in the subsurface, significant changes in soil properties appear in horizontal and vertical directions that introduce anisotropy in soil properties such as the hydraulic conductivity and the electrical resistivity. The premise of this thesis is that anisotropy in electrical resistivity can be used to extract meaningful information about other soil characteristics and properties. In particular, we investigate whether the anisotropy in electrical properties can be used to obtain information about the heterogeneity of sediment structures and macropore preferential flow processes using non-invasive geophysical techniques because such information is hard to obtain in field applications using classical destructive methods.

Synthetic modelling has shown that information on soil heterogeneity can be obtained from the anisotropy in electrical resistivity. In particular, it was shown that the correlation length ratio of bimodal facies distribution of two isotropic materials with different complex resistivity can be inversely estimated from the effective complex electrical resistivity in two directions (i.e. the anisotropy). In this thesis, this result from a synthetic modelling study was experimentally validated using complex electrical resistivity measurements on a measurement cell with two bimodal sediment distributions that differ in the fraction and spatial arrangement of each material. The effective complex electrical resistivity in the mHz to kHz frequency range of these two sediment distributions was determined using a novel analysis approach. To estimate the correlation length ratio, we used a global optimization method that minimized the difference between measured and modelled effective electrical resistivity. Effective complex electrical resistivity measurements of heterogeneous distributions showed a good agreement with the results obtained in the synthetic study for the same distributions, although measurement results were very sensitive to the sample thickness that was difficult to control. It was concluded that the electrical anisotropy in resistivity can indeed be used to obtain information about the heterogeneity in sediments with a very high accuracy in correlation length ratio, volume fraction, and the electrical parameters of the Cole-Cole model.

Macropores play a major role in contaminant transport from the surface through the vadose zone to the groundwater. Therefore, it is crucial to obtain information about macropore preferential flow and to improve our ability to characterize flow processes in macropores. In this thesis, we evaluated whether changes in electrical anisotropy in resistivity can be used to identify the existence of macropore

flow processes using direct measurements of resistivity in horizontal and vertical direction and electrical imaging. In a first step, we performed simulations and measurements to determine the electrical anisotropy in resistivity associated with water infiltration in an artificial macropore within the middle of a soil column. In the simulations, water content distributions were simulated using a 3D axisymmetric water flow model and then converted to electrical resistivity distributions to obtain the temporal development of effective electrical resistivity in horizontal and vertical direction. Both simulations and measurements showed very strong dynamic changes in electrical anisotropy due to water infiltration in the macropore and clearly highlighted that electrical anisotropy can be used to identify macropore preferential flow processes. The observed and modelled dynamical changes in the electrical anisotropy agreed well with each other, but deviated from expectations based on available simple conceptual models because the chosen electrode arrangement does not allow a correct determination of the effective horizontal and vertical electrical resistivity. Since this can only be overcome by the use of an imaging framework, in a next step it was explored whether time-lapse anisotropic electrical imaging can provide valuable information with high resolution in space and time to analyze preferential flow processes. For this, an artificial 2D macropore was created in a Hele-Shaw tank with electrodes. Electrical measurements were made using a novel fast ERT system that provided 10 images per second. An anisotropic inversion code was used to invert the electrical measurements using coarse cells that are bigger than the size of the macropore in correspondence with field applications where macropore flow processes cannot be resolved either. This resulted in images of macroscopic anisotropy in electrical resistivity with a high temporal resolution, and these were used to analyze the temporal dynamics of electrical anisotropy of inversion cells with and without water infiltration in macropores. It was found that the anisotropy showed strong dynamical reactions to water infiltration for cells with macropores that matched well with expected behavior, whereas almost no response was observed for cells without macropores. However, the size of the inversion cells affected the imaging results. Overall, this study showed that electrical anisotropy is useful to characterize subsurface structures and processes.

Zusammenfassung

Detaillierte Informationen über Untergrundstrukturen, Fliess- und Stofftransport-prozesse in der ungesättigten Zone sind für die Charakterisierung des Bodens und der Erhaltung der Grundwasserqualität unerlässlich. Jedoch sind solche Informationen nur schwer erfassbar. Dies liegt vor allem an der Komplexität des Bodensystems, welches ein erhebliches Maß an räumlicher Variabilität der Untergrundstruktur aufweist und damit das Erlangen von Systemverständnis stark erschwert. Die heterogenen Untergrundstrukturen, z.B. aufgrund von Schichtungen oder Makroporen, führen zu anisotropen Bodeneigenschaften, die erheblich unterschiedliche hydraulische und elektrische Leitfähigkeiten in horizontaler und vertikaler Richtung aufweisen können. In dieser Arbeit soll untersucht werden, welche charakteristischen Bodeneigenschaften aus der messbaren Anisotropie des elektrischen Widerstands gewonnen werden können. Im Besonderen soll untersucht werden, ob die Messung der anisotropen elektrischen Eigenschaften mittels nichtinvasiver geophysikalischer Methoden geeignet ist, um Information über die Heterogenität von Sedimentstrukturen und präferentiellen Fliessprozessen in Makroporen zu bestimmen. Diese Informationen können bislang nur schwer auf der Feldskala und nur mit destruktiven Methoden gewonnen werden.

In Vorarbeiten wurde mittels numerischer Modellierung gezeigt, dass eine Korrelation zwischen der Anisotropie des elektrischen Widerstands und der Bodenheterogenität besteht. Insbesondere ergab sich, dass das Korrelationslängenverhältnis bimodaler Verteilungen, bestehend aus zwei isotropen Materialien mit unterschiedlichen komplexen elektrischen Widerständen, mittels elektrischer Anisotropiemessungen bestimmt werden kann. Dazu wurde der effektive komplexe elektrische Widerstand zwei orthogonaler Richtungen bestimmt. Das oben erläuterte Ergebnis der numerischen Studie wurde in dieser Arbeit anhand von Messungen des komplexen elektrischen Widerstands in einer Messzelle mit zwei bimodalen Sedimentstrukturen, welche sich im Mischungsverhältnis und in der räumlichen Anordnung der verwendeten Materialien unterschieden, experimentell bestätigt. Der effektive komplexe elektrische Widerstand dieser zwei Sedimentverteilungen wurde mit einem neuartigen, speziell angepassten Verfahren im Frequenzbereich von einigen mHz bis zu einigen kHz gemessen. Um das Korrelationslängenverhältnis zu bestimmen, wurde ein globaler Optimierungsansatz verwendet, welcher die Differenz zwischen den gemessenen und den modellierten frequenzabhängigen effektiven komplexen elektrischen Widerständen minimiert. Die gemessenen effektiven komplexen elektrischen Widerstände dieser heterogenen Strukturen zeigten eine gute Übereinstimmung mit den Ergebnissen der numerischen Modellierung, wobei insbesondere die Probendicke, die in der verwendeten Messzelle nur schwer zu kontrollieren war, einen großen Einfluss auf die Messdaten hatte. Diese Ergebnisse bestätigen die Annahme, dass die messbare elektrische Anisotropie genutzt werden kann, um die Heterogenität von Sedimentstrukturen mit einer hohen Genauigkeit im Hinblick auf das Korrela-

tionslängenverhältnis, dem Volumenanteil, als auch die elektrischen Parameter des Cole-Cole Modells zu bestimmen.

Zusätzlich zur Schichtung haben auch Makroporen einen nicht vernachlässigbaren Einfluss beim Schadstofftransport von der Oberfläche durch die ungesättigte Zone in das Grundwasser. Daher ist es wichtig, diese präferentiellen Flüsse zu identifizieren und zu charakterisieren. In dieser Arbeit wurde folglich untersucht, ob Fliessprozesse in Makroporen mittels kontinuierlicher Messung der elektrischen Anisotropie in horizontaler und vertikaler Richtung, sowie mittels elektrischer Widerstandstomographie erkannt werden können. In einem ersten Schritt wurde eine Infiltration in eine künstliche Makropore im Zentrum einer Bodensäule simuliert und experimentell durchgeführt. Die Wassergehaltsverteilungen in der Säule wurden in einem dreidimensionalen achsensymmetrischen Wasserflussmodell modelliert und in elektrische Widerstandsverteilungen konvertiert, um die zeitliche Entwicklung des effektiven elektrischen Widerstands in horizontaler und vertikaler Richtung zu erhalten. Simulation und Messung zeigten beide sehr starke dynamische Änderungen der elektrischen Anisotropie durch die Infiltration in die Makropore, was demonstriert, dass die elektrische Anisotropie zur Identifikation präferentieller Flüsse in Makroporen geeignet ist. Die beobachteten und modellierten dynamischen Änderungen der elektrischen Anisotropie stimmten sehr gut überein, zeigten aber signifikante Abweichungen vom verfügbaren vereinfachten konzeptionellen Modell, da die verwendete Elektrodenanordnung keine korrekte Bestimmung der effektiven horizontalen und vertikalen Impedanz erlaubte. Um diese Problematik zu umgehen, wurde in einem weiteren Schritt untersucht ob kontinuierliche Messungen des anisotropen komplexen Widerstandes mittels elektrischer Widerstandstomographie eine räumlich und zeitlich hochauflösende Detektion von präferentiellen Fliessprozessen ermöglicht. Für diese Messungen wurde eine künstliche Makropore in einer Hele-Shaw-Zelle mit seitlich angebrachten Elektroden realisiert. Die elektrischen Messungen wurden mit einer neuartigen, schnellen ERT-Datenerfassung durchgeführt, welche mit der gewählten Konfiguration 10 Bilder pro Sekunde speicherte. Zur Rekonstruktion der Anisotropie wurde ein Inversionscode verwendet, welcher die intrinsische Anisotropie des elektrischen Widerstands berücksichtigt. Um Feldanwendungen zu simulieren, bei dem Makroporen-Prozesse nicht im Einzelnen aufgelöst werden können, wurde ein grobes Gitter verwendet, dessen Zellen deutlich größer waren als die Größe der Makropore. Diese Untersuchungen lieferten zeitlich hochauflösende Bilder der makroskopischen Anisotropie des elektrischen Widerstands, welche im Hinblick auf die zeitliche Dynamik der elektrischen Anisotropie der einzelnen Gitterzellen analysiert wurden. Die Ergebnisse zeigten, dass wie erwartet die elektrische Anisotropie nur für Zellen mit Makroporenanteil starke dynamische Reaktionen auf die Infiltration bewirkten, während Zellen ohne Makroporenanteil kaum Änderungen in der elektrischen Anisotropie aufwiesen. Jedoch sollte erwähnt werden, dass die Größe der Zellen einen starken Einfluss auf die Ergebnisse der elektrischen Bildgebung hatte. Zusammenfassend zeigen die Ergebnisse dieser Studie, dass die Messung der elektrische Anisotropie ein hilfreiches Werkzeug zur Bestimmung der Untergrundstrukturen und präferentiellen Fliessprozesse darstellt.

Table of Contents

List of Figures

List of Tables

List of Abbreviations

GPR   ground penetrating radar
ERT   electrical resistivity tomography
BTC   breakthrough curves
EIT   electrical impedance tomography
SIP   spectral induced polarization
NaCl   sodium chloride
FEM   finite element method
SISim   sequential indicator simulation
GSLib   geostatistical software library
SCE   shuffled complex evolution
OF   objective function
PMMA   poly(methyl methacrylate)
MvG   mualem van genuchten
TDR   time domain reflectometry

Chapter 1

INTRODUCTION

1.1 General Introduction

Improved characterization of soil heterogeneity and macropore preferential flow is important to better understand a range of key processes in the hydrologic cycle, such as overland flow, infiltration into the soil, evaporation to the atmosphere, and transpiration by plants. Accurate predictions of both flow and solute transport processes in the vadose zone are required to appropriately address problems of groundwater contamination and to predict the replenishment of limited groundwater resources. Therefore, it is of utmost importance to quantitatively characterize heterogeneity in soil and sediment properties. Furthermore, water and solutes can quickly bypass the vadose zone through macropores, although these macropores occupy only a small volume fraction in the vadose zone. Many efforts have been made to improve understanding of macropore preferential flow processes, but unfortunately most standard methods to investigate macropores are destructive and thus do not allow *in situ* monitoring of flow processes associated with macropores. However, such detailed information of these processes is needed to better understand, plan, and regulate hydrological and agricultural activities, especially when dealing with potentially harmful chemicals that can be transported alongside water.

1.2 Literature Background

1.2.1 *Heterogeneity in Subsurface Structures*

To properly describe flow and transport in soil and groundwater systems, it is important to quantitatively characterize heterogeneity in soil and sediment prop-

erties. A wide range of studies has dealt with this heterogeneity, and different methods have been used to characterize heterogeneity (e.g. Alexander et al., 2011; de Marsily et al., 2005; Illman et al., 2012; Teles et al., 2006). These methods include genetic, geostatistical, and Boolean approaches. In genetic modelling, it is attempted to obtain realistic descriptions of heterogeneity by modelling sedimentation processes. For example, Jacod and Joathon (1971) developed a genetic model to describe the evolution of sedimentary processes and considered a wide range of factors determining sedimentation (e.g. depth, distance from the source, subsidence, and nature of sediments). Teles et al. (2004) also characterized heterogeneity of alluvial media using genetic methods. In geostatistical analysis, two-point or multi-point statistics are used to describe heterogeneity. In case of the commonly used two-point statistics, heterogeneity is summarized by the spatial covariance function calculated from continuous or categorical data (see e.g. Ahmed and de Marsily, 1987; Dai et al., 2005; Goovaerts, 2001; Johnson, 1995; Ritzi, 2000; Teles et al., 2004). Boolean or Markovian models are used to describe discontinuous facies models where upscaling or averaging is required to describe this discontinuity in space. It has commonly been applied to describe heterogeneity in permeability and hydraulic conductivity (Fogg et al., 1998; Renard and de Marsily, 1997).

Stochastic modelling of soil and groundwater systems has developed into a large research field in the past decades. In particular, hydrogeologists have been strongly interested in stochastic descriptions of heterogeneous aquifers (Cacas et al., 1990a,b; Carrera, 1993; Dagan, 1982, 1985). For instance, perturbation-based spectral theory was used to relate aquifer heterogeneity of hydraulic conductivity to head variance, effective conductivity tensors, and macrodispersivity tensors. Although this approach proved to be robust for saturated flow problems, significant issues remain for more complicated systems or processes, such as unsaturated media, strongly heterogeneous media, and multiphase flow (Gelhar, 1986). More recently, stochastic upscaling has been used together with geostatistical simulations to describe hydraulic conductivity (Bierkens and van der Gaast, 1998; Wen and Gómez-Hernández, 1996; Yeh, 1992). Although stochastic hydrologists have been able to explain some key phenomena observed in the field, the success of this type of analysis hinges on detailed measurements of relevant aquifers properties to estimate the spatial covariance functions used to describe heterogeneity.

In an attempt to directly characterize heterogeneity, geophysical methods are increasingly being used. For instance, GPR data have been used to obtain information on aquifer heterogeneity by direct estimation of the correlation length from

radar images (Bayer et al., 2011; Comunian et al., 2011; Knight, 2001; Knight et al., 2004; Rea and Knight, 1998). Recently, Klotzsche et al. (2012) obtained high-resolution images of dielectric permittivity and electrical conductivity of a gravel aquifer using cross-hole GPR data. Using their full-waveform inversion approach, they were able to identify connected sedimentary structures that caused preferential flow. Time-lapse ERT has also been used to monitor flow and transport in aquifers. For example, solute BTC across a control plane have been measured using ERT, and these BTC were used to estimate the mean and variance of the hydraulic conductivity (Kemna et al., 2002; Müller et al., 2010; Vanderborght et al., 2005).

Most geophysical applications have attempted to resolve aquifer heterogeneity and have treated the geophysical properties as isotropic. However, it has long been known that geophysical properties (e.g. electrical resistivity) show anisotropy (e.g. Schlumberger et al., 1934). This anisotropy can be related to unresolved subsurface structures at the microscopic scale (e.g. preferential electrical conduction in mineral grains) or to unresolved structures at the macroscopic scale (e.g. fine layering). In particular, such unresolved subsurface structures affect the electrical properties of the subsurface (Hill, 1972; Zisser and Nover, 2009). Therefore, several studies have explored the electrical anisotropy associated with horizontally isotropic layered media (Edwards et al., 1984; Kenkel et al., 2012), gas hydrate-filled fractures (Cook et al., 2010), and hydraulic conductivity in bog peats (Beckwith et al., 2003a,b).

Recently, Winchen et al. (2009) presented a synthetic modelling study that investigated whether information on subsurface structure can be obtained from the anisotropy in effective complex electrical resistivity. For this, they simulated the effective complex electrical resistivity in two perpendicular directions for bimodal heterogeneous distributions of two isotropic materials that have different complex resistivity that can be described by the Cole-Cole model (Cole and Cole, 1941; Pelton et al., 1978). They found an empirical relationship between the mixing parameter (α) of a power averaging model (McCarthy, 1991) to describe the effective complex electrical resistivity and the correlation length ratio of the two semivariogram models that were used to generate the bimodal distribution. Finally, they showed that the correlation length ratio can be inversely estimated from the effective complex electrical resistivity in two directions (i.e. the anisotropy). Although these results were promising, they were obtained in a synthetic modelling study and it is not evident that these findings also apply to laboratory or field measurements of complex electrical properties.

1.2.2 *Macropore Preferential Flow*

Accurate predictions of both flow and solute transport processes in the vadose zone are required to appropriately address problems of groundwater contamination and to predict the replenishment of limited groundwater resources. In this context, macropore preferential flow processes are of considerable importance because they can quickly transport water and contaminants from the surface to the groundwater. The importance of water flow and solute transport in macropores has been shown in a range of field studies (Beven and Germann, 1982; Flury et al., 1994; Ghodrati and Jury, 1992), and the mechanisms of preferential macropore flow have been elucidated in laboratory studies (Allaire et al., 2002a,b; Buttle and Leigh, 1997). In his review paper, Jarvis (2007) extensively discussed the causes and consequences of non-equilibrium flow in macropores, and he provided an overview of natural and anthropogenic factors that control the potential for non-equilibrium water flow in soils. To quantify the importance of preferential flow processes, accompanying models are required to describe the dynamics of the processes that occur during water movement (Castiglione et al., 2003; Feyen et al., 1998; Gerke, 2006; Greco, 2002; Köhne et al., 2009a,b; Lamy et al., 2009; Šimůnek et al., 2003).

Since macropore preferential flow is controlled by several factors such as the geometry of the pore structure, their size, and flow patterns, different methods have been used to investigate preferential flow. Allaire et al. (2009) reviewed several techniques to investigate preferential flow in the laboratory and field and differentiated between destructive and non-destructive methods. The most commonly used destructive method to investigate preferential flow paths is the use of dye tracers in the field (Flühler et al., 1996; Flury et al., 1994). Destructive characterization of macropore structure has also been achieved by filling the macropore with liquids that harden after some time (i.e. skeletisation of macropores). Skeletisation has been attempted with epoxy resin (Moran and McBratney, 1992a,b; Vervoort et al., 2003), paraffin wax (Meadows et al., 2005; Zaher et al., 2005), plaster of Paris (FitzPatrick et al., 1985), and latex (Abou Najm et al., 2010; Garner, 1953).

Laboratory investigations of macropore preferential flow have often used artificial macropores because such pores have some advantages over undisturbed field soil columns when the focus is on the elucidation of non-equilibrium water flow in macropores. For example, the well-known geometry of artificial macropores allows studying the effect of soil surface sealing on macropore flow (Ela et al., 1992). Furthermore, the easily constructed macropore-matrix profile allows performing different types of flow experiments, such as drainage, upward flow, and infiltration

experiments (Köhne and Mohanty, 2005). Luo et al. (2008) emphasized the importance of pore connectivity for macropore flow and found that many macropores are discontinuous from the top to the bottom of the soil profile, which means that these dead-end macropores are not effective for flow processes. Flow experiments with artificial macropores circumvent complications due to such dead-end macropores, and allow investigating macropore flow processes with a guaranteed pore connection between the surface and profile end.

Destructive methods are suitable to characterize structures of macropores, but obviously they are of limited value for investigating dynamic flow processes associated with macropores. Non-invasive methods that have been used to investigate and image macropore preferential flow processes are X-ray tomography (Luo et al., 2008, 2010; Mooney and Morris, 2008; Vanderborght et al., 2002), photoemission scanning (Perret et al., 2000), neutron imaging (Kaestner et al., 2008), and magnetic resonance imaging (Bechtold et al., 2011; Haber-Pohlmeier et al., 2010; Simpson et al., 2007). Although promising, these methods are restricted to investigations of dynamical flow processes associated with macropores in laboratory soil columns only, and some limitations exist that hinder their usability. For example, most of these methods rely on small sample sizes that may not be representative of field-scale processes. In addition, most of these methods are very costly, inaccessible, and difficult to transfer from the laboratory to the field.

Electrical resistivity measurements may provide a suitable alternative because they are able to cover sample sizes ranging from laboratory columns to entire fields. Recently, Moysey and Liu (2012) studied if macropore activation can be detected using electrical resistivity measurements. They used saturated soil samples and made electrical resistivity measurements using a Wenner array configuration with 30 mm electrode spacing. To create artificial macropores, they inserted 75 nonconducting rods vertically into the soil samples. These rods were sequentially removed and the apparent resistivity was measured after each rod removal. They found that an increase of macropore porosity by 4 % decreased the apparent resistivity by up to 30 %. They concluded that resistivity monitoring is a viable approach for detecting the onset of macropore flow in field studies. Although the study of Moysey and Liu (2012) presented first promising results, infiltration and the exchange of water between the macropore and the matrix domain was not considered in their fully saturated samples. In unsaturated soils, activation of macropores is expected to create a dynamic change in the apparent resistivity. In a series of recent publications, Greve et al. investigated preferential flow in cracked soils using the anisotropy of electrical resistivity in the horizontal plane measured with square-electrode configurations (Greve et al., 2010a,b, 2012b). The work of

Greve et al. (2012b) nicely showed that electrical resistivity measurements may be an appropriate tool to investigate flow processes in soils with dynamic changes in soil cracking. However, they did not consider electrical anisotropy in the vertical plane, which is also expected to vary because of the presence of time-stable resistive (air-filled) or conductive (water-filled) macropores.

Interestingly, electrical resistivity distributions can be determined using ERT. The principle of ERT is to use many different combinations of electrical current injection in two electrodes and electrical potential measurements in two other electrodes to obtain information about the subsurface electrical resistivity distribution using inversion. ERT has been used to monitor field-scale drainage and infiltration processes (Daily et al., 1992; Garré et al., 2011; Glass et al., 2002; LaBrecque et al., 2002; Michot et al., 2003), solute transport processes at different scales ranging from laboratory soil columns (Binley et al., 1996a,b; Olsen et al., 1999; Slater et al., 2002), lysimeters (Garré et al., 2010; Koestel et al., 2009a,b), up to the field scale (Binley et al., 2002; Deiana et al., 2008; Garré et al., 2013; Oberdörster et al., 2010). The reader is referred to the review paper of Samouëlian et al. (2005) for a comprehensive description of the use of ERT in soil science and an overview of the main advantages and limitations of ERT in 1D-, 2D-, and 3D surveys. The state-of-the-art of ERT inversion also referred to as ERT imaging is nicely introduced in the recent review of Loke et al. (2013).

ERT has also been used to study the importance of preferential flow in cracking soils. For example, Jones et al. (2012) used ERT to map the crack network in soil. In addition, ERT has been used to monitor seasonal changes in soil due to swelling and shrinking on a flood embankment (Jones et al., 2014), and to investigate the relationship between soil cracking and water irrigation events in the root zone (Greve et al., 2012a). Furthermore, Slater et al. (1997) used cross-borehole ERT measurements to map preferential flow pathways in limestone environment. Finally, Nimmer et al. (2007) used both cross-borehole and surface ERT measurements to monitor the dilution of a conductive potassium chloride plume in a fractured rock environment.

However, researchers have typically applied isotropic ERT inversion (e.g. Bechtold et al., 2012; Coscia et al., 2012; Doetsch et al., 2012; Günther et al., 2006; Vanderborght et al., 2005; Wagner et al., 2013) to image dynamic changes in soil properties so far, and very few attempts have been made to consider anisotropy in soil electrical resistivity although this may provide information about lateral and vertical variation in soil characteristics and preferential flow processes. Pain et al. (2003) and Herwanger et al. (2004) presented anisotropic resistivity inversion methods to estimate heterogeneous distributions of anisotropic electrical re-

sistivity. Furthermore, Kenkel et al. (2012) developed 2D anisotropic complex conductivity inversion and Schmoldt and Jones (2013) nicely illustrated how interpretation of anisotropic 1D- and 2D inversion of magnetotelluric data can be used to obtain orthogonal geological strike directions.

1.3   Thesis Objectives and Outline

The key question that this thesis addresses is: how to derive information from the anisotropy of electrical properties for the characterization of heterogeneous sediment structures and preferential flow processes? In order to answer this question, we formulated the following sub-objectives that will be addressed in three Chapters:

1. Experimentally validate the theoretical findings of the synthetic modelling study by Winchen et al. (2009) that showed how information on soil heterogeneity can be obtained from the anisotropy in electrical resistivity.

2. Evaluate whether dynamical changes in the anisotropy of electrical resistivity can be used to identify the existence of flow in macropores and to characterize the exchange between macropores and bulk soil.

3. Explore whether time-lapse ERT imaging instead of direct measurement of horizontal and vertical resistivity can provide valuable information with high resolution in space and time that allows analyzing preferential flow processes associated with macropores.

The remaining of the thesis is organized as follows. Chapter 2 experimentally validates the modelling study of Winchen et al. (2009) that showed that information on soil heterogeneity can be obtained from the anisotropy in electrical resistivity. In particular, the anisotropy of heterogeneous bimodal facies distributions of two isotropic materials packed in a measurement cell is determined in the mHz to kHz frequency range. Subsequently, the ratio of correlation lengths that describe the structure of the sediment is estimated directly from the complex electrical resistivity measurement in two directions (i.e. the electrical anisotropy).

Chapter 3 addresses anisotropy in electrical resistivity during a water infiltration experiment in artificial macropore. First, a synthetic modelling study is presented that investigates the dynamical changes in the anisotropy of electrical resistivity. For this, a coupled hydrological-electrical model to describe the effect of preferential flow on electrical properties is developed and validated by simulating water content distributions in 2D using HYDRUS code and converting water distribu-

tions to resistivity distributions to monitor the temporal developments of effective complex electrical resistivity in horizontal and vertical direction in 3D using MATLAB software. To evaluate the temporal development changes in the anisotropy of electrical resistivity in the laboratory, an infiltration experiment for a soil column with artificial macropore is performed and the electrical impedances in horizontal and vertical direction is measured using the EIT system.

Chapter 4 deals with imaging of macro-anisotropy in electrical resistivity during water infiltration in an artificial macropore in a Hele-Shaw tank. Time-lapse electrical resistance measurements using a very fast ERT system are made during water infiltration. The electrical resistance data are inverted for anisotropic electrical resistivity using an inversion grid that is substantially coarser than the size of the macropore. This results in resistivity images in two perpendicular (X- and Z-) directions that are used to calculate macroscopic electrical anisotropy.

Finally, Chapter 5 summarizes the overall conclusions of this thesis. Recommendations to address the drawbacks and limitations that have been identified here will be made. Last but not least, an outlook is provided to guide future work towards field applications that build on the laboratory investigations presented in this thesis.

Chapter 2

USING ELECTRICAL ANISOTROPY FOR SUB-SCALE STRUCTURAL CHARACTERIZATION OF SEDIMENTS: AN EXPERIMENTAL VALIDATION STUDY[1]

In the previous Chapter 1, we presented a general introduction and literature background of topics that are covered in this thesis. In particular, a synthetic modelling study was discussed where information on soil heterogeneity was obtained from the anisotropy in electrical resistivity. The objective of this Chapter (2) is to experimentally validate the findings of this synthetic modelling study. In order to do so, we develop a new measurement procedure to determine the effective complex electrical resistivity from a set of current injections and potential measurements on a heterogeneous distribution. A synthetic modelling study will be presented that confirms that this new measurement procedure is able to reproduce the results of the previous study that showed how the electrical properties and the correlation length ratio of bimodal distributions of two materials can be obtained

---

[1]Adapted from Al-Hazaimay S., J.A. Huisman, E. Zimmermann, and H. Vereecken. Using electrical anisotropy for structural characterization of sediments: An experimental validation study. Manuscript submitted to Near Surface Geophysics.

from the effective complex electrical resistivity measured in two perpendicular directions. After validation of the new measurement approach, measurement results will be presented for two bimodal distributions in a 2D measurement cell. It will be shown that the newly developed measurement strategy is able to estimate the electrical properties, the volume fraction, and the correlation length ratio with good accuracy from complex resistivity measurements in two directions.

2.1 Measurements

2.1.1 *Electrical Impedance Measurements*

Figure 2.1 shows the EIT system and its components that were used in this study (Zimmermann et al., 2008b). We used the principle of four-point electrode configurations, where two electrodes were used for current injections and two other electrodes were used for potential measurements. The EIT system consists of a function generator (Agilent 33120A) that produces a sinusoidal input signal with a frequency ranging from 10^{-2} Hz to 10^{+4} Hz and a peak-to-peak voltage of 10 V. Multiplexer cards select the two predefined active channels for current injection. For current measurement and correction, two shunt resistors are used that are both connected to the ADC cards. Electrode modules with amplifiers and relays are used to minimize the electrical load at the electrodes. Each electrode module is connected to an ADC for potential measurements. The EIT measurement system has 40 channels that can be used for current injections and potential measurements. In each measurement step, two channels are used to inject current and thirty-eight channels are used to measure the electrode voltages relative to ground. Potential differences between electrodes are calculated for the four-point electrode configurations of interest *a posteriori*. Electrode cables with a fixed length of 5000 mm were used to connect the electrode modules to the EIT system using electrode terminals (RJ45-Cat5e). A LabVIEW program is used to control the function generator and the ADC cards and to acquire and store the output voltage. A custom-made MATLAB library is responsible for post-processing of the measurements.
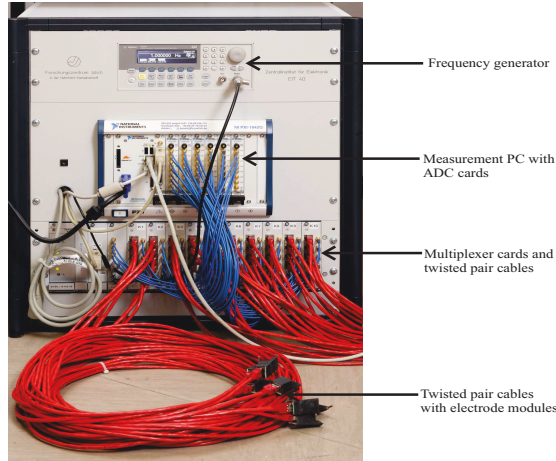
Figure 2.1: Components of the EIT system (MEDUSA-2) of Zimmermann et al. (2008b).

2.1.2 *Experimental Setup*

We used a square 2D measurement cell (Figure 2.2) with a side length of 480 mm and a height of 50 mm. Ten electrodes were equally spaced along each side with a separation of 45 mm from each other and with a separation of 37.5 mm from the corners of the cell. The electrodes were made of silver wires with a diameter of 1.5 mm and extended along the entire height of the measurement cell so that 2D electrical current flow can be assumed.
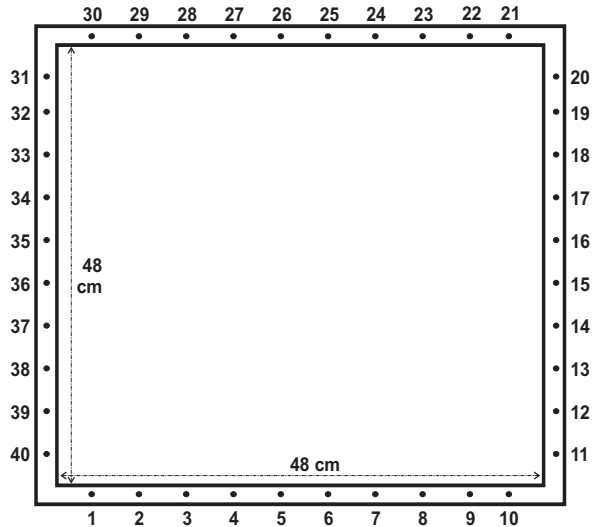
Figure 2.2: 2D measurement cell showing dimensions and electrode positions (numbers 1 to 40).

We used two different materials to create bimodal heterogeneous distributions in the measurement cell. For material A, we selected a combination of sand (F36, Quarzwerke Frechen GmbH, Frechen, Germany) with a mean grain size of 0.16 mm and 3 % by weight of activated charcoal (Merck KGaA, Darmstadt, Germany) with particle sizes ranging from 0.3 mm to 0.5 mm. For material B, we used the same sand and added 10 % by weight of bentonite (EDASIL Agrimont GmbH, Abensberg, Germany) with a mean grain size of 63 μm. We selected these two materials because they were expected to show a strong contrast in the frequency-dependent complex resistivity. To determine the actual complex resistivity of material A and B, we used the SIP system of Zimmermann et al. (2008a) with a cylindrical measurement cell with porous bronze current electrodes and non-polarizable potential electrodes with ceramic tips (more details in Breede et al., 2011). The measured resistivity magnitude and phase angle are shown in Figure
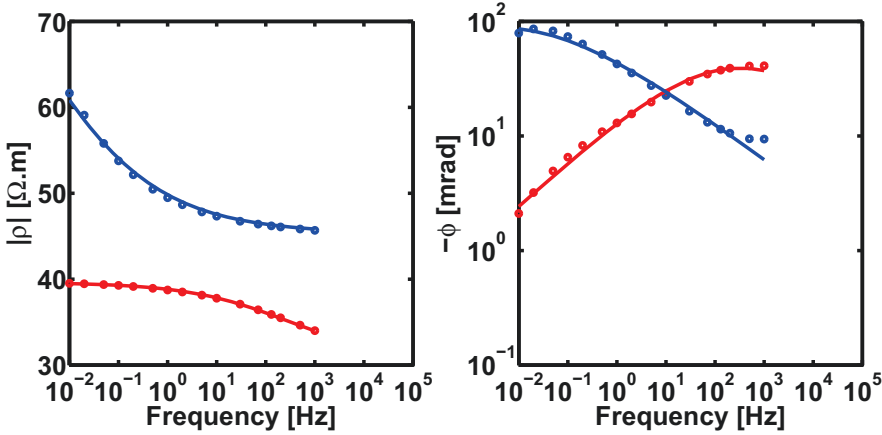
Figure 2.3: Resistivity magnitude (left) and phase angle (right) spectra showing the individual responses of the measured (dots) and fitted (lines) complex resistivity of material A (blue) and B (red).

The complex resistivity (ρ, $\Omega.m$) of material A and B was described with a Cole-Cole model:

$$\rho(\omega) = \rho_0 \left[1 - m \left(1 - \frac{1}{1 + (i\omega\tau)^c} \right) \right] \qquad (2.1)$$

where ω ($rad\ s^{-1}$) is the angular frequency ($2\pi f$), f (Hz) is the frequency, ρ_0 ($\Omega.m$) is the DC resistivity, m is the chargeability, τ (s) is the relaxation time, and c is the Cole-Cole exponent. The Cole-Cole parameters for each material

were obtained by manually fitting Equation 2.1 to the measured spectra shown in Figure 2.3. The fitted complex resistivity is also shown in Figure 2.3 and the Cole-Cole parameters are provided in Table 2.1. It can be seen that material A is more resistive with a relatively strong polarization peak in the mHz range, and that material B is more conductive with a relatively weaker polarization peak in the kHz range. Because of the use of a single Cole-Cole model, the high-frequency increase in polarization associated with Maxwell-Wagner polarization and the effect of the electrode contact impedance (see Breede et al., 2012) is not well captured.

Table 2.1: **Cole-Cole parameters obtained by fitting Equation 2.1 to SIP spectra plotted in Figure 2.3.**

Parameter	Material A	Material B
ρ ($\Omega.m$)	74	40
m	0.34	0.29
10^τ (s)	1	-3.50
c	0.50	0.30

Two bimodal distributions of material A and B were experimentally investigated in the measurement cell (Figure 2.4). The first distribution (dist7030) had a volume fraction (f) of 0.7 for material A and 0.3 for material B. We used the following procedure to pack the measurement cell with material A and B. In a first step, material A was prepared by mixing F36, charcoal, and NaCl solution with weights that are presented in Table 2.2. The electrical conductivity of the NaCl solution was 500 μS cm^{-1} at $20°C$. Material A was packed by adding eight spoons at a time to the measurement cell, stirring the saturated material, and firm pressing to avoid collecting air bubbles. Next, material B was prepared by mixing F36, bentonite, and NaCl solution with the same electrical conductivity with weights that are presented in Table 2.2. Material B was packed in the measurement cell by removing 60x20x20 mm stripes from material A, adding four spoons of material B to the cavities thus created, stirring the material, and applying light pressure to remove air bubbles and to assure good contact at the interface between material A and B.

The second distribution (dist5050) had equal volume fractions of 0.5 for material A and B, which were prepared and packed in the same manner as material A in dist7030 with the weights provided in Table 2.2. A thin plastic ruler with a length of 480 mm was positioned at the interface between material A and B to ensure material separation during the packing procedure. The ruler was removed after packing, and both materials were slightly compressed to establish contact between materials A and B.

Table 2.2: **Material weights used to prepare material A and B in distribution dist5050 and dist7030.**

Distribution	Material A			Material B		
	F36 (g)	charcoal (g)	NaCl (cm^3)	F36 (g)	bentonite (g)	NaCl (cm^3)
dist5050	4975	154	1260	1978	220	540
dist7030	3620	112	900	3359	373	900
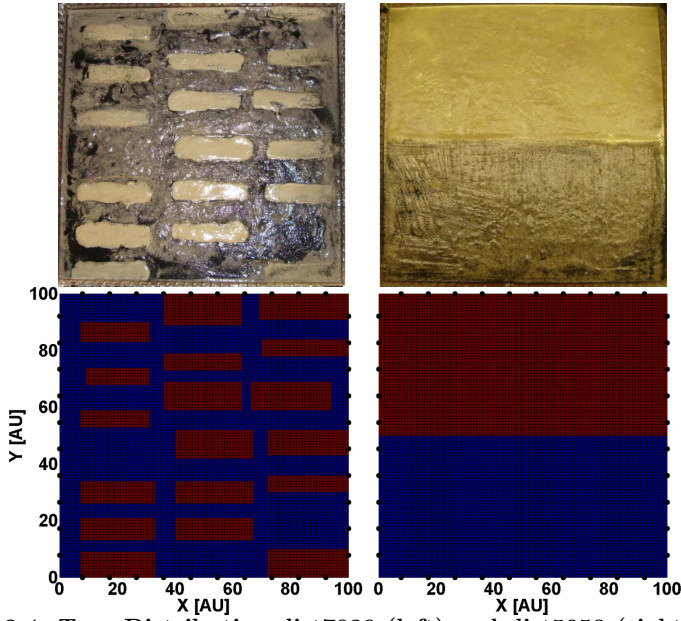
Figure 2.4: **Top: Distribution dist7030 (left) and dist5050 (right) showing the arrangement of material A (dark) and B (light) in the measurement cell. Bottom: Distribution sim7030 (left) and sim5050 (right) showing the arrangement of material A (blue) and B (red). Black dots show the position of the electrodes.**

2.1.3 Electrical Anisotropy Measurements

To determine the anisotropy in effective complex electrical resistivity for the bi-modal distributions shown in Figure 2.4, we performed electrical measurements in two directions. In a first step, we injected current in one direction through one pair of electrodes (e.g. 1-30 in Figure 2.2) and measured potential differences through all other pairs in the same direction (e.g. 2-29, 3-28, ..., 10-21). This procedure resulted in nine potential difference values for one current injection. In a second step, we injected current through a second pair of electrodes (e.g. 2-29). Again, we measured potential differences in all other pairs of electrodes (e.g. 1-30, 3-28, ..., 10-21). We repeated this process by injecting current for the rest of all electrode pairs in a particular direction (e.g. 3-28, 4-27, ..., 10-21). In total, this resulted in 90 potential difference values in a particular direction. This procedure was repeated for the perpendicular direction (e.g. current injection in electrodes 11-40, 12-39, etc.) to obtain a second set of 90 potential difference values. The derivation of the effective complex electrical resistivity (section 2.2.3) in both directions from these two sets of measurements is discussed after the introduction of the simulation studies.

2.2 Simulations

2.2.1 *Forward Problem*

In the forward problem, we calculated electrical impedances associated with the four-point electrode configurations described above using a FEM as described in literature (Murai and Kagawa, 1985; Zimmermann, 2010). Poisson's Equation was solved for electrical potential distribution for a given current injection assuming an isotropic 2D electrical resistivity distribution:

$$\frac{\partial}{\partial x}\left(\frac{1}{\rho^*}\frac{\partial \varphi}{\partial x}\right) + \frac{\partial}{\partial y}\left(\frac{1}{\rho^*}\frac{\partial \varphi}{\partial y}\right) = I\delta(x - x_0)\delta(y - y_0) \qquad (2.2)$$

where φ (V) is the electrical potential distribution, I (A) are point current sources with coordinates $(x_0,\ y_0)$ in m, and δ is a Dirac-delta function. Equation 2.2 was solved for the electrical potential distribution using the FEM method and an appropriate set of boundary conditions (Dirichlet and Neumann boundaries).

2.2.2 Heterogeneous Distributions for Synthetic Modelling

Bimodal heterogeneous distributions were created on a rectangular 100x100 grid using the SISim algorithm from GSLib (Deutsch and Journel, 1998). The semi-variograms used to create these heterogeneous distributions varied with respect to the volume fraction of material A and B and also considered anisotropy in the correlation lengths in x- and y- direction. In total, we created 247 bimodal distributions with 13 correlation length ratios ranging from 1 to 7 in x-direction while a value of 2 was considered in y-direction, and 19 volume fractions for material A ranging from 0.05 to 0.95. In addition, we considered the two bimodal distributions shown in Figure 2.4. Figure 2.5 shows a selection of the generated bimodal distributions for three volume fractions of material A (0.05, 0.30, and 0.50) and selected correlation length ratios (1 [2-2], 2.5 [5-2], 4.5 [9-2], 6 [12-2], and 7 [14-2]). The same set of current injections and potential measurements described above was then simulated in two perpendicular directions for the 247 bimodal distributions. The derivation of the effective complex electrical resistivity in both directions from these two sets of measurements is described next.
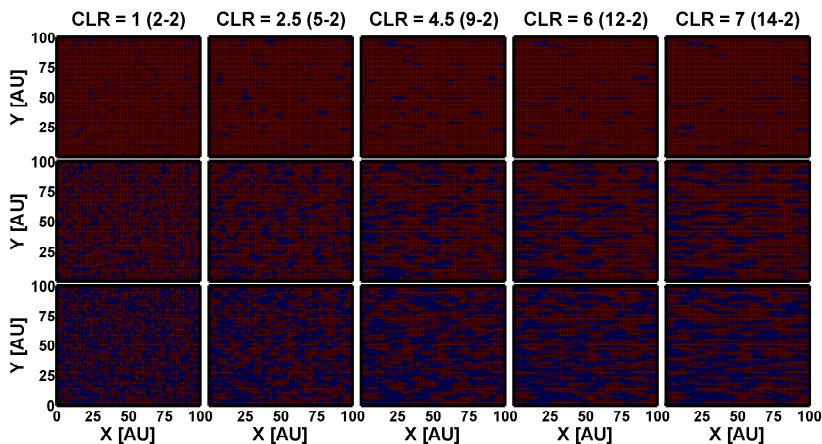
Figure 2.5: Exemplary bimodal distributions generated using the SISim algorithm. The volume fraction of material A (blue) is 0.05 (top), 0.30 (middle), and 0.50 (bottom) row, respectively. From left to right column, the correlation length ratio between x- and y-direction increases.

2.2.3 *Derivation of Effective Complex Electrical Resistivity*

In their synthetic modelling study, Winchen et al. (2009) determined the effective complex electrical resistivity by applying constant potentials at two sides of the domain, and determining the amount of current flow across the bimodal distribution. Such a method is possible in simulation studies, but cannot be used in a verification study with actual measurements. Therefore, we developed a new approach to estimate the effective complex electrical resistivity from a set of current injections and associated potential measurements obtained using point electrodes. The challenge here is to transform the original dataset in such a way that constant potentials at the two opposite borders can be assumed.

Figure 2.6: Simple electrical circuit with current flow I and potentials U across a sample.

Consider the electrical impedance (Z) of a simple circuit (Figure 2.6), which can be calculated according to:

$$ZI = U \tag{2.3}$$

where U (V) is the voltage, and I (A) is the current. Equation 2.3 can be reformulated for a set of n current injections and m potential measurements:

$$\left[\sum_n Z_{m,n} I_n \right] = U_m \tag{2.4}$$

in the next step, we want to reformulate Equation 2.4 to obtain a constant (arbitrary) voltage U at the two opposite boundaries of the domain. For this, we introduce the weighting vector w_n and the unity matrix E_m:

$$\left[\sum_n Z_{m,n} I_n w_n \right] = \left[E_m \right] U \tag{2.5}$$

using matrix notation and some manipulation, Equation 2.5 can be rewritten

as:

$$[Z_{m,n}][diag(I_n)][w_n] = [E_m]U \tag{2.6}$$

$$[w_n] = \Big([Z_{m,n}][diag(I_n)] \Big)^{-1}[E_m]U \tag{2.7}$$

we now calculate the effective current across the domain using:

$$I = [I_n]^T[w_n] \tag{2.8}$$

and the effective impedance can then be calculated using:

$$Z = U/I \tag{2.9}$$

the effective complex electrical resistivity can be calculated from this impedance using:

$$\rho^*_{eff} = \frac{ZA}{l} \tag{2.10}$$

where A (m^2) is the cross-sectional area of the sample, and l (m) equals the side length of the simulation or measurement domain.

In order to accurately calculate I and Z using the procedure outlined above, one would need to know the voltage at all electrodes including the current electrodes. Unfortunately, the voltages at the current electrodes cannot be determined accurately because of the unknown contact impedance. To overcome this problem, we introduce a constant correction factor k to compensate for the missing voltage at the current electrodes:

$$I_{est} = [I_n]^T[w_n]k \tag{2.11}$$

where I_{est} is the estimated current flow across a heterogeneous distribution for a given constant voltage difference. I_{est} can be used to calculate the effective impedance and complex resistivity using Equation 2.9 and 2.10, respectively. In order to estimate k, we simulated 90 potential measurements following the procedure described above for homogeneous models of material A and B using the parameters provided in Table 2.1. An almost perfect correspondence between pre-

scribed and estimated effective complex electrical resistivity was obtained when

Figure 2.7: Resistivity magnitude (left) and phase angle (right) spectra of the known (dots) and estimated (lines) complex resistivity of a homogeneous model of material A (blue) and B (red).

2.2.4 Estimation of Correlation Length Ratio from Effective Complex Electrical Resistivity

To estimate the correlation length ratio from the effective complex electrical resistivity in two directions, we applied the inversion approach of Winchen et al. (2009). This inversion relies on a power averaging model to relate the resistivities of the two materials, the volume fraction f, and the effective complex electrical resistivity:

$$\left(\frac{1}{\rho^*_{eff}}\right)^{\alpha} = \text{f.}\left(\frac{1}{\rho_{\text{A}}}\right)^{\alpha} + (1-\text{f}).\left(\frac{1}{\rho_{\text{B}}}\right)^{\alpha} \qquad (2.12)$$

where ρ_{A} and ρ_{B} $(\Omega.m)$ are the complex resistivity of material A and B described using Cole-Cole parameters of Equation 2.1, and α is the mixing parameter. Winchen et al. (2009) showed that the mixing parameter was related to the correlation length ratio by:

$$\alpha = \text{a} + \text{b.}\left(\frac{\xi_{\parallel}}{\xi_{\perp}}\right)^{\text{c}} \qquad (2.13)$$

where a, b, and c are empirical constants whose values are -1.07, 0.86, and 0.32,

19

respectively, and $\xi_\parallel$ and $\xi_\perp$ are correlation length in two perpendicular directions. To estimate the correlation length ratio from effective complex electrical resistivity, the power averaging model in combination with the empirical Equation for α was fitted to the effective complex electrical resistivity determined in two directions. This was achieved by varying the Cole-Cole parameters of the two materials, the volume fraction, and the correlation length ratio using the SCE algorithm (Duan et al., 1993), which is a global optimization algorithm that combines stochastic and deterministic search approaches to minimize the following OF:

$$OF = \sum_\omega \left(\frac{\Re(\rho_{True}^\omega - \rho_{eff}(\mathrm{f}, \alpha, \rho_\mathrm{A}, \rho_\mathrm{B}))}{\Re(\rho_{True}^\omega)} \right)^2 + \sum_\omega \left(\frac{\Im(\rho_{True}^\omega - \rho_{eff}(\mathrm{f}, \alpha, \rho_\mathrm{A}, \rho_\mathrm{B}))}{\Im(\rho_{True}^\omega)} \right)^2 \tag{2.14}$$

where ρ_{True}^ω $(\Omega.m)$ is the simulated or measured effective complex electrical resistivity, and ρ_{eff} $(\Omega.m)$ is the effective complex electrical resistivity calculated by the power averaging model using the resistivity of both materials, volume fraction, and the mixing parameter estimated from the correlation length ratio. Table 2.3 shows the lower and upper bounds that were used in the SCE algorithm to evaluate Equation 2.14:

Table 2.3: **Lower and upper limits of Cole-Cole parameters, volume fraction, and correlation length ratio used in the SCE algorithm to evaluate the** OF **(Equation 2.14).**

	ρ $(\Omega.m)$	m	10^τ (s)	c	f $(\%)$	correlation length ratio
Lower	1	0.1	-3	0	0.01	1
Upper	1000	0.5	5	1	0.99	10

2.3 Results and Discussion

2.3.1 *Validation of Approach to Estimate the Effective Complex Electrical Resistivity*

The approach to estimate the effective complex electrical resistivity from a set of current injections and potential measurements relies on an empirical correction factor k with a value of 0.744 that was derived from simulations for homogeneous distributions of material A and B. To test whether this value of k is also valid for heterogeneous distributions, we estimated the effective complex electrical re-

sistivity in two directions from a set of simulated current injections and potential measurements for the sim5050 distribution because an analytical solution is known for such a layered distribution ($\alpha = 1$ and -1 in Equation 2.12). Figure 2.8 presents the estimated effective complex electrical resistivity for the sim5050 distribution and the complex resistivity of material A and B. As already discussed by Winchen et al. (2009), the phase values are more influenced by material B when measurements are made parallel to the layering than the phase values for a measurement perpendicular (i.e. in series) to the layering at low frequencies. At high frequencies, the phase values are more influenced by material A for the measurements that are made perpendicular to the layering. It is important to realize that it is this frequency-dependent behavior of the effective complex electrical resistivity that allows estimating the Cole-Cole parameters, volume fraction, and the correlation length ratio. In particular, the estimation of the correlation length ratio would not be possible from the effective DC resistivity in two directions only (Winchen et al., 2009). The comparison of the known and estimated effective complex electrical resistivity for the sim5050 distribution in Figure 2.8 clearly shows that the correction factor determined for a homogeneous material also provides accurate estimates of the effective complex electrical resistivity of heterogeneous distributions. In series direction, the estimated effective complex electrical resistivity matches the known (analytical) solution very well. In parallel direction, the simplifying assumptions made in the derivation of Equation 2.5 to 2.11 resulted in a minor deviations from the expected effective complex electrical resistivity. However, we consider these deviations to be small compared to other uncertainties in this study, such as variability introduced by sample preparation.
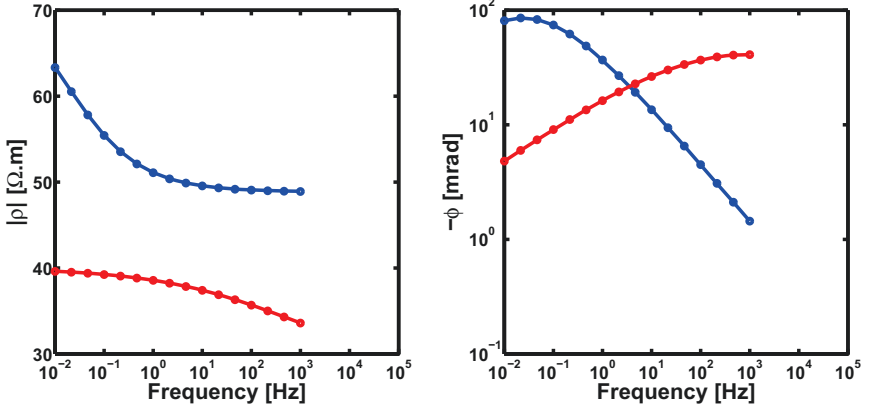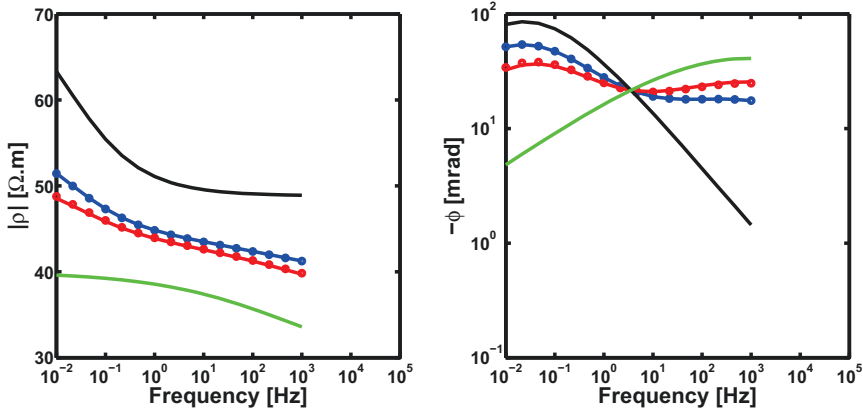
Figure 2.8: Resistivity magnitude (left) and phase angle (right) spectra of the known (dots) and estimated (lines) effective complex electrical resistivity in series (blue) and parallel (red) for distribution sim5050. Material A (black) and B (green) showing the individual responses of Cole-Cole model.

To investigate how the minor deviations between the known and estimated effective complex electrical resistivity shown in Figure 2.8 affect the inverted parameters, the estimated effective complex electrical resistivity in two directions was used in the inversion approach using Equations 2.12 and 2.14. Figure 2.9 shows the estimated and fitted resistivity magnitude and phase angle spectra in series and parallel direction of distribution sim5050. Clearly, the power-average model fits the estimated effective complex electrical resistivity almost perfectly in both directions across the entire frequency range. Table 2.4 provides the known and fitted parameters (ρ_A, ρ_B, f) of both materials. The fitted resistivity magnitude deviates less than 1.1 $\Omega.m$ from the prescribed values for material A and B. The other fitted parameters are in even better agreement with the prescribed values. Therefore, we conclude that the newly developed measurement and interpretation strategy provides accurate estimates of the effective complex electrical resistivity.
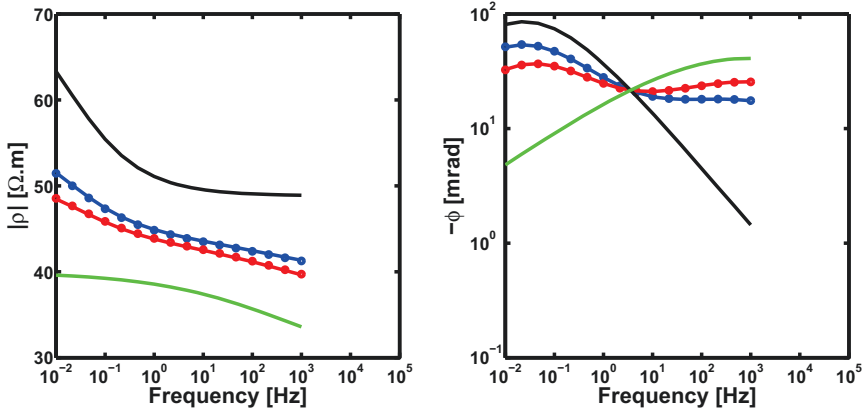
Figure 2.9: Resistivity magnitude (left) and phase angle (right) spectra of the estimated (dots) and fitted (lines) effective complex electrical resistivity in series (blue) and parallel (red) for distribution sim5050. Material A (black) and B (green) showing the individual responses of Cole-Cole model.

Table 2.4: Prescribed and fitted Cole-Cole parameters and volume fraction for distribution sim5050.

	sim5050			
	Material A		Material B	
Parameter	Prescribed	Fitted	Prescribed	Fitted
ρ ($\Omega.m$)	74	75.06	40	39.35
m	0.34	0.34	0.29	0.29
10^τ (s)	1	0.99	-3.50	-3.51
c	0.50	0.50	0.30	0.30
f (%)	0.50	0.49	0.50	0.51

2.3.2 Simulation and Inversion Results

After establishing the validity of the new approach to estimate the effective complex electrical resistivity, we now aim to reproduce the main findings of Winchen et al. (2009) using simulations and inversions for a set of 247 bimodal distributions generated with SISim using different volume fractions and correlation length ratios. Figure 2.10 shows a scatter plot of the prescribed (input) and fitted correlation length ratio for all distributions. In accordance with Winchen et al. (2009), there is a clear positive correlation between prescribed and fitted correlation length ratio (r = 0.87) and the root mean square error is 99.8 %. The deviation between prescribed and fitted correlation length ratio increases with increasing correlation length ratio. Overall, the deviation between prescribed and fitted correlation

length ratio follows a normal distribution with a mean value of -0.07 and a standard deviation of 0.997. This suggests an almost unbiased estimate of the correlation length ratio, which is in contrast to the results of Winchen et al. (2009) who found a significant underestimation for high values of the prescribed correlation length ratio. We attribute this difference to the use of small correlation length in y-direction (see Figure 2.5), which ensures that the semivariogram of the SISim realization is close to that of the prescribed semivariogram. In Winchen et al. (2009), a wider range of values was used for the correlation length in y-direction, and the observed underestimation of the correlation length ratio was attributed to discrepancies of the actual and prescribed semivariogram for the SISim realization that occurred because of the limited size of the simulation domain (100 by 100).
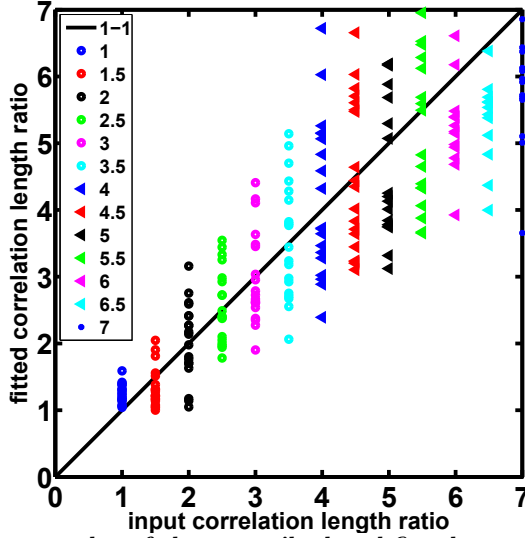
Figure 2.10: **Scatter plot of the prescribed and fitted correlation length ratio obtained by inversion of the effective complex electrical resistivity in two directions by minimizing Equation 2.14 for 247 distributions with varying Cole-Cole parameters, volume fraction, and the correlation length ratio for material A and B.**

Figure 2.11 shows a scatter plot of the prescribed (input) and fitted volume fraction of all distributions. Some deviations between prescribed and fitted volume fraction can be observed between 0.3 and 0.75, in particular for small correlation length ratios. However, the overall agreement is excellent (r = 0.99) and the root mean square error value is low with a value of 3 %. The deviation between prescribed and fitted volume fraction followed a normal distribution with a mean of -0.02 and a standard deviation of 0.024. The underestimation of the volume fraction by

24

values up to 0.1 reported by Winchen et al. (2009) could not be reproduced here for reasons that were discussed earlier.
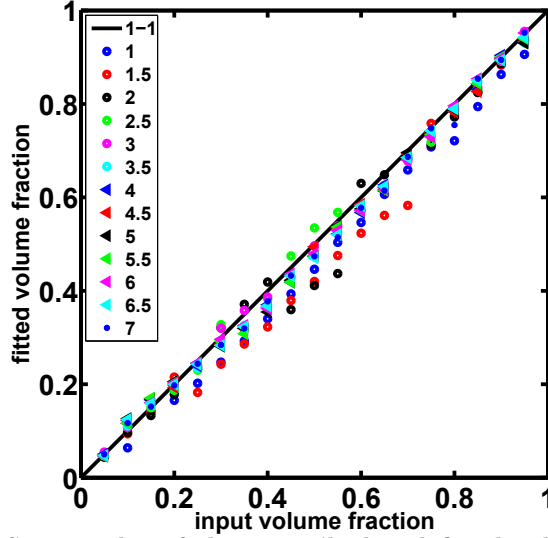
Figure 2.11: Scatter plot of the prescribed and fitted volume fraction obtained by inversion of the effective complex electrical resistivity in two directions by minimizing Equation 2.14 for 247 distributions with varying Cole-Cole parameters, volume fraction, and the correlation length ratio for material A and B.

The fitted Cole-Cole parameters for all simulated distributions are summarized in Figure 2.12 and Table 2.5. Figure 2.12 shows histograms of fitted Cole-Cole parameters and the fit of a Gaussian distribution based on the mean and standard deviation reported in Table 2.5. On average, the prescribed Cole-Cole parameters are accurately estimated in the inversion. However, there seems to be considerable uncertainty in the estimation of the DC resistivity for both materials.
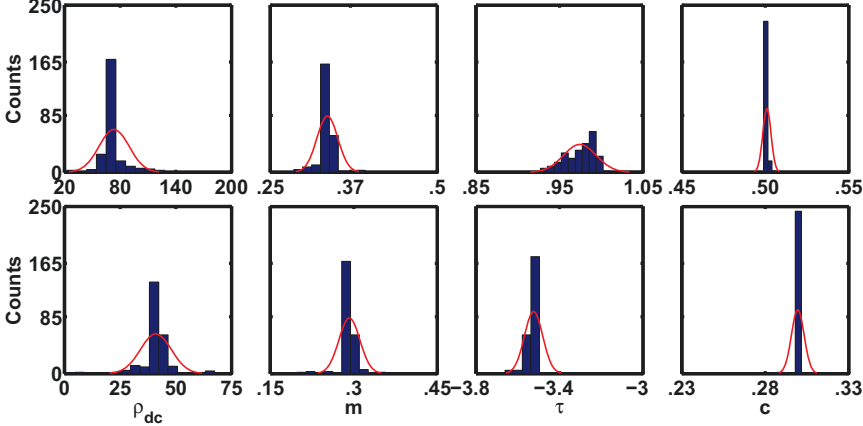
Figure 2.12: Histogram plots of the minimization function of Cole-Cole parameters. The upper row shows the parameter of material A (left to right; ρ_{dc}, m, τ, and c) and the lower row shows the parameter of material B (left to right; ρ_{dc}, m, τ, and c). The red curves are the fitted Gaussian distribution using the values from Table 2.5.

Table 2.5: Prescribed and mean fitted Cole-Cole parameters of the 247 distributions that were inverted using Equation 2.14. std. indicates the standard deviation of each parameter.

Parameter	Material A			Material B		
	Prescribed	Fitted	std.	Prescribed	Fitted	std.
ρ $(\Omega.m)$	74	73.41	16.157	40	41	6.925
m	0.34	0.34	0.016	0.29	0.29	0.019
10^τ (s)	1	0.97	0.020	-3.50	-3.52	0.044
c	0.50	0.50	0.003	0.30	0.30	0.004

In a next step, we analyze the distribution sim7030 shown in Figure 2.4. This distribution was created for ease of realization in an actual laboratory experiment and does not strictly corresponds to a stochastic realization from a bimodal distribution as shown in Figure 2.5. Determination of the indicator variograms in x- and y-direction showed that the expected correlation length ratio for the sim7030 is 6. We calculated the effective complex electrical resistivity in two perpendicular directions and inverted for the volume fraction, correlation length ratio, and the Cole-Cole parameters again. The fitted parameters are presented in Table 2.6 and these parameters are in reasonable agreement with prescribed values. The fitted correlation length of 7.39 is somewhat higher than expected from the semivariogram analysis, and this may be related to the fact that the parameterization of Equation 2.13 was derived from second-order stationary bimodal distributions generated with SISim. Clearly, sim7030 deviates considerably from such a realiza-

tion, and this may have affected the inversion results. Nevertheless, this synthetic study shows that an experimental validation of the numerical findings presented so far should be feasible using an actual realization of sim7030 (i.e. dist7030 in Figure 2.4).

Table 2.6: Prescribed and fitted Cole-Cole parameters, volume fraction, and correlation length ratio for distribution sim7030.

| | sim7030 | | | |
| | Material A | | Material B | |
Parameter	Prescribed	Fitted	Prescribed	Fitted
ρ ($\Omega.m$)	74	78.82	40	35.81
m	0.34	0.34	0.29	0.29
10^τ (s)	1	1.01	-3.50	-3.47
c	0.50	0.49	0.30	0.30
f (%)	0.70	0.63	0.30	0.37
correlation length ratio	6	7.39	-	-

2.3.3   *Experimental Validation*

For the experimental validation, material A and B were packed into the measurement cell (dist5050) and electrical impedance measurements were performed in two perpendicular directions using the EIT system. The effective complex electrical resistivity in both directions was then calculated using the methodology that was described earlier. Figure 2.13 shows the estimated effective complex electrical resistivity magnitude and phase angle spectra in series and parallel direction of the distribution dist5050. We ignored measurements higher than 1 kHz because of the electromagnetic coupling effects and Maxwell-Wagner effects in this frequency range (see Figure 2.3). Clearly, there is a marked similarity between the general shape of the resistivity magnitude and phase angle spectra for the simulation results (Figure 2.9) and the actual measurements (Figure 2.13). The best fitting model obtained in the inversion of the effective complex electrical resistivity for the volume fraction and Cole-Cole parameters for material A and B (with $\alpha = 1$ or -1) is also presented in Figure 2.13. In general, the fit is excellent and the best fitting parameters (ρ_A, ρ_B, f) are presented in Table 2.7. In general, the fitted Cole-Cole parameters are in reasonable agreement with those independently determined using SIP measurements. The variation in inverted relaxation times is within the range of values expected for different packing methods. There is a considerable deviation in the estimated volume fraction, which was not observed in the synthetic modelling studies. We found that the measured effective complex electrical resistivity is very sensitive to sediment thickness (see Equation 2.10),

and we suspect that the observed deviation in known and fitted volume fraction is a result of variations in sediment thickness across the measurement cell.

Finally, the effective complex electrical resistivity for the distribution dist7030 was determined in two directions (see Figure 2.13). Again, the inversion approach fitted the magnitude and phase of the effective complex electrical resistivity well and the inverted parameters are also reported in Table 2.7. The fitted Cole-Cole parameters are reasonably close to the expected values from SIP measurements and the inversion of dist5050. In particular, the relaxation times of dist5050 and dist7030 are reasonably close, which supports the notion that the observed differences in relaxation time can be related to differences in packing between SIP soil columns and the measurement cell shown in Figure 2.2. Most importantly, the fitted correlation length ratio of 7.89 is in good correspondence with the value expected from semivariogram analysis (6), and in even better correspondence to the value obtained from the inversion of the synthetic data for sim7030 (7.39).
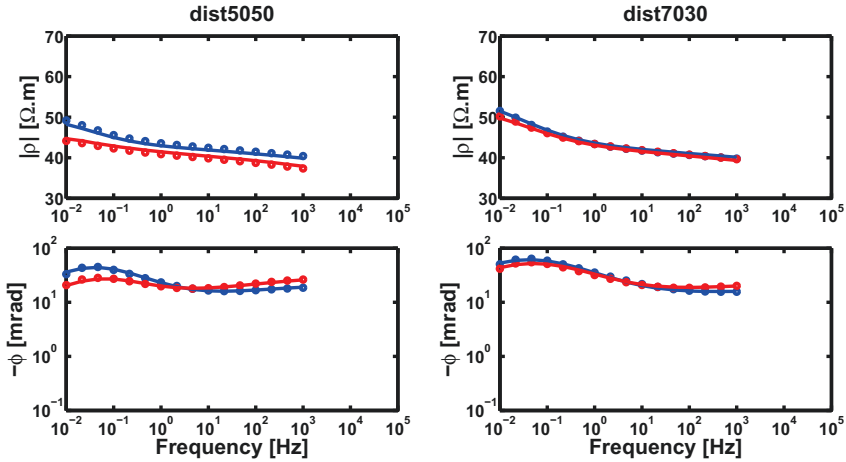
Figure 2.13: **Left: Resistivity magnitude (top) and phase angle (bottom) spectra of the measured (dots) and fitted (lines) effective complex electrical resistivity in series (blue) and parallel (red) obtained for distribution dist5050. Right: Resistivity magnitude (top) and phase angle (bottom) spectra of the measured (dots) and fitted (lines) effective complex electrical resistivity in series (blue) and parallel (red) obtained for distribution dist7030.**

Table 2.7: **Prescribed and fitted Cole-Cole parameters, volume fraction, and correlation length ratio obtained for the measured distribution dist5050 and dist7030.**

Parameter	Material A dist5050 Prescribed	dist5050 Fitted	dist7030 Fitted	Material B dist5050 Prescribed	dist5050 Fitted	dist7030 Fitted
ρ ($\Omega.m$)	74	75.02	70.73	40	39.04	40.37
m	0.34	0.28	0.34	0.29	0.39	0.47
10^{τ} (s)	1	0.70	0.76	-3.50	-4.77	-4.53
c	0.50	0.61	0.52	0.30	0.19	0.17
f (%)	0.50	0.33	-	0.50	0.76	-
	0.70	-	0.56	0.30	-	0.44
correlation length	-	-	-	-	-	-
ratio	6	-	7.89	-	-	-

2.4 Conclusions

In this study, we estimated structural parameters describing heterogeneity from measurements of the anisotropic effective complex electrical resistivity. We reproduced the main findings of the synthetic modelling study of Winchen et al. (2009), who estimated the correlation length ratio of semivariograms in x- and y-direction from the effective complex electrical resistivity. In addition, we experimentally validated the findings of Winchen et al. (2009).

In a first step, we have developed a new measurement strategy to determine the effective complex electrical resistivity from current and potential measurements with point electrodes on a heterogeneous distribution. This was required because Winchen et al. (2009) used a simulation approach that could not be applied in an experimental validation study. The newly developed measurement strategy was tested in a synthetic study on bimodal distributions with known electrical and structural properties, and we confirmed that the correlation length ratio could be accurately estimated with a root mean square error of 100 % from the effective complex electrical resistivity in two perpendicular directions. In addition, it was shown that the electrical properties of both materials and their volume fraction could be accurately estimated.

In a next step, the new measurement strategy was applied to actual heterogeneous bimodal sediment distributions in order to estimate the Cole-Cole parameters of both materials in addition to the volume fraction and correlation length ratio from broadband measurements of the effective complex electrical resistivity. The estimated Cole-Cole parameters were compared with independent parameters de-

termined directly from reference measurements on both materials independently. Despite differences in the packing procedure, the inverted Cole-Cole parameters were in good agreement with those of the reference measurements. In addition, the estimated correlation length ratio of the bimodal distribution obtained in the experimental validation matched very well with the value obtained in the synthetic study for the same distribution. It was concluded that anisotropy in the effective complex electrical resistivity can provide information on the structural properties of bimodal distributions, which is useful to obtain improved stochastic descriptions of soil and aquifers.

On a more general level, the results presented here show how structural organization of material properties can lead to anisotropy in the effective complex electrical resistivity. Since soils and aquifers are known to be structurally organized across a range of scales, the results of this study also highlight that anisotropy should perhaps not be ignored, as is currently done in many applications of electrical resistivity and impedance tomography. The development of reliable procedures to interpret measurements of the effective complex electrical resistivity in a tomographic inversion framework that considers anisotropy should therefore be prioritized in future work. Such tomographic inversions will provide images of the anisotropy in effective complex electrical resistivity that may be interpreted in terms of unresolved geological structures using the interpretation methods developed and validated in this study.

Chapter 3

INVESTIGATING PREFERENTIAL FLOW PROCESSES IN SOILS USING ANISOTROPY IN ELECTRICAL RESISTIVITY[1]

In the previous Chapter 2, we presented a study to experimentally validate a synthetic modelling study that showed how useful information on soil heterogeneity can be derived from electrical anisotropy measurements. As argued earlier, electrical anisotropy appears not only because of soil heterogeneity but can also be caused by flow processes in macropores that are present in horizontal and vertical direction in the vadose zone. Therefore, the objective of this Chapter (3) is to evaluate whether dynamic changes in the anisotropy of electrical resistivity can be used to identify water flow in macropores. Simulations and experiments will be performed for infiltration in a soil column with an artificial macropore. In a first step, 3D water content distributions associated with infiltration into the artificial macropore will be simulated and the simulated temporal development of the resistivity anisotropy will be obtained by solving the Poisson Equation after converting the simulated water content distributions to electrical resistivity distributions. It will be shown that the horizontal and vertical resistivity react differently to the presence of the macropore, and that this leads to electrical anisotropy in the resistivity. To verify the simulation results, we will also present measurements of the

---

[1]Adapted from Al-Hazaimay S., J.A. Huisman, E. Zimmermann, and H. Vereecken. Investigating preferential flow processes in soils using anisotropy in electrical resistivity. Manuscript submitted to Vadose Zone Journal.

temporal dynamics of the anisotropy in resistivity during water infiltration in an
artificial macropore.

3.1   Measurements

3.1.1   *Electrical Measurements*

The electrical resistivity measurements were made using the EIT system of Zimmermann et al. (2008b). We used the principle of four-point electrode configurations, where two electrodes were used for current injections and two other electrodes were used for potential measurements. The EIT system consists of a function generator (Agilent 33120A) that produces the sinusoidal input signal with a frequency of 1 Hz and a peak-to-peak voltage of 10 V. Multiplexer cards select the two active channels for current injection using predefined electrode configurations. For current measurement and correction two shunt resistors are used. The end of each resistor is connected to ADC cards. Electrode modules with amplifiers and relays are used to minimize the electrical load at the electrodes. Each electrode modules is connected to an ADC card for simultaneous measurements of all electrode potentials. A LabVIEW program is used to control the function generator and the ADC cards and to acquire and store the output voltage. A custom-made MATLAB library is responsible for post-processing of the measurements.

Different types of electrodes were used for current injections and potential measurements. To inject current, we used brass electrodes with a length of 86 mm and a diameter of 5 mm. Electrodes were inserted into the column for infiltration experiments (see Figure 3.1) using cable glands. The end of the current electrodes was plane with the inner wall of the column. We installed the current electrodes before soil material was packed in the column to ensure good electrical contact during the infiltration experiment. To measure the potential difference, we used non-polarizable electrodes that were described in detail by Breede et al. (2011). These non-polarizable electrodes consist of a small tube made of PMMA with a length of 210 mm and a diameter of 5 mm, and they are closed from both sides by a cone-shaped porous ceramic at one end and a plug at the other end. The PMMA tube was filled with the same water that we used in the infiltration experiment. A silver wire with a diameter of 1 mm is located in the middle of the PMMA tube and is fixed by the plug at the end of the electrode. The ceramic cone is made of aluminum oxide with a diameter of 5 mm. The structure of the electrodes allows insertion of the ceramic cone inside the column which provides

good material contact without introducing polarization by the presence of metal in the current flow pathways (Breede et al., 2011).
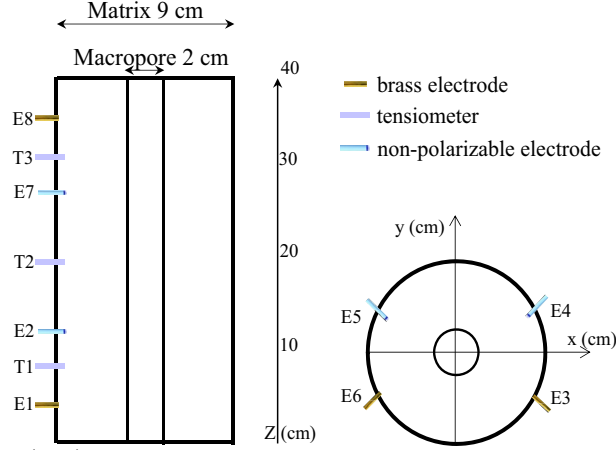
Figure 3.1: (left) 2D vertical cross-section of the artificial macropore surrounded by soil matrix showing locations of the electrodes in vertical direction (E1, E2, E7, and E8) and tensiometers (T1, T2, and T3). (right) Horizontal cross-section of the infiltration column showing the location of the electrodes in horizontal direction (E3, E4, E5, and E6).

3.1.2   *Soil Column with Artificial Macropore*

Following the work of Köhne and Mohanty (2005), we built a soil column with an artificial macropore (see Figure 3.1). The soil column was 400 mm high and had an inner diameter of 90 mm. We used two different materials to prepare the matrix and macropore domains. For the matrix domain, we selected a mixture of fine sand (F34, Quarzwerke Frechen GmbH, Frechen, Germany) with a mean grain size of 0.2 mm and 10 % of silt-clay mixture (Mahlton FT-202r, SIBELCO Deutschland GmbH, Ransbach-Baumbach, Germany) with a particle size distribution between 0.63 μm - 63 μm. This material will hereafter be referred to as the sand-clay mixture. For the macropore domain, we selected coarse sand (FH31, Quarzwerke Frechen GmbH, Frechen, Germany) with a mean grain size of 0.35 mm.

The following procedure was used to prepare the soil column with an artificial macropore. First, we positioned a PMMA tube with an outer diameter of 20 mm in the middle of the column and fixed its position. The diameter of the PMMA tube was selected to create a macropore with a volume of 5 % of the entire soil volume of the column. The sand-clay mixture that makes up the matrix domain was prepared by adding 411 cm^3 of tap water to 3600 g of sand-clay mixture. The

conductivity of the tap water was 460 $\mu S\ cm^{-1}$ at 20°C. The matrix domain was packed in layer increments of approximately 30 mm thickness by firm pressing. For the macropore domain, 400 g of coarse sand was mixed with 6 cm^3 of the same tap water. The macropore was packed by pouring six small spoons of sand in the PMMA tube, pulling up the PMMA tube, and compressing the sand using a metal stick with a diameter that matched the inner diameter of the tube (16 mm). The packing procedure resulted in an average bulk density of 1.63 $g\ cm^{-3}$ and 1.64 $g\ cm^{-3}$ for the matrix and macropore domain, respectively. The associated porosities are 0.39 $cm^3\ cm^{-3}$ and 0.38 $cm^3\ cm^{-3}$ for the matrix and macropore domain, respectively. The resulting water content was calculated from the weight of the added water and was 0.16 $cm^3\ cm^{-3}$ in the matrix domain and 0.05 $cm^3\ cm^{-3}$ in the macropore domain. To monitor the temporal development of the pressure head during infiltration, we installed three tensiometers at 320 mm, 200 mm, and 80 mm depth below the top of the column (T1, T2, and T3 in Figure 3.1).

The two materials used to prepare the matrix and macropore domain were selected because their soil hydraulic properties (see Table 3.1) were approximately known from previous studies (Bechtold et al., 2011; Breede, 2013). However, the previously reported hydraulic properties were not consistent with the known initial water content and the measured initial pressure head distribution in the column. This resulted in a significant mismatch between simulated and measured electrical resistivity. Therefore, we adapted the hydraulic properties of both domains manually (Table 3.1) to match the initial water content and pressure head of the packed material and the temporal development of the measured electrical resistivity and anisotropy.

Table 3.1: Original and adapted hydraulic properties of the material of matrix and macropore domain.

Hydraulic properties	Macropore		Matrix	
	Original	Adapted	Original	Adapted
θ_s $(cm^3\ cm^{-3})$	0.4	0.4	0.349	0.4
θ_r $(cm^3\ cm^{-3})$	0.05	0.05	0.145	0.05
α (cm^{-1})	0.035	0.05	0.017	0.08
n	8	8	4.91	4.91
K_s $(cm\ day^{-1})$	3888	5500	3.96	21.5

3.1.3   *Electrical Anisotropy Measurements*

To determine the anisotropy in electrical resistivity, we made measurements in two directions (horizontal and vertical), as illustrated in Figure 3.1. To determine the resistivity in vertical direction, the current electrodes were located at 360 mm and 40 mm depth below the top of the column (E1 and E8 in Figure 3.1) and the potential electrodes were located at 280 mm and 120 mm depth below the top of the column (E2 and E7 in Figure 3.1). To determine the resistivity in horizontal direction, the current electrodes (E3 and E6 in Figure 3.1) and potential electrodes (E4 and E5 in Figure 3.1) were located around the circumference in the middle of the column at 200 mm depth below the top of the column. The geometry factors for the horizontal and vertical electrode configurations that are required to convert the measured electrical resistance into electrical resistivity were obtained from a measurement where the entire column was filled with water with a known electrical resistivity. In this study, we define anisotropy, A, as:

$$\text{A} = \frac{\rho_{\text{horizontal}}}{\rho_{\text{vertical}}} \tag{3.1}$$

We used the following procedure to infiltrate tap water into the macropore domain during electrical measurements. First, we inserted a PMMA tube with a length of 50 mm and an outer diameter of 20 mm to a distance of 15 mm in the macropore domain and fixed its position. This tube ensured that water infiltration occurred in the macropore domain only and avoided that water redistributed on the entire surface of the column. A syringe pipette (Thermo Scientific) with a volume of 10 cm^3 was used to create a constant head of 2.5 cm within the tube. Although water moved in the vertical direction initially, lateral flow was observed on the outside of the column in the final stage of the experiment. In total, 200 cm^3 of tap water was infiltrated in the macropore domain within about 8 minutes. Resistivity measurements in horizontal and vertical direction were performed with a temporal resolution of 11 s during infiltration using the EIT system described above. Resistivity measurements started 2 minutes before infiltration and continued for 195 minutes.

3.2 Simulations

3.2.1 *Simulation of Infiltration in Artificial Macropore*

We simulated infiltration in an artificial macropore using the HYDRUS 2D/3D code (Šimůnek et al., 2008), which solves the pseudo-three-dimensional axisymmetric Richards' Equation (Richards, 1931) that describes the movement of water in porous media. Richards' Equation is a combination of the continuity Equation for water flow with the flow Equation of Buckingham-Darcy for unsaturated soils and can be written as follows:

$$\frac{\partial \theta(h)}{\partial t} = \frac{\partial}{\partial x}\left[K(h)\left(\frac{\partial h}{\partial x}\right)\right] + \frac{\partial}{\partial z}\left[K(h)\left(\frac{\partial h}{\partial z} + 1\right)\right] \tag{3.2}$$

where θ is the volumetric water content ($cm^3\ cm^{-3}$), t is the time (day), z is the vertical space coordinate (cm, positive upward), x is the radial coordinate (cm), h is the pressure head (cm), and K is the hydraulic conductivity ($cm\ day^{-1}$). To solve Richards' Equation, the water retention function $\theta(h)$, the hydraulic conductivity function K(h), and the initial and boundary conditions need to be defined. In this study, we used the MvG model (Mualem, 1976; van Genuchten, 1980) to describe the water retention function and hydraulic conductivity function for h $\leq$ 0:

$$S_e(h) = \frac{\theta(h) - \theta_r}{\theta_s - \theta_r} = 1 + \frac{1}{[1 + |\alpha h|^n]^m} \tag{3.3}$$

and

$$K(h) = K_s S_e(h)^{0.5}\left[1 - (1 - S_e(h)^{1/m})^m\right]^2 \tag{3.4}$$

with

$$m = 1 - \frac{1}{n} \tag{3.5}$$

in these Equations, S_e is the effective saturation (-), K_s is the saturated hydraulic conductivity ($cm\ day^{-1}$), θ_r and θ_s are the residual and saturated water contents ($cm^3\ cm^{-3}$), respectively, α is related to the inverse of the air-entry pressure (cm^{-1}), and n is a measure of the width of the pore-size distribution.

The model domain was based on the dimensions of the experimental setup presented above. Because of the axisymmetric approach, the domain extended 45 mm in x-direction and 400 mm in z-direction (i.e. one half of the vertical cross-section). Two vertical regions (see Figure 3.5) were created to represent the macropore (10 mm width) and the matrix domain (35 mm width) and these two regions were parameterized with different soil hydraulic properties (Table 3.1). The model domain was discretized into 15000 nodes over the entire flow domain with a regular grid spacing of 4 mm in vertical and 0.3 mm in horizontal direction. The pressure head was initialized to -26 cm for all nodes based on tensiometer measurements in the actual experiment. We used a time-variable boundary condition at the top of the column across the width of the macropore. A pressure head of 2.5 cm was applied for 6.77 minutes, after which the boundary condition was switched to a no-flow boundary condition. This infiltration duration was selected to achieve the same infiltration amount as in the actual experiment (200 cm^3). All other boundaries of the model domain were no-flow boundaries. Water infiltration and redistribution was simulated for 43.2 minutes, and 41 water content distributions at regular time increments of 1.08 minutes were subsequently selected to simulate electrical resistivity measurements.

3.2.2 *Petrophysical Model*

To link water content distributions to electrical resistivity distributions, we used the petrophysical relationship of Archie (1942):

$$\frac{1}{\rho} = \sigma = F\sigma_w(\frac{\theta}{\phi})^n \tag{3.6}$$

where F denotes the formation factor, σ_w is the electrical conductivity of water (S^{-1} m), n is the saturation exponent, θ is the volumetric water content (cm^3 cm^{-3}), and ϕ is the porosity (cm^3 cm^{-3}). The parameters of this petrophysical model were estimated using TDR conductivity measurements (Bechtold et al., 2010; Huisman et al., 2008) in variably saturated sample cores of both materials using the same tap water as in the macropore infiltration experiment. Conductivity measurements obtained using TDR and the associated fit of Equation 3.6 are presented in Figure 3.2, and the fitted model parameters are reported in Table 3.2.
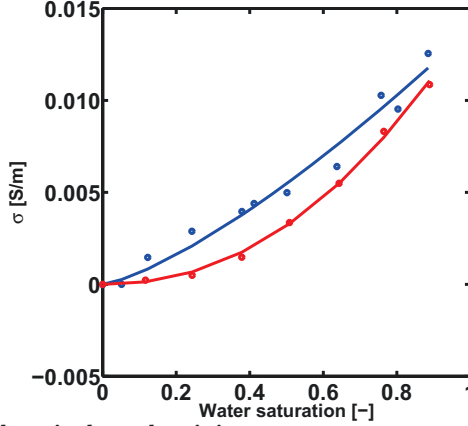
Figure 3.2: Electrical conductivity measurements made with TDR (dots) on soil sample cores and the fitted Archie's model (lines) for sand-clay (blue) mixture and sand (red) material.

Table 3.2: Petrophysical parameters of the matrix and macropore domain from TDR electrical conductivity measurements on independently packed soil sample cores.

Archie's parameters	Macropore	Matrix
n	2.1643	1.3394
F	3.2065	3.3059
ϕ $(cm^3 \ cm^{-3})$	0.378	0.387
σ_w $(\mu S \ cm^{-1})$	460	460

3.2.3 *Simulation of Anisotropy in Resistivity*

The simulated electrical transfer resistance is obtained by solving the Poisson Equation in 3D assuming an isotropic 3D electrical resistivity distribution. The electrical potential distribution within a sample for a given current injection can be obtained from:

$$\frac{\partial}{\partial x}\left(\frac{1}{\rho^*}\frac{\partial \varphi}{\partial x}\right) + \frac{\partial}{\partial y}\left(\frac{1}{\rho^*}\frac{\partial \varphi}{\partial y}\right) + \frac{\partial}{\partial z}\left(\frac{1}{\rho^*}\frac{\partial \varphi}{\partial z}\right) = I\delta(x-x_0)\delta(y-y_0)\delta(z-z_0) \quad (3.7)$$

where ρ^* is the complex electrical resistivity $(\Omega.m)$, φ is the electrical potential distribution (V), I are point current (A) sources with coordinates $(x_0, \ y_0, \ z_0)$ in m, and δ is a Dirac-delta function. This Equation can be solved for the 3D electrical potential distribution using a FEM and an appropriate set of boundary

38

conditions. We used a custom-made FEM implementation that solves the Poisson Equation in 3D following the approach of Murai and Kagawa (1985) using MATLAB (Zimmermann, 2010).

The model domain used to simulate electrical current flow in 3D was based on the dimensions of the experimental setup presented above. The height of the cylindrical model domain was 400 mm with a radius of 45 mm. It was discretized into 44880 tetrahedral elements and 8651 nodal points. The simulated temporal development of the electrical anisotropy was then obtained by simulating the horizontal and vertical transfer resistance for the electrode configurations described earlier. The required electrical resistivity distributions were obtained by relating the simulated water content distributions of the water flow model domain in 2D to the electrical flow model domain in 3D. This was achieved by searching the nearest nodal points of the hydrological model for each element midpoint of the electrical model. The electrical resistivity of each element was then calculated using Equation 3.6 and the parameters provided in Table 3.2.

3.2.4 *Anisotropy Sensitivity to Resistivity Contrast and Macropore Volume Fraction*

To test the sensitivity of the electrical anisotropy to the resistivity contrast between matrix and macropore domain and the macropore volume fraction, we performed the following simulations. First, we selected three representative values for the resistivity of the matrix domain: one for dry soil (3800 $\Omega.m$), one for moist soil (235 $\Omega.m$; similar to the resistivity of the column with artificial macropore that we used in this study), and one for a fully saturated soil (72 $\Omega.m$). For each of these three matrix domain resistivity values, seven resistivity values ranging from 10 $\Omega.m$ to 70 $\Omega.m$ were assigned to the macropore domain to represent infiltration of water with different resistivity in an empty macropore. In addition, the volume fraction of the macropore was varied from 0.01 $cm^3\ cm^{-3}$ to 0.05 $cm^3\ cm^{-3}$ for each combination of resistivity values for the matrix and macropore domain. Finally, sensitivity of the anisotropy to the electrical resistivity of the macropore and matrix was investigated in more detail for a macropore volume fraction of 0.05 $cm^3\ cm^{-3}$ by varying the macropore resistivity from 10 $\Omega.m$ to 500 $\Omega.m$ in steps of 10 $\Omega.m$ for the dry, moist, and fully saturated matrix domain.

3.3 Results and Discussion

3.3.1 *Anisotropy Sensitivity to Resistivity Contrast and Macropore Volume Fraction*

Figure 3.3 shows the simulated electrical anisotropy for three resistivity values for the matrix domain and a range of resistivity values for the macropore domain as a function of macropore volume fraction. A simple conceptual model would be that the presence of a conductive vertical macropore in a resistive matrix leads to a lower vertical resistivity as compared to the horizontal resistivity, and therefore an anisotropy value larger than 1.0. This is indeed what we found in this simple model sensitivity test. For example, when the matrix domain was dry (e.g. high resistivity of 3800 $\Omega.m$; see Figure 3.3(a)) and more conductive water was present in the macropore (e.g. 70 $\Omega.m$), an electrical anisotropy of 2.87 was obtained for a macropore volume fraction of 0.05 $cm^3\ cm^{-3}$. When more conductive water was present in the macropore, the electrical anisotropy increased up to 10.33. With decreasing macropore volume fraction, the electrical anisotropy decreased but remained high enough (>1.45) even for low macropore volume fractions when sufficient contrast in resistivity between matrix and macropore domain was present. Similar results were obtained for the moist (Figure 3.3(b)) and fully saturated case (Figure 3.3(c)). However, the change in anisotropy was not as large for the dry soil matrix due to the reduced contrast between matrix and macropore domain. The electrical anisotropy ranged from 1.02 to 1.80 for the moist matrix and from 1.00 to 1.16 for the fully saturated case.
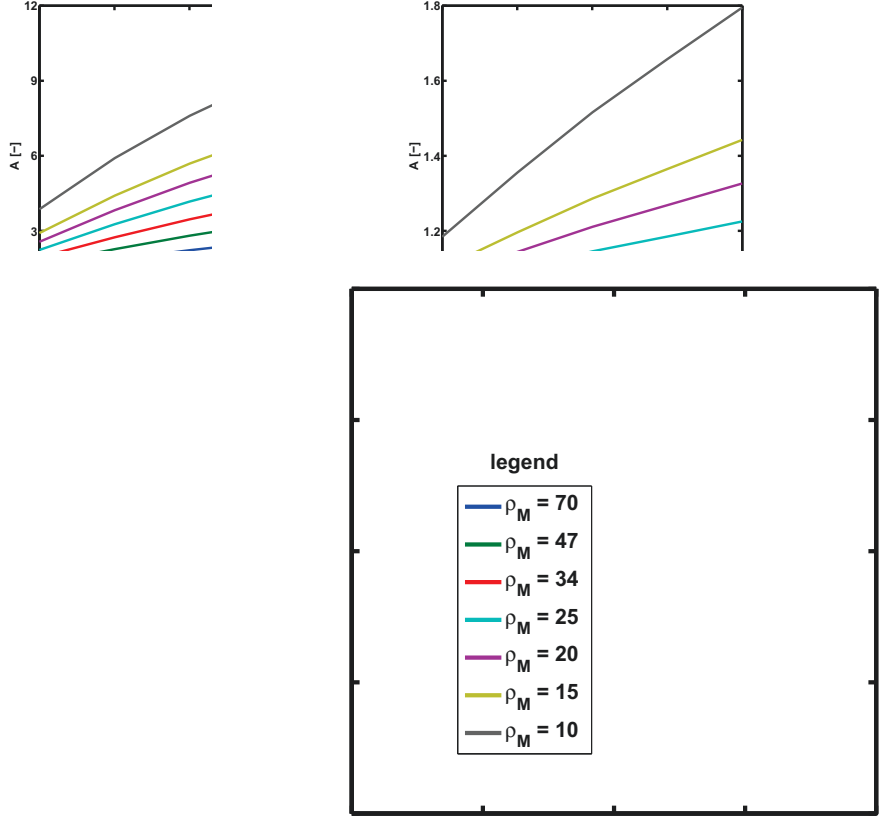
Figure 3.3: Anisotropy sensitivity test for (a) dry ($\rho = 3800$ $\Omega.m$), (b) moist ($\rho = 235$ $\Omega.m$), and (c) fully saturated ($\rho = 72$ $\Omega.m$) matrix domain and seven resistivity values (see legend) of the macropore domain as a function of macropore volume fraction. ρ_M indicates the resistivity of the macropore domain.

Figure 3.4 shows a more detailed analysis of the dependence of the simulated horizontal and vertical resistivity and the associated anisotropy on the matrix and macropore resistivity for a macropore volume fraction of 0.05 cm^3 cm^{-3}. Figure 3.4(a) and 3.4(b) confirm that the anisotropy was indeed considerably larger than 1 when the contrast in resistivity of the macropore and matrix domain was sufficiently high as is the case for the dry matrix. In the case of the moist matrix (Figure 3.4(c) and 3.4(d)), anisotropy larger than 1.2 only occurred when the macropore resistivity was below 30 $\Omega.m$. For higher macropore resistivities, the anisotropy was close to 1 even when the macropore resistivity was larger than the matrix resistivity. In the case of the fully saturated matrix (Figure 3.4(e) and 3.4(f)), the simulated anisotropy was always smaller than 1.2 and a minimum of the anisotropy was observed when the macropore domain was slightly less resistive (40-

41

60 $\Omega.m$) than the matrix domain (72 $\Omega.m$). These simulation results show that the simple conceptual model used earlier is not valid for small contrasts in macropore and matrix resistivity. This is associated with the sensitivity distributions of the electrode configurations used to measure the horizontal and vertical resistivity, as was also pointed out by Moysey and Liu (2012).

The results of this sensitivity analysis have implications for the interpretation of the electrical anisotropy associated with infiltration in the artificial macropore used in this study. In contrast to more realistic field conditions, the artificial macropore is filled with soil material in our experimental setup. This reduces the contrast between matrix and macropore domain and the resulting anisotropy values. Therefore, the modeling and experimental results for the artificial macropore presented hereafter should be considered as a conservative representation of anisotropy signals that can potentially be observed in the field.

3.3.2 *Numerical Results*

Figure 3.5 shows the simulated water content distributions for infiltration into the artificial macropore. At time1, water infiltration was started and water quickly moved vertically in the macropore domain. Some lateral flow into the soil matrix was also simulated. When infiltration into the macropore stopped at time6, the entire macropore was almost saturated. From time7 to time23, water redistributed from the macropore into the matrix. After time23, the macropore was completely dry again in the simulation and water only redistributed in the matrix domain.

Figure 3.4: Simulated horizontal (red) and vertical (blue) resistivity (a, c, and e) and the associated anisotropy (b, d, and f) from (a and b) dry ($\rho = 3800$ $\Omega.m$), (c and d) moist ($\rho = 250$ $\Omega.m$), and (e and f) fully saturated ($\rho = 72$ $\Omega.m$) matrix domain as a function of the macropore resistivity for a macropore volume fraction of **0.05** cm^3 cm^{-3}. ρ_M indicates the resistivity of the macropore domain.
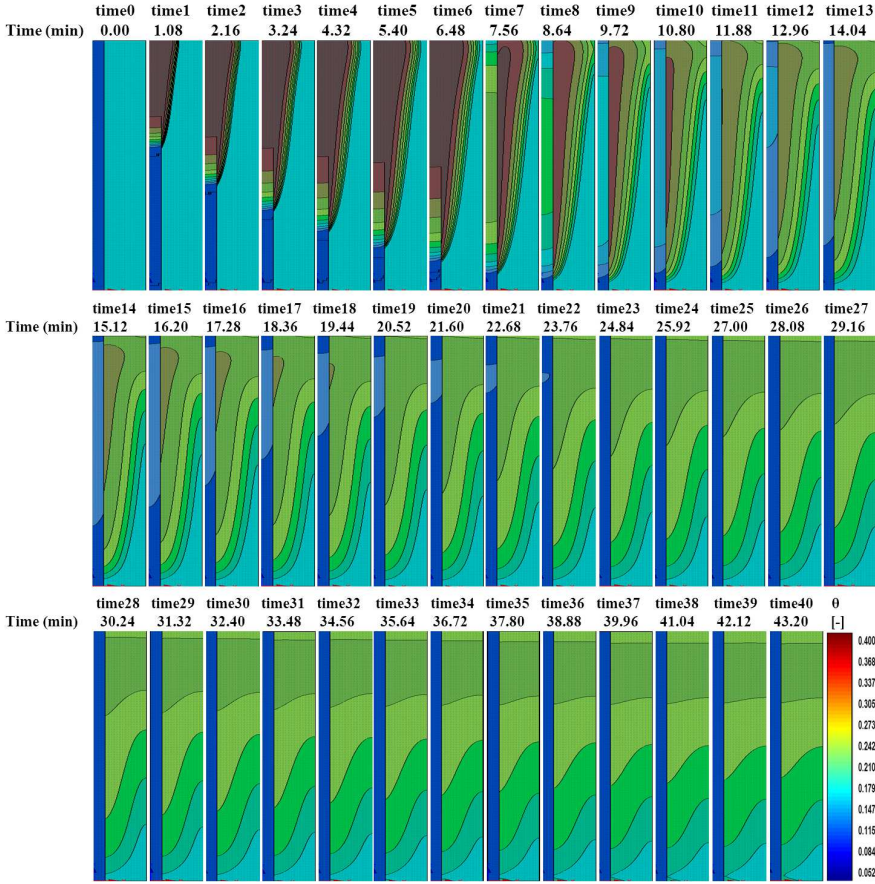
Figure 3.5: Simulated water content distributions for infiltration into the artificial macropore obtained using HYDRUS code.

Figure 3.6(a) shows the simulated horizontal and vertical electrical resistivity and the associated anisotropy is shown in Figure 3.6(b). It is evident that the simulated horizontal and vertical resistivity reacted differently because of the presence of the macropore, which led to a pronounced temporal development of the anisotropy in the resistivity. At the beginning of the experiment, the resistivity is high and a small positive anisotropy (1.081) is present because of the presence of the empty ('deactivated') macropore in the moist matrix. This anisotropy value larger than one for a resistive macropore in a less resistive matrix is consistent with the results presented in Figure 3.4(d). As soon as the infiltration process started, the flow in the macropore is activated and both the horizontal and vertical resistivity decreased strongly. The anisotropy also decreased, which contradicts the simple conceptual model that anisotropy is much larger than one when conductive macropores are present. As discussed for the results of the sensitivity test in sec-

tion 3.3.1, this is related to the small contrast in macropore and matrix resistivity when an artificial macropore is used and the effect of the sensitivity distribution of the electrode configurations. The simulated minimum in the anisotropy is 0.89, which is lower than the simulated values presented in Figure 3.4(d). We attribute this to the water exchange between macropore and matrix that enlarges the conductive region around the macropore (time5 and time6 in Figure 3.5). As soon as infiltration into the macropore stopped, water re-distributed to the matrix domain and the anisotropy increased again towards similar values as observed at the beginning of the simulation. Overall, these simulations show that water flow in macropores leads to a distinct temporal change in the anisotropy of the electrical resistivity that would not occur in soils without macropore flow.

(c)   (d)

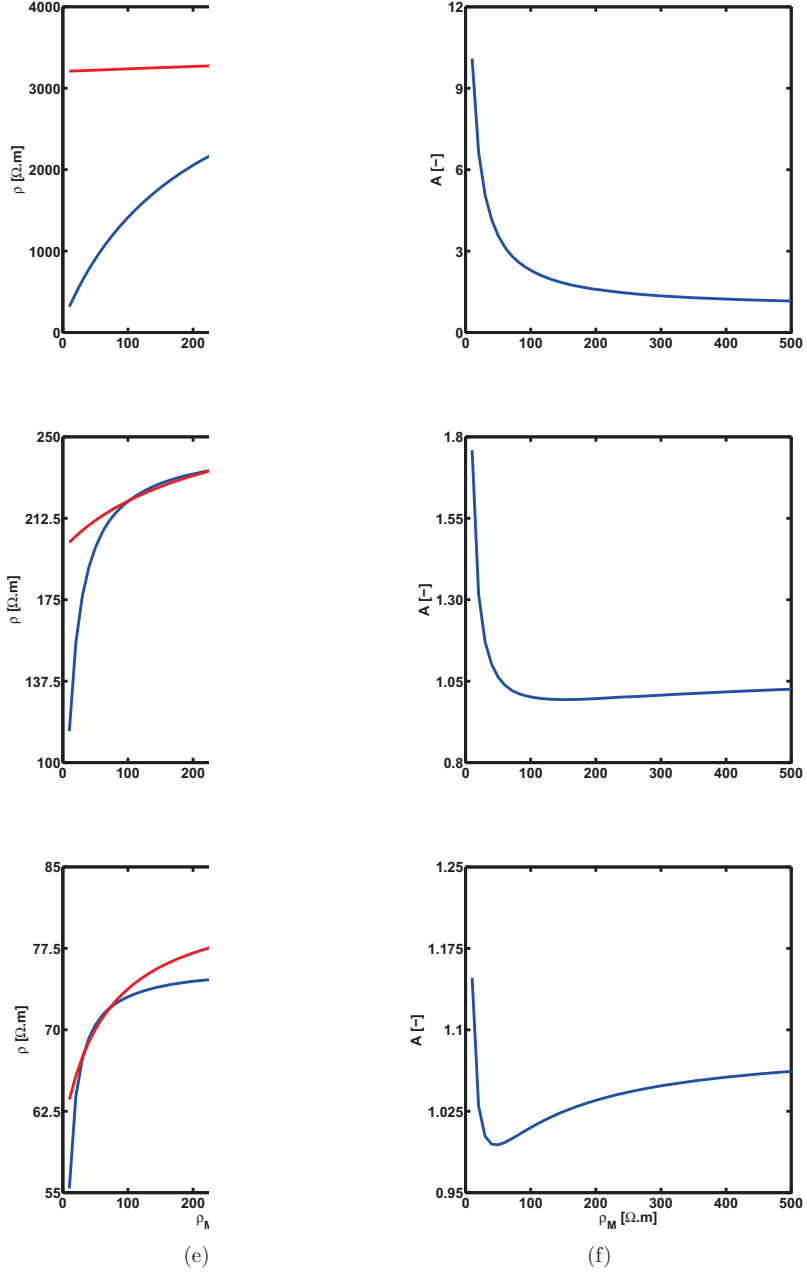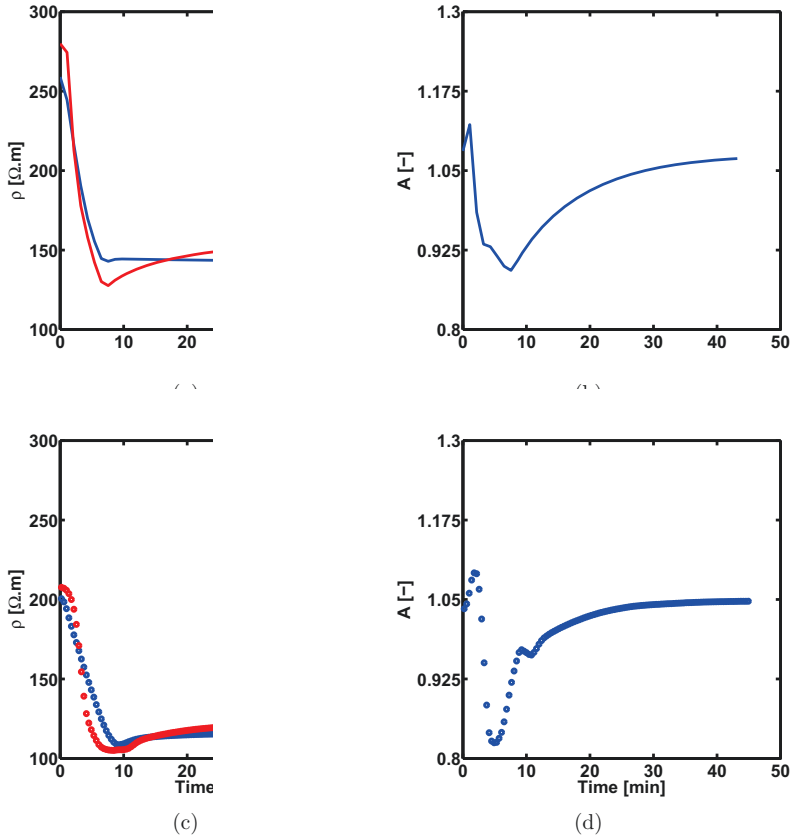**Figure 3.6: Horizontal (red) and vertical (blue) electrical resistivity (a and c) and the associated anisotropy (b and d) from (a and b) simulations and (c and d) measurements of water infiltration in an artificial macropore.**

3.3.3 *Sensitivity of Anisotropy to Changes in Hydraulic Properties*

The sensitivity of the anisotropy to changes in hydraulic properties was analyzed by varying the parameters provided in Table 3.1 for both the macropore and matrix domain. Hydraulic properties were decreased and increased by 10 % relative to the original values (see Table 3.1) and the hydrological and electrical resistivity simulations were repeated. The simulated anisotropy response was generally not sensitive to changes in the hydraulic properties of the macropore (Figure 3.7(a), 3.7(c), 3.7(e), 3.7(g) & 3.7(i)). In contrast, the anisotropy was more sensitive to changes in hydraulic properties of the matrix (Figure 3.7(b), 3.7(d), 3.7(f), 3.7(h) & 3.7(j)), especially towards changes in the air-entry value α (Figure 3.7(b)) and the saturated water content θ_s (Figure 3.7(j)). This sensitivity further showed that the simulated anisotropy in the initial phase and towards the end of the experiment was not much affected by changes in the hydraulic properties. For example, the minimum anisotropy was almost identical for all model runs. The main differences in the simulated temporal development of the anisotropy where observed in the phase where water redistributed in the matrix domain. In our model setup, the water flux associated with this redistribution through unsaturated flow is apparently mainly controlled by the α and θ_s parameters.

(e)   (f)
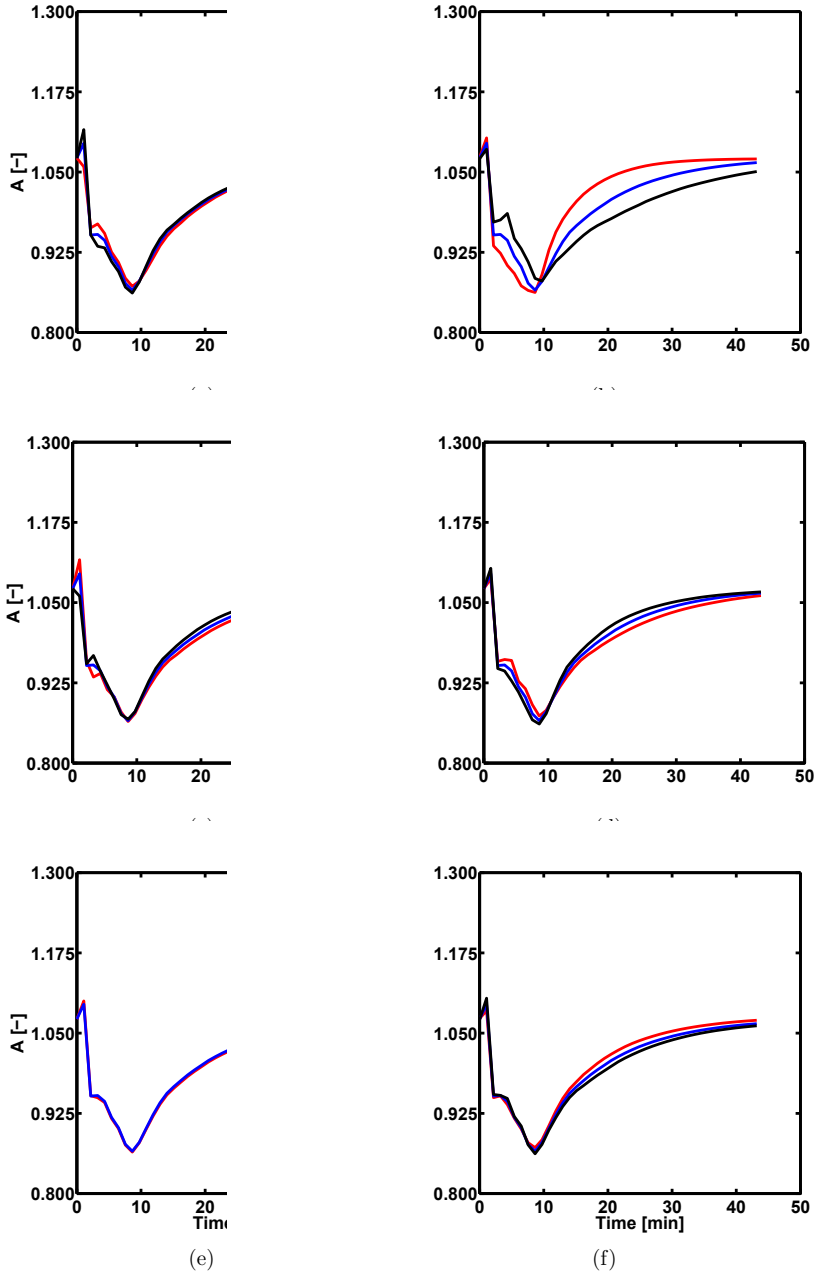
Figure 3.7: This is a continued Figure (cont.)
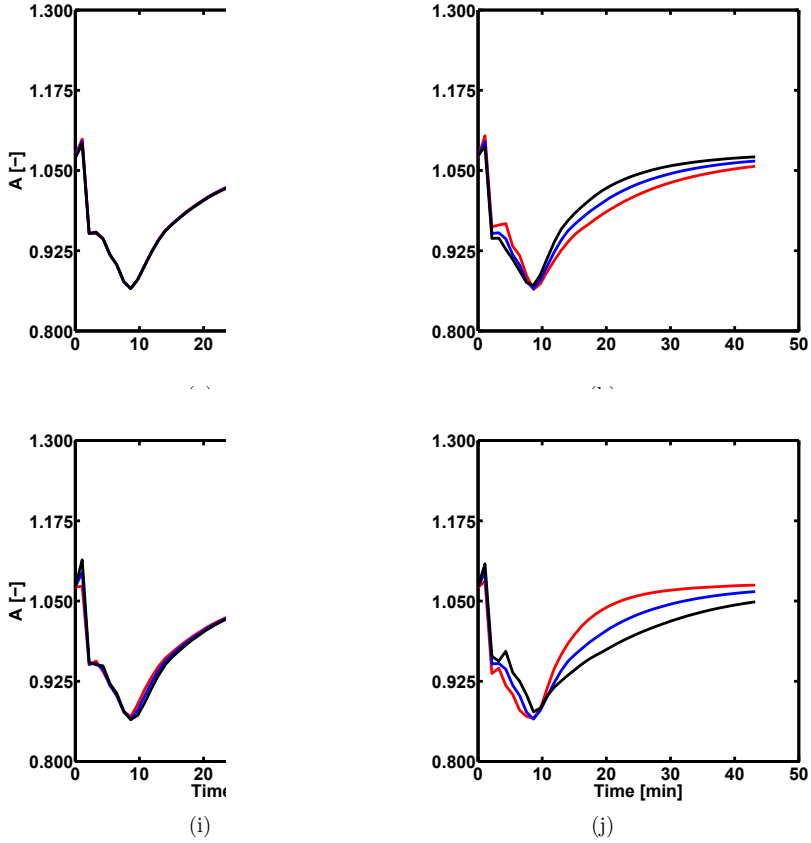
Figure 3.7: Sensitivity analysis of the anisotropy to changes in the hydraulic properties by increasing (black) and decreasing (red) 10 % of the following parameters: (a) α, (c) K_s, (e) n, (g) θ_r, and (i) θ_s of the macropore domain and (b) α, (d) K_s, (f) n, (h) θ_r, and (j) θ_s of the matrix domain. Blue lines correspond with the original hydraulic parameters provided in Table 3.1. The n parameter of the macropore domain (e) could not be increased by 10 % because of numerical issues with the HYDRUS model.

3.3.4 *Measurement Results*

Figure 3.6(c) shows the horizontal and vertical electrical resistivity measured during macropore infiltration and redistribution. The associated temporal development of the anisotropy is shown in Figure 3.6(d). Clearly, the observed and modeled resistivity in horizontal and vertical direction show similar behavior (Figure 3.6(a) & 3.6(c)). Both the measured and modeled horizontal resistivity was higher than the vertical resistivity before infiltration was started, as expected from the results presented in Figure 3.4. When water infiltrated in the macropore, a strong decrease in both measured and modeled horizontal and vertical resistivity was observed. The measured anisotropy also showed similar behavior as compared with the simulation results: a quick decrease until the end of infiltration in the macropore and a subsequent slower increase towards the initial anisotropy value observed without water flow in the macropore. The consistency between measured and modeled data further increased our confidence that it is possible to understand the temporal development of resistivity anisotropy associated with macropore preferential flow processes. Clearly, these distinct temporal signatures of anisotropy resistivity open up perspectives for the field characterization of such processes using appropriate square-electrode configurations (Greve et al., 2012b) or anisotropic inversion of ERT data (Kenkel et al., 2012).

Although the general behavior of measured and modeled resistivity and anisotropy are similar in Figure 3.6, some discrepancies are also apparent. For example, there is a considerable difference in the value of the simulated and measured resistivity (i.e. the model predicted higher resistivity values). Such discrepancies can be expected when soil hydraulic properties and petrophysical parameters are not directly determined on the same sample, but instead are taken from previous experiments on the same material. In addition, the packing of the column and specifically the macropore was not straightforward and heterogeneity might have been introduced due to inhomogeneous packing.

3.4 Conclusions

In this work, we showed that infiltration in an artificial macropore resulted in distinct differences in the temporal development of electrical resistivity measurements in two perpendicular directions and thus in the 'macroscopic' anisotropy in electrical resistivity. The general behavior of the temporally varying anisotropy was similar in our model simulations and measurements. We conclude that temporal variations in anisotropy in electrical resistivity can be used to identify the

existence of flow in macropores. Since changes in water redistribution in the soil matrix led to distinctly different temporal changes in electrical resistivity in a model sensitivity study, we also think that anisotropy can be used to quantify exchange between macropore and soil matrix in future studies. This would be an important contribution since this information is notoriously difficult to obtain using traditional methods to investigate macropores.

In future work, it will be interesting to study macropore preferential flow in an anisotropic ERT framework (e.g. Kenkel et al., 2012, 2013) instead of the direct measurement of horizontal and vertical resistivity used in this study. For example, the temporal development of the electrical resistivity can be imaged during water infiltration in an artificial macropore.

Chapter 4

IMAGING OF ELECTRICAL ANISOTROPY ASSOCIATED WITH MACROPORE INFILTRATION PROCESSES: A 2D LABORATORY EXPERIMENT WITH AN ARTIFICIAL MACROPORE[1]

In the previous Chapter 3, we presented flow experiments using an artificial macropore to understand the effect of water flow in macropores on the electrical anisotropy. The results showed that measurements of the horizontal and vertical resistivity reacted differently when water flowed in the macropore, which led to electrical anisotropy. The observed electrical anisotropy was in good agreement with simulation results from 3D axisymmetric hydrological modelling using the HYDRUS software package and electrical forward modelling using custom-made MATLAB software. Overall, this first experiment confirmed that monitoring of the electrical anisotropy can be used to identify macropore flow. However, the observed changes in anisotropy were not in agreement with available conceptual models (e.g. Moysey and Liu, 2012) because the chosen electrode arrangement does

---

[1]Adapted from Al-Hazaimay S., J. Kenkel, E. Zimmermann, A. Kemna, H. Vereecken, and J.A. Huisman. Imaging of electrical anisotropy associated with macropore infiltration processes: A 2D laboratory experiment with an artificial macropore. Manuscript will be submitted to Vadose Zone Journal.

not allow a correct determination of the effective horizontal and vertical electrical resistivity, which can only be overcome by the use of an imaging framework. In a next step, the objective of this Chapter (4) is therefore to use anisotropic electrical imaging instead of direct measurement of horizontal and vertical resistivity to investigate flow processes associated with macropores. To this end, we performed time-lapse ERT measurements on a Hele-Shaw tank with an artificial macropore using a novel fast ERT instrument that allows the acquisition of 10 ERT data sets per second. These ERT data sets are inverted to obtain images of the anisotropic electrical resistivity using a coarse inversion grid so that flow processes remain unresolved and appear in the electrical anisotropy. We interpret temporal dynamics in electrical anisotropy in terms of preferential flow processes.

4.1 Measurements

4.1.1 *Hele-Shaw Tank with Artificial Macropore*

We built a Hele-Shaw tank with side lengths of 300 mm and a thickness of 20 mm (see Figure 4.1) and filled it with two different materials to prepare a background matrix with an artificial macropore. The top side of the tank was designed to be removable so that the tank can be packed with soil material. For the matrix domain, we used fine sand (F34, Quarzwerke Frechen GmbH, Frechen, Germany) with a mean grain size of 0.2 mm. For the macropore domain, we used glass beads with a diameter of 4 mm (Merck KGaA, Darmstadt, Germany). The following procedure was used to prepare the tank. First, we inserted a rectangular metal stick with side lengths of 20 mm and a height of 300 mm in the middle of the tank and fixed its position. This metal stick was selected to create an artificial macropore that occupied 6.7 % of the entire volume of the tank. Next, the sand that makes up the matrix domain was prepared by adding 286 cm^3 of tap water to 2671 g of fine sand. The electrical conductivity of the tap water was 463 $\mu S\ cm^{-1}$ at 20°C. The matrix domain was packed in layer increments of approximately 30 mm thickness by firm pressing. For the macropore domain, we mixed 191 g of glass beads with 10 cm^3 of the same tap water. The macropore was packed after pulling out the metal stick completely by repeatedly adding six small spoons of glass beads in the macropore cavity, and applying some pressure using the rectangular stick. The packing procedure resulted in average bulk densities of 1.65 $g\ cm^{-3}$ and 1.64 g cm^{-3} for the macropore and matrix domain, respectively. The associated porosity is 0.38 $cm^3\ cm^{-3}$ for both the matrix and macropore domain. The resulting water content was calculated from the weight of the added water and was 0.17 $cm^3\ cm^{-3}$

in the matrix domain and 0.09 cm^3 cm^{-3} in the macropore domain.

The same tap water as used in the sample preparation was used to infiltrate water in the macropore domain. For this, a hole with a diameter of 14 mm was made in the middle of the top side of the tank directly above the macropore domain. A funnel was placed in this hole to infiltrate water into macropore. In total, 100 cm^3 of water was infiltrated in the macropore domain within 27 s. As expected, water initially moved quicker in the vertical direction than in the lateral direction because the funnel assured that water only infiltrated in the macropore domain.

The Hele-Shaw tank was equipped with forty electrodes for ERT measurements that were numbered as shown in Figure 4.1. All electrodes were brass electrodes and had a radius of 6 mm and a length of 57 mm. Fourteen electrodes were used on the left and right side, and twelve electrodes were used on the top side. All electrodes were equally separated with a distance of 20 mm from each other and the corners of the tank and were located in the center of the top and side walls. In addition, electrodes 17 and 18 were separated with a distance of 20 mm from the artificial macropore. Electrodes on the left and right side of the tank were installed before packing to ensure good material contact. These electrodes were placed in plastic cable glands with an inner diameter of 7 mm so that the electrode tips were flush with the inner wall of the tank. In contrast, the electrodes on the top side were installed inside the plastic glands so that twice the diameter is inserted in the sample when the top side of the Hele-Shaw tank is installed after sample preparation.

4.1.2 *Electrical Resistance Measurement Equipment*

The electrical measurements were made using a similar EIT system (Zimmermann et al., 2008b) as used in section 2.1.1 with some modifications (Zimmermann et al., 2013) that enable fast electrical resistivity measurements in order to monitor quick macropore flow processes. To reduce EIT measurement time, mathematically orthogonal signals were used to inject current simultaneously in all current electrodes and inverse multiplexing was used to separate the contribution of each injection to the measured potential at any potential electrode. This approach thus replaces n current injections by one simultaneous injection at all current electrodes, which reduces the measurement time by a factor of n. In order to create orthogonal signals, we chose sine waves with frequencies of 250 Hz, 300 Hz, 350 Hz, 400 Hz, and 450 Hz at the electrodes I1, I2, I3, I4, and I5 in Figure 4.1, respectively. The modified EIT system was equipped with ten multiplexer cards each with four electrode modules. Three of these electrode modules were used for potential mea-
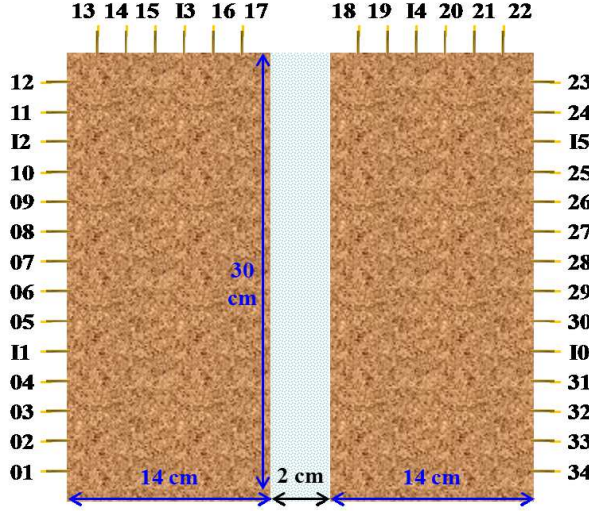
Figure 4.1: Experimental setup with dimension of the tank filled with sand in the matrix domain and glass beads in the macropore domain. Numbers I0 to I5 indicate the position of the current electrodes, whereas numbers 01 to 34 indicated positions of voltage electrodes.

surements. The fourth electrode module was redesigned to inject current with common function generators (Agilent 33120A) and integrated shunt resistors and amplifiers were used to measure the strength of the injected current. It should be noted that the potential measurements are made with respect to the system-ground.

4.1.3 *Electrical Resistance Measurements*

Time-lapse ERT measurements were performed in the tank during water infiltration in the macropore domain. We used electrodes I0, I1, I2, I3, I4, and I5 for the current injections and electrodes 01 to 34 for the voltage measurements (see Figure 4.1). Electrode I0 was the sink for all current injections and was connected to ground potential. We used this low amount of current electrodes to quickly obtain a coarse image of preferential flow processes as detailed above. In post-processing, the measured electrical currents and voltages are converted to transfer resistances for selected four-electrode configurations following Zimmermann et al. (2013). For the current injection, skip-zero electrode configurations were selected (i.e. I1-I2 in Figure 4.1, see Slater et al., 2000) and associated voltages were calculated for all potential electrodes (01 to 34) relative to ground. In a next step, skip-zero electrode configurations were selected for the potential measurements, which resulted

in 204 combinations of current injection and potential measurements per data set that were subsequently used in the anisotropic ERT inversion (see Table 4.1). ERT measurements were started 40.5 s before the infiltration process and continued for 1200 s where 10 data sets (i.e. frames) were recorded per second. This resulted in 12000 data sets of transfer resistances which were inverted to image the temporal development of the electrical anisotropy during infiltration.

Table 4.1: Electrode pairs used for current injections and potential measurements.

Configuration	Current	Potential
	I1-I2, I2-I3, I3-I4, I4-I5, I5-I0, I0-I1	01-02, 02-03, 03-04, 04-05, 05-06, 06-07, 07-08, 08-09, 09-10, 10-11, 11-12, 12-13, 13-14, 14-15, 15-16, 16-17, 17-18, 18-19, 19-20, 20-21, 21-22, 22-23, 23-24, 24-25, 25-26, 26-27, 27-28, 28-29, 29-30, 30-31, 31-32, 32-33, 33-34, 34-01

4.2 Inversion Techniques

4.2.1 *Imaging of Anisotropic Electrical Resistivity*[2]

In order to image the temporal dynamics of preferential flow processes during water infiltration, we inverted the ERT data using CRTOMO. This is a finite-element based, smoothness-constraint inversion code based on Kemna (2000) that uses log-transformed impedances as data and log-transformed electrical conductivity (i.e. reciprocal of resistivity) as model parameters. CRTOMO uses a standard Gauss-Newton procedure for non-linear inverse problems to find the smoothest electrical conductivity distribution that fits the measured resistance data to a specific error level (ϵ). To account for anisotropic conductivity, the code of Kemna (2000) was extended by assuming a diagonal conductivity tensor (see Equation 4.1) in Cartesian coordinates, which corresponds to the following diagonal resistivity tensor:

$$\frac{1}{\boldsymbol{\sigma}} = \boldsymbol{\rho} = \begin{pmatrix} \rho_x & 0 & 0 \\ 0 & \rho_y & 0 \\ 0 & 0 & \rho_z \end{pmatrix} \tag{4.1}$$

---

[2]The development and implementation of anisotropic electrical resistivity tomography is part of the PhD thesis of Johannes Kenkel (University of Bonn). The approach is outlined here for sake of completeness only.

where $\boldsymbol{\sigma}$ is the electrical conductivity tensor, $\boldsymbol{\rho}$ is the electrical resistivity tensor in which ρ_x, ρ_y, and ρ_z are the electrical resistivity in x-, y-, and z-direction, respectively. This required the modification of the forward model (Kenkel et al., 2012), the sensitivity computation, and the inverse procedure (Kenkel et al., 2013). In this study, we define anisotropy, A, as:

$$A = \frac{\rho_X}{\rho_Z} \tag{4.2}$$

it should be noted that the anisotropy factor A is presented in logarithmic scale in the following $(\log_{10}(A) = \log_{10}(\rho_X) - \log_{10}(\rho_Z))$. Therefore, $\log_{10}(A) = 0$ indicates an isotropic medium, and $\log_{10}(A)$ values much higher or lower than zero indicate anisotropy.

The objective function being minimized during ERT inversion consists of two terms that represent the data misfit and the model roughness, which are balanced by the regularization parameter (λ):

$$\Psi(\boldsymbol{m}) = \|\boldsymbol{W}_\epsilon[\boldsymbol{d} - \boldsymbol{f}(\boldsymbol{m})]\|^2 + \lambda\|\boldsymbol{R_m}(\boldsymbol{m})\|^2 \tag{4.3}$$

where $\boldsymbol{m}$ is the model parameter vector ($\boldsymbol{m}_j = \log_{10}\sigma_j$) in which σ varies over a discrete j^{th} pixel parametersation of number of model parameters $\boldsymbol{M}$ (j=1, ..., $\boldsymbol{M}$), $\boldsymbol{d}$ is the data vector, $\boldsymbol{f}(\boldsymbol{m})$ denotes the finite-element forward model operator (Poisson Equation), $\boldsymbol{R}$ is a first-order matrix (roughness) operator for $\boldsymbol{m}$, and $\boldsymbol{W}_\epsilon$ is a data weighting matrix that represents the measurement error ϵ_i of each of the N resistance measurement in a diagonal form according to:

$$\boldsymbol{W}_\epsilon = diag(1/\epsilon_1, ..., 1/\epsilon_N) \tag{4.4}$$

To regularize the additional degrees of freedom associated with anisotropy, the most isotropic model is sought by adding an anisotropy penalty term in the objective function similar to Pain et al. (2003). In the extended anisotropic inversion scheme, a spatial smoothness constraint is imposed for each component of the resistivity tensor. Accordingly, anisotropic smoothing of the model is required, which can be achieved by separating the matrix $\boldsymbol{W}$ with respect to X- and Z-direction and introducing two real smoothing parameters α_x and α_z (Kemna, 2000) where α_x and α_z are chosen from the interval between (0, 1]. The ratio of α_x and α_z should ideally follow the ratio of the correlation lengths of the subsurface structure with respect to horizontal and vertical directions, respectively. Unfortunately, this

information is not known and likely temporally variable in case of anisotropy associated with flow processes. In this study, we arbitrarily fixed these two smoothing parameters to 1. During the inversion, an optimum regularization parameter λ has to be found for each iterative step so that the measured data are best reconstructed without introducing artifacts or excessive smoothing. This is achieved using a univariate search method (Kemna et al., 2014) in which the model is updated by solving a linear system of Equations (see Equation 6 in Kemna et al., 2002) with different trial values of the regularization parameter. The criterion to stop the iterative process is that the data misfit reaches a value of N (i.e. number of resistances measurement) for a maximum possible value of λ. More details about our approach to ERT inversion can be found in Kemna (2000), Kemna et al. (2002), and Binley and Kemna (2005).

4.2.2 *Mesh Discretization*

The modelling domain was discretized into 60x60 (3600) square elements in the X-Z plane (see Figure 4.2(a)) with a side length of 5 mm and 3721 nodes. We used Neumann boundary conditions with no current flow for all domain boundaries. For the sake of anisotropic inversion, we used the two coarse inversion meshes shown in Figure 4.2(b) and 4.2(c) with the corresponding element numbering for proper identification. The first mesh consisted of 9 elements (mesh9) with a side length of 100 mm and the second mesh consisted of 25 elements (mesh25) with a side length of 60 mm. The idea behind this coarse discretization is to produce an inversion grid that is coarser than the size of the macropore so that flow processes remain unresolved and appear only in the anisotropy of the electrical resistivity. Although the electrode configurations used in the ERT data acquisition in the Hele-Shaw tank partly allow to resolve the electrical resistivity changes associated with infiltration in the macropore, we choose to use these coarse inversion grids because we expect that this is more representative for field applications where macropore flow processes likely cannot be resolved with typical electrode separations of 100 mm or more. The two different inversion grids were selected to investigate how the anisotropic inversion results are affected by the extent to which the macropore region is resolved.
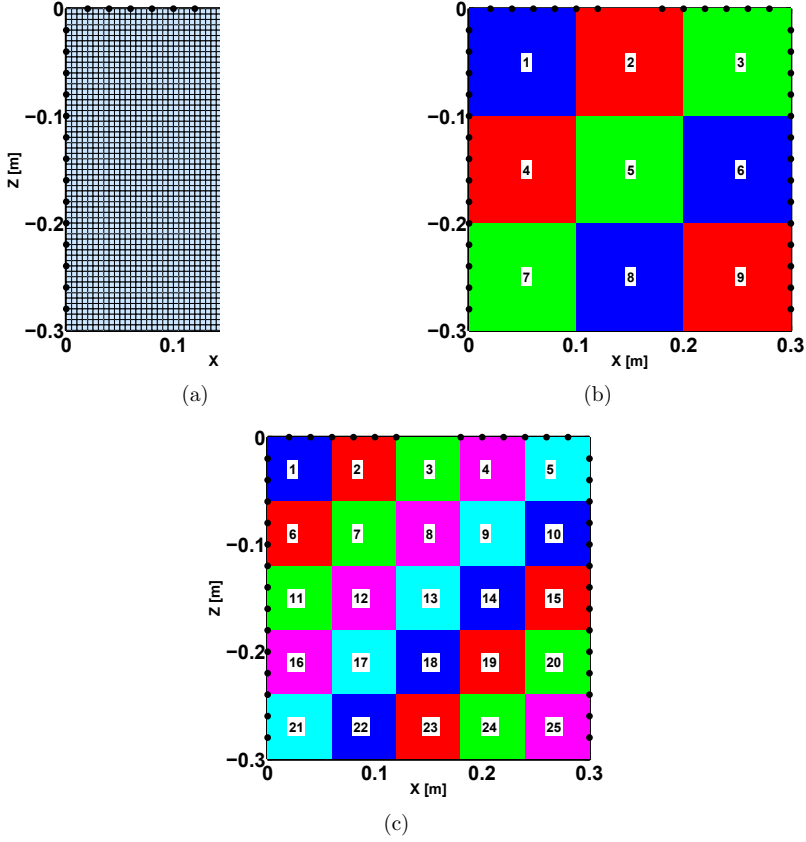
Figure 4.2: (a) Discretization used for ERT forward modelling, and discretization used for ERT inversion: mesh9 (b) and mesh25 (c). All elements have been numbered for proper identification. The position of all electrodes is indicated with solid black circles.

4.3 Data Error Assessment

Assessment of data errors is important in ERT inversion because it is commonly used to determine the appropriate extent to which the measured transfer resistances need to be described during model inversion (see Equation 4.3). Data error quantification is often based on reciprocal measurements where current and potential electrodes are interchanged for any four-electrode configuration (Koestel et al., 2008; LaBrecque et al., 2002; Slater et al., 2000) because such an interchanging of current and potential electrodes should not affect the resistance measurement. Therefore, the difference in measured resistance between forward (normal) and

reciprocal measurements (Z_n and Z_r, respectively), also referred to as the reciprocal error (e), can be used to approximate errors in ERT data (Slater et al., 2000):

$$e = Z_n - Z_r \tag{4.5}$$

In this study, we used a fast data acquisition system that is not able to make reciprocal measurements. Instead, we propose to use the symmetry of our experimental setup (see Figure 4.1) for the data error quantification using resistance measurements on the measurement tank filled with water of different electrical conductivity (40, 159.3, and 439 μS cm^{-1}). These water conductivities were selected to cover the range of measured transfer resistances that we expect in the macropore infiltration experiment. We performed the following steps for each transfer resistance measurement. First, electrical current was injected through one electrode pair (e.g. normal measurement I1-I2 in Figure 4.1). Due to the tank symmetry, the symmetrical (reciprocal) current injection electrode pair for I1-I2 is I5-I0. Next, we calculated resistances using skip-zero (e.g. 01-02), skip-one (e.g. 01-03), and skip-two (e.g. 01-04) electrode configurations for each normal and reciprocal current injection pair. As a result, we obtained 102 symmetrical ("reciprocal") resistance measurements. This procedure was repeated for three other pairs of current electrodes (i.e. I2-I3, I3-I4, and I1-I0) and their symmetrical counterparts (i.e. I4-I5, I4-I3, and I0-I1). This resulted in 408 symmetrical resistance measurements for each selected electrical conductivity of the water. Therefore, a total of 1224 symmetrical measurements were available for data error quantification.

Slater et al. (2000) proposed to filter obvious outliers from the data before fitting an error model to the envelope of reciprocal measurements (e.g. $|e| > 0.1 * |Z|$, where Z is the mean resistance of normal and reciprocal measurements). Koestel et al. (2008) also removed obvious outliers and proposed to further process the reciprocal measurements by dividing all resistance measurements into equally sized bins (in logarithmic scale). For each bin, they proposed to calculate the mean transfer resistance and the standard deviation of the reciprocal error. To obtain the error model for our measurements, we followed a similar but slightly different approach. This approach can be summarized as follows. First, we calculated the mean value of resistances obtained from symmetrical electrode configurations and the reciprocal error according to Equation 4.5. Resistance measurements with an error of exactly zero were removed because these were measurements where the symmetrical electrode configurations had identical potential electrodes. Next, the

resistance data were separated into 15 equally sized bins and the mean resistance of each bin was calculated. Finally, the data error ϵ for each bin was quantified using:

$$\epsilon = \sqrt{\frac{1}{2} * \mathrm{mean}(e^2)} \tag{4.6}$$

LaBrecque et al. (1996) suggested the following simple model to describe data errors:

$$\epsilon = a * |Z| + b \tag{4.7}$$

where a represents a relative (dimensionless) error contribution and b is the absolute error contribution (Ω). This model was manually fitted to the binned data (see Figure 4.3), and this resulted in $a = 0.01$, and $b = 0.015$ Ω. These values are in reasonable agreement with previous studies (e.g. $a = 0.01$ and $b = 0.1$ Ω (Slater et al., 2000); $a = 0.003$ and $b = 0.026$ Ω (Koestel et al., 2008); $a = 0.028$ and $b = 0.42$ Ω (Bechtold et al., 2012)). The fitted data error model was used to define the data weighting matrix $\boldsymbol{W}_\epsilon$ (Equation 4.4) for all subsequent anisotropic ERT inversion results.
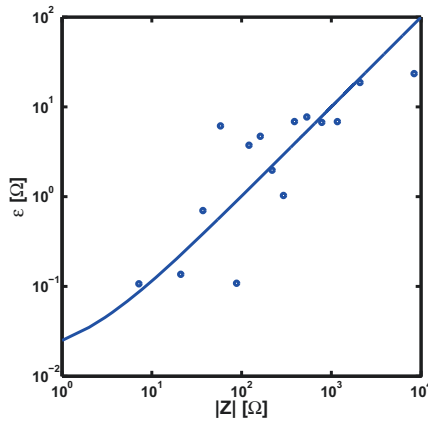
Figure 4.3: Binning of the symmetrical measurement configurations into 15 equally sized bins (dots) in logarithmic scale and the fitted error model (line).

4.4 Results and Discussion

4.4.1 *Inversion Results for mesh9*

Figure 4.4 shows inversion results for ρ_X and ρ_Z and the associated $\log_{10}(A)$ for three stages of the water infiltration experiment. These three stages were selected to evaluate in detail whether electrical resistivity and the associated anisotropy behave as expected in response to fast water flow in the macropore domain. In particular, we present results obtained before infiltration started (Stage I), during infiltration (Stage II), and after infiltration in the macropore stopped (Stage III).
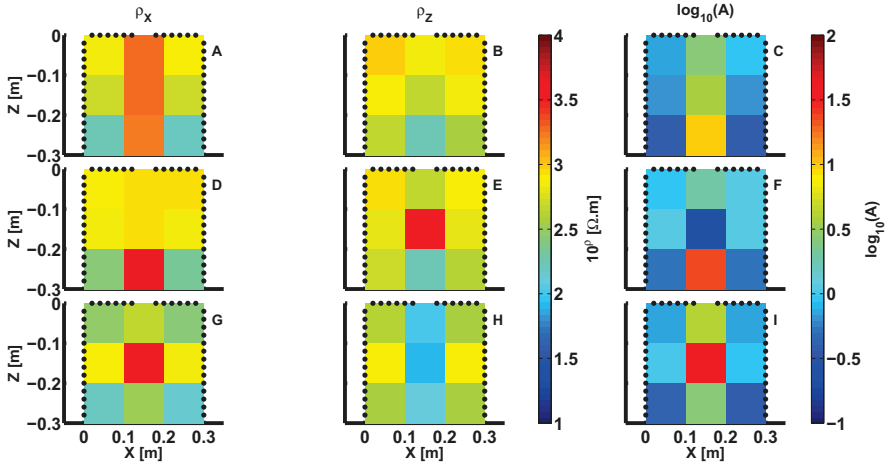
Figure 4.4: ERT inversion results for ρ_X (panel A, D, and G), ρ_Z (panel B, E, and H), and $\log_{10}(A)$ (panel C, F, and I) for Stage I (panel A, B, and C), Stage II (panel D, E, and F), and Stage III (panel G, H, and I) for mesh9.

The electrical resistivity distribution in Stage I should reflect the initial water content distribution. Since the initial water content of the macropore was lower than that of the matrix, we expect a higher electrical resistivity in the macropore domain. The presence of a resistive macropore pathway in a less resistive matrix in cells 2, 5, and 8 (see Figure 4.2(b) for cell numbering) presents a considerable flow barrier for electrical current in X-direction and thus should lead to a higher horizontal resistivity (ρ_X) as compared to the vertical resistivity (ρ_Z) and a $\log_{10}(A)$ that is larger than zero. This is indeed confirmed by the inversion results presented in the top row of Figure 4.4. The observed anisotropy ranged from $\log_{10}(A_2) = 0.41$, $\log_{10}(A_5) = 0.59$, to $\log_{10}(A_8) = 0.99$. The situation is different for cells without macropore. Here, ρ_X and ρ_Z are expected to be similar,

which results in a $\log_{10}(A)$ value close to zero. A general comparison of ρ_X and ρ_Z for cells 1, 3, 4, 6, 7, and 9 showed that it ranged from $10^{2.19}$ $\Omega.m$ to $10^{2.88}$ $\Omega.m$ for ρ_X and from $10^{2.58}$ $\Omega.m$ to $10^{2.98}$ $\Omega.m$ for ρ_Z. Electrical resistivity generally decreased with depth in the flow cell, which suggests that significant water distribution occurred between sample preparation and the start of the infiltration experiment. The $\log_{10}(A)$ factor was for these cells $\log_{10}(A_1)$ = -0.13, $\log_{10}(A_3)$ = -0.05, $\log_{10}(A_4)$ = -0.20, $\log_{10}(A_6)$ = -0.17, $\log_{10}(A_7)$ = -0.41, and $\log_{10}(A_9)$ = -0.39 with more negative anisotropy values near the bottom of the flow cell (cells 7 and 9) indicating lower electrical resistivity values in ρ_X than in ρ_Z. We attribute this to a layer with higher water content at the bottom of the tank that occurred due to downward water flow in the time period between sample preparation and the start of the infiltration experiment.

In general, it is also important to realize that the electrical resistivity and thus the anisotropy of cells 7, 8, and 9 are less well constrained because of the limited sensitivity (see Figure 4.5) of the electrical resistance measurements towards changes in the electrical resistivity of these cells due to lack of electrodes at the bottom of the tank. In Figure 4.5, it is evident that cell 5, 7, 8, and 9 are less constrained in both X- and Z-direction, although the lack of sensitivity is more evident in Z-direction. This higher sensitivity in X-direction for these cells as compared to the Z-direction is related to the cross-sample current injections (e.g. I0-I1, see Figure 4.1) that are much more influenced by ρ_X than ρ_Z.
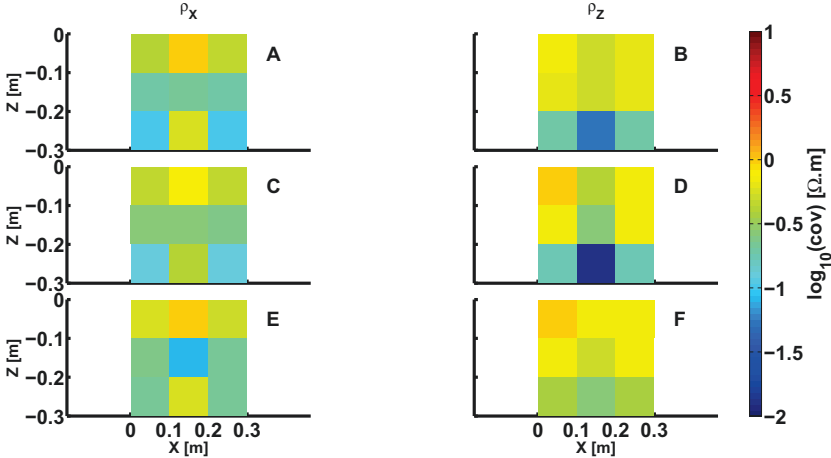

Figure 4.5: Cumulative sensitivity coverage for Stage I (panel A and B), Stage II (panel C and D), and Stage III (panel E and F) for ρ_X (left) and ρ_Z (right) for mesh9.

In Stage II, water was infiltrating in the macropore domain and this led to a decrease in ρ_X for cell 2 and 5 (i.e. $\rho_{X2} = 10^{2.95}$ $\Omega.m$ and $\rho_{X5} = 10^{2.94}$ $\Omega.m$) as

compared to Stage I (i.e. $\rho_{X2} = 10^{3.25}$ $\Omega.m$ and $\rho_{X5} = 10^{3.27}$ $\Omega.m$) for the same cells. This is related to the water-filled macropore that does not present a barrier for horizontal electric current flow anymore. The ρ_Z of cell 2 decreased more strongly than ρ_X, which resulted in an increase in the anisotropy relative to Stage I. The strong decrease in ρ_Z is attributed to a continuous electrically conductive pathway from the top to the bottom of cell 2 that consists of the water-filled macropore and a zone of wetted sand associated with flow from the macropore to the matrix region. The ρ_Z of cell 5 did not decrease, which indicates that the macropore was not wetted from top to bottom for this cell at this point in time. Overall, this resulted in a strong change in the anisotropy of cell 5 with a $\log_{10}(A)$ value as low as -0.60. The amount of infiltrated water was not sufficient to reach cell 8 so that no obvious changes relative to Stage I can be seen here. Moreover, no changes in the ρ_X and ρ_Z are expected between Stage I and Stage II for cells 1, 3, 4, 6, 7, and 9 because of the absence of flow, and this is confirmed by Figure 4.4D and 4.4E. The relative changes in electrical resistivity between Stage I and Stage II were below 18 % for ρ_X and ρ_z for cells 1 and 3 with the highest sensitivity, and increased with depth for reasons outlined above. The associated $\log_{10}(A)$ ranged from $\log_{10}(A_9) = $ -0.29 to $\log_{10}(A_6) = 0.05$ as shown in Figure 4.4F.

In Stage III, infiltration in the macropore has stopped and it is expected that water will move laterally from the macropore to the matrix domain (see simulation results in section 3.3.2 of Chapter 3) so that the electrical resistivity in the macropore domain will decrease. As in Stage I, the presence of the resistive macropore in a conductive matrix is expected to lead to a higher ρ_X as compared to ρ_Z. The results presented in Figure 4.4G and 4.4H for cells 2, 5, and 8 seem to be consistent with this simple conceptual model. The associated $\log_{10}(A)$ of Stage III are shown in Figure 4.4I and were $\log_{10}(A_2) = 0.63$, $\log_{10}(A_5) = 1.60$, and $\log_{10}(A_8) = 0.45$. Again, ρ_X and ρ_Z of cells 1, 3, 4, 6, 7, and 9 are relatively unaffected so that the $\log_{10}(A)$ values of these cells remain close to isotropic (i.e. ranged from $\log_{10}(A_9) = $ -0.40 to $\log_{10}(A_4) = 0.02$).

4.4.2 *Time-lapse ERT Results for mesh9*

Figure 4.6 shows time-lapse ERT results for ρ_X and ρ_Z for each cell in mesh9. Although 12000 data sets were available, we only inverted data until 120 seconds from the beginning of the experiment because no changes in measured transfer resistance were observed after this time. In addition, we only inverted every tenth frame to obtain a 1 second resolution. As expected because of the absence of water flow, ρ_X and ρ_Z of cells 1 to 9 are constant from time t = 1 s to t = 40 s

(i.e. see shaded area I in Figure 4.6), which indicates the stability of the resistance measurements obtained with the fast data acquisition system and the inversion procedure. As discussed previously, ρ_X and ρ_Z are similar for cells that do not contain the macropore, whereas ρ_X is higher than ρ_Z for cells with macropore. Infiltration started at t $= 41$ s and continued until t $= 67$ s (i.e. see shaded area II in Figure 4.6). The ρ_X and ρ_Z for cell 2 and 5 immediately decreased as soon as the infiltration process was started in the macropore domain and continued to decrease in at least one of the cells as long as water was being infiltrated, although a small increased in ρ_Z appeared between t $= 50$ s to t $= 59$ s for cell 2 and between t $= 40$ s to t $= 45$ s for cell 5. We attribute this unexpected increase to imaging issues related to appropriate error quantification, the estimation of the regularization parameter, and the impact of the considered mesh size (e.g. fine or coarse) with respect to the scale of the processes. Nevertheless, it is clear that ρ_X and ρ_Z reacted differently as was already expected from measurements presented in the previous Chapter 3 (Figure 3.6(c) in section 3.3.4). Although the expected behavior for Stage I and Stage III was also observed for cell 8 (Figure 4.6), no regular behavior of ρ_X nor ρ_Z was observed during Stage II for this cell because of the lack of the sensitivity in this part of the measurement cell. As expected, ρ_X and ρ_Z did not change strongly during infiltration for cells 4, 6, 7, and 9. Furthermore, a small drop in electrical resistivity for cell 1 and 3 occurred 16 s after the start of infiltration at t $= 57$ s, which indicates lateral flow from the macropore to the matrix domain in the top 10 cm of the measurement cell (see time1 to time6 in the simulated water content distribution in Figure 3.5).

After infiltration stopped from t $= 68$ s onwards (i.e. see shaded area III in Figure 4.6), an increase in ρ_X towards the initial value is observed for cells 2 and 5. However, we notice that it took a few seconds to stabilize infiltration between the end of Stage II and the beginning of Stage III which can be seen in ρ_X for cell 5 in Figure 4.6. The ρ_Z did not increase for these two cells. We attribute this to the saturation dynamics in the macropore. After infiltration stopped, water redistributed from the macropore to the matrix and the decreased macropore saturation caused an increase in ρ_X. The ρ_Z did not significantly increase because the macropore only occupies a moderate part of the cell.

Figure 4.7 shows the temporal development of the electrical anisotropy of all cells in mesh9. Overall, it is evident that the anisotropy in electrical resistivity is a clear indicator of unresolved preferential flow processes. All cells with the unresolved macropore showed strong temporal dynamics in electrical anisotropy (i.e. cells 2, 5, and 8), whereas cells without macropore did not show fast changes in electrical anisotropy. As soon as the infiltration process started, the macropore domain is

filled with water (activated) and both ρ_X and ρ_Z decreased as long as water is present in the macropore. After infiltration stopped, the anisotropy returned to values larger than prior to infiltration because of the presence of the resistive (deactivated) macropore (high ρ_X) in a matrix that has now been wetted by exchange with the macropore and thus has a lower ρ_Z than before infiltration.
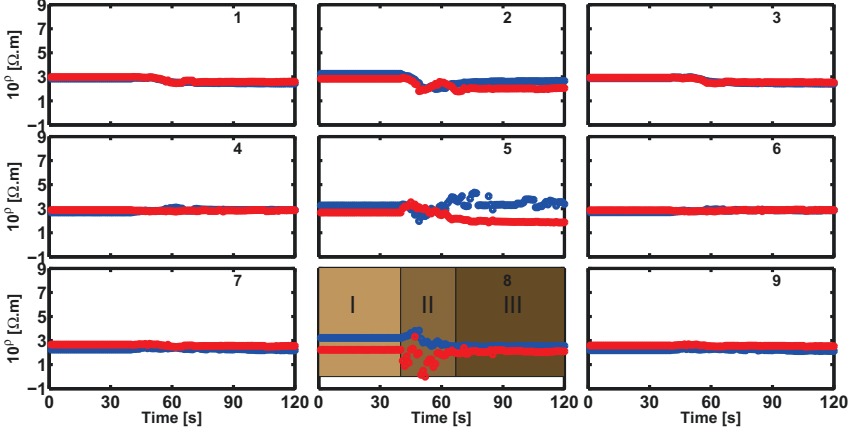
Figure 4.6: Time-lapse ERT results for ρ_X (blue) and ρ_Z (red) for cell 1 to 9 of mesh9.

Figure 4.7: Time-lapse ERT results for the anisotropy of cells with macropore (2, 5, and 8) and cells without macropore (1, 3, 4, 6, 7, and 9) for mesh9.

4.4.3 *Time-lapse ERT Results for mesh25*

To investigate to what extent the inversion results are affected by the size of the inversion cells, the analysis was repeated for a second inversion grid with 25

cells (see Figure 4.2(c) for corresponding cell numbering). Figure 4.8 presents the temporal changes in electrical resistivity for this second mesh. We present results in a similar manner as for the first coarse grid by considering cells that are part of the matrix domain only (1, 5, 11, 15, 21, and 25), and cells that are combinations of the matrix and macropore domain (3, 13, and 23). Again, ρ_X and ρ_Z of all selected cells in mesh25 is constant from time t = 1 s to t = 40 s. For Stage I, ρ_X and ρ_Z for cells without macropore show a good match between the results for mesh25 and mesh9 as expressed by the relative changes between corresponding inversion cells (see Table 4.2). These relative changes were calculated from the mean value over all times in Stage I and were below 3 % for ρ_X and below 13 % for ρ_Z for top cells with the highest sensitivity (Figure 4.5). The relative differences increased with decreasing sensitivity, especially for ρ_Z. For cells with macropore, the best correspondence between the inversion results of mesh25 and mesh9 is observed for cells near the top of the measurement cell (e.g. cell 3 in Figure 4.8 with its corresponding cell 2 in Figure 4.6). For this cell 3, both ρ_X and ρ_Z decreased strongly as soon as infiltration started, although an increase in ρ_Z was obtained between t = 40 s and t = 43 s, which we attribute to imaging issues as detailed above. Furthermore, ρ_Z for cell 13 and 23 is higher than ρ_X, which is not the case for the corresponding cells in mesh9. Again, we attribute this to the limited sensitivity near the bottom of the measurement cell, which leads to less well-constrained inversion results that are more sensitive to measurement errors and regularization artifacts.

Table 4.2: Relative changes for cells without macropore in mesh25 with respect to their corresponding cells in mesh9 for ρ_X, ρ_Z, and A for Stage I.

Relative changes (%)	mesh25 to mesh9					
	1	5	11	15	21	25
ρ_X	2.6	2.3	12.4	12.2	59.5	13
ρ_Z	13	13	54.4	42	68.8	160.4
A	11.9	17.6	27.2	38.2	5.5	56.6

Figure 4.9 presents the temporal changes in $\log_{10}(A)$ for the same selected cells in mesh25. Table 4.2 also provides the relative changes in anisotropy for cells without macropore in mesh25 and their corresponding cells in mesh9. In general, the results for the finer grid confirm that preferential flow in the macropore leads to strong temporal dynamics in the anisotropy of the electrical resistivity, which decreases with depth within the flow cell. It is evident that cell 3 shows the strongest response to water infiltration. Before infiltration, a constant positive anisotropy was obtained ($\log_{10}(A_3) = 1.64$) followed by a strong decrease in anisotropy when infiltration started at time t = 41 s. As soon as water infiltration

stopped, anisotropy increased because water redistributed to matrix domain. In addition, the cells without macropore hardly showed temporal variability in the electrical anisotropy independent of the chosen inversion grid.
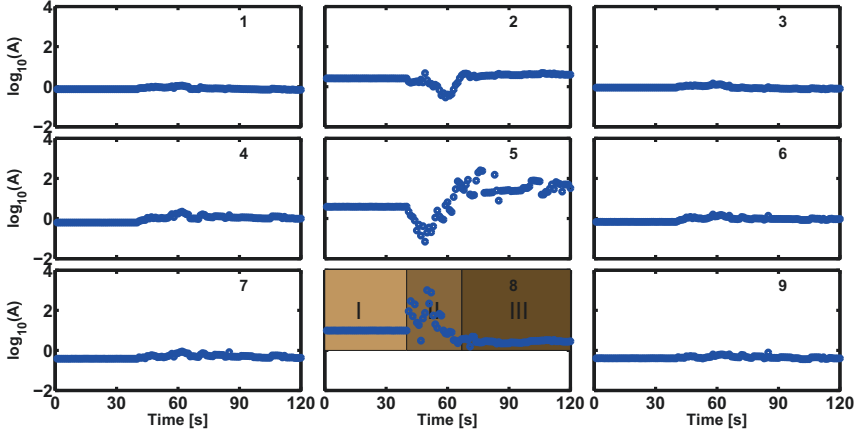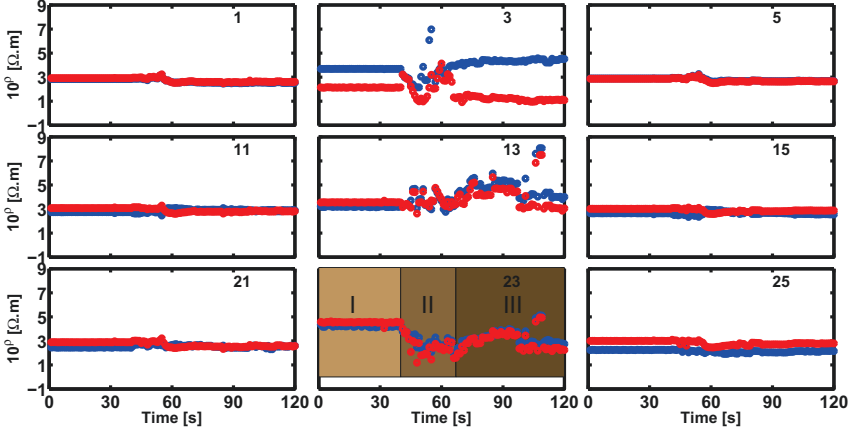

Figure 4.8: Time-lapse ERT results for ρ_X (blue) and ρ_Z (red) for the selected cells of mesh25.
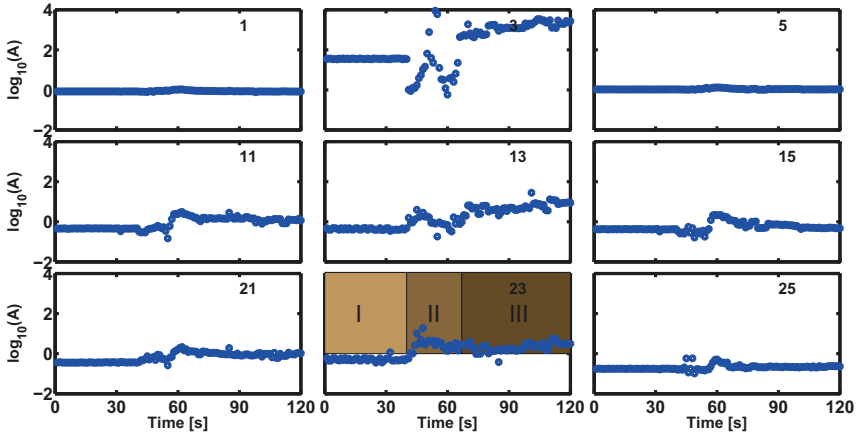
Figure 4.9: Time-lapse ERT results for the anisotropy for selected cells with macropore (3, 13, and 23) and without macropore (1, 5, 11, 15, 21, and 25) for mesh25.

In general, the dynamical changes in anisotropy of electrical resistivity associated with water infiltration into the macropore were larger for mesh9 than for mesh25. Furthermore, higher anisotropy values for mesh9 were obtained with depth in the flow cell. The key to interpreting this result is the size of the inversion cells with respect to the scale of the processes. When inversion cells are used that are small compared to the process scale, both ρ_X and ρ_Z decrease strongly due

to the presence of infiltrating water because the conductive vertical pathway is surrounded by narrower resistive area that belongs to the matrix domain. With increasing size of the inversion cells, the surrounded resistive area that belongs to the matrix domain becomes larger and therefore ρ_X decreases more than ρ_Z when the macropore domain becomes wet. In the case of mesh9, the macropore occupied about 20 % of the inversion cell, whereas this value was 33 % for mesh25. When considering that there also is significant exchange of water between macropore and matrix, it is not unreasonable to assume that mesh25 almost resolves the relevant processes and thus resulted in lower electrical anisotropy values. In field applications, it will not be straightforward to determine the optimum size of the inversion cells, because of the limited and likely spatially variable scale of the macropore flow processes. Clearly, the use of too small inversion cells will cause the disappearance of the macroscopic anisotropy. Based on our limited testing, it seems adequate when the scale of the processes occupies ~ 20 % of the inversion cells.

4.5 Conclusions

In the previous Chapter 3, we showed that a direct measurement of electrical resistivity in horizontal and vertical direction leads to electrical anisotropy in preferential flow processes. However, the observed anisotropy was difficult to interpret in the context of the simple conceptual model that was presented by Moysey and Liu (2012) because of the chosen experimental setup and electrode configurations. To overcome this limitation, we extended the previous work by performing time-lapse ERT measurements during an infiltration experiment on a Hele-Shaw tank with an artificial macropore. The ERT data sets were inverted to obtain images of the anisotropic electrical resistivity using coarse inversion grids so that flow processes remain unresolved and appear in the electrical anisotropy. As in the previous experiments, we found that ρ_X and ρ_Z reacted differently to the water infiltration and that preferential flow processes lead to strong temporal dynamics in the electrical anisotropy. With the imaging framework used in this study, the observed anisotropy was more straightforward to interpret and largely controlled by the electrical resistivity of the macropore. Prior to infiltration, the empty macropore was a barrier for electrical current flow leading to a much higher ρ_X as compared to ρ_Z in cells with a macropore. When infiltration started, ρ_X decreased more strongly than ρ_Z leading to temporal changes in the electrical anisotropy. After infiltration stopped and water redistributed to the matrix domain, the macropore domain presented a barrier to electrical current flow again, thus increasing the electrical

resistivity and the associated anisotropy again. The imaging results showed that strong temporal changes of macro-anisotropy occurred in cells with macropore although the volume of the macropore was small as compared to the volume of the tank and the inversion cells. In contrast, no changes in the anisotropy response to water infiltration were observed in cells without macropore.

The results also showed that the size of the inversion cells relative to the process scale (i.e. macropore dimensions) is an important issue when using electrical anisotropy imaging to study macropore preferential flow processes. We found stronger temporal changes in electrical anisotropy when the macropore occupied 20 % of the inversion cell as compared to the case where the macropore occupied 33 % of the inversion cell. Overall, we conclude temporal dynamics in the electrical anisotropy may be a good indication of preferential flow processes in the subsurface. In a next step, it should be investigated whether anisotropic inversion of ERT data can be used to identify and study preferential flow in field applications.

Chapter 5

CONCLUSIONS AND OUTLOOK

In this Chapter (5), we will present the overall conclusions and outlook of this thesis. First, the main findings of each Chapter will be summarized and the main conclusions will be highlighted. Furthermore, we will present recommendations to further improve the results and discuss limitations and drawbacks that were found in each Chapter. In addition, we provide a short outlook where the next important steps for this research direction will be provided.

5.1   Conclusions

Geophysical methods are increasingly used to study flow and transport processes in heterogeneous porous media. In this thesis, it was investigated whether anisotropy in electrical resistivity can provide information on heterogeneous soil and sediment structures and preferential flow processes. This overall objective of this thesis involved sub-goals that are summarized as follows: (1) to experimentally validate an existing synthetic modelling study that showed how measurements of the anisotropy of the complex resistivity can be used to obtain structural information for heterogeneous bimodal facies distributions, (2) to examine whether measurements of electrical resistivity anisotropy provide information on preferential flow processes in a soil column with artificial macropore, and (3) to monitor the temporal dynamics of macroscopic anisotropy in electrical resistivity associated with water infiltration in artificial macropore using tomography techniques.

In Chapter 2, a new measurement strategy was developed to obtain the relationship between electrical anisotropy of complex resistivity and Cole-Cole parameters,

volume fraction, and correlation length ratio of bimodal heterogeneous soil distributions. This new strategy was successfully tested using a synthetic modelling study and spectral electrical anisotropy measurements on simple two-layer distributions for which the effective complex electrical resistivity could be calculated using analytical solutions. In the synthetic modelling study, a satisfying agreement was found between the prescribed and fitted Cole-Cole parameters. In addition, both the volume fraction and the correlation length ratio also showed an excellent agreement between the prescribed and fitted values, although minor deviations in volume fraction were observed for small correlation length ratios. The test measurements on a two-layer sediment structure provided resistivity magnitude and phase angle spectra that matched well with modelled spectra obtained using analytical solutions. In a final step, the spectral electrical anisotropy of the resistivity was determined from measurements on a heterogeneous bimodal distribution, and the Cole-Cole parameters, volume fraction, and the correlation length ratio was inversely estimated from the spectral electrical anisotropy. The fitted Cole-Cole parameters were reasonably close to the Cole-Cole parameters that were independently measured using SIP. The estimated volume fraction showed an acceptable match, and remaining deviations were attributed to variations in sediment thickness. The fitted correlation length ratio (7.89) for this heterogeneous distribution also matched well with the modelled correlation length ratio for this distribution (7.39). It was concluded that a direct measurement of horizontal and vertical effective complex electrical resistivity resulted in sufficient contrast so that the spectral electrical anisotropy provided sufficient information to obtain relevant information on the geometrical arrangement of subsurface properties (i.e. the correlation length ratio). The results in this Chapter (2) illustrate that electrical resistivity anisotropy may provide relevant information to better characterize subsurface heterogeneity in soil and sediment.

In Chapter 3, we investigated the relationship between electrical resistivity anisotropy and macropore preferential flow. A 3D synthetic modelling study of water infiltration into an artificial macropore within a soil column showed strong temporal changes in resistivity anisotropy because electrical resistivity in horizontal and vertical direction reacted differently to the water infiltration process. However, modelled changes in anisotropy did not match available conceptual models where the presence of a conductive macropore in a resistive matrix leads to a lower vertical resistivity as compared to horizontal resistivity. This was attributed to the relatively small resistivity contrast between the matrix and the macropore and the effect of the sensitivity distribution of the electrode configurations. A model sensitivity analysis was performed to investigate how the simulated dynamics of

the electrical anisotropy were affected by the hydraulic properties of the macropore and matrix domain. It was found that the electrical anisotropy was more sensitive to the hydraulic properties of the matrix domain, and the air-entry value α and the saturated water content θ_s in particular. Actual electrical resistivity measurements on an identical soil column resulted in similar dynamical changes in the electrical anisotropy as in the synthetic modelling study. A small positive anisotropy at the beginning of the experiment was observed, which was followed by a strong decrease as soon as water was infiltrated in the macropore domain. After infiltration, water redistributed to the matrix domain and the anisotropy increased towards its initial values. It was concluded that electrical resistivity anisotropy is promising to study water infiltration and solute transport processes in the vadose zone in general and in macropores in particular.

In Chapter 4, the temporal dynamics of the electrical resistivity anisotropy associated with water infiltration into macropores were imaged using ERT. Two-dimensional anisotropic inversion was used to produce resistivity images using inversion cells that were coarser than the size of the macropore. The imaging results confirmed that the electrical resistivity anisotropy can be used to identify and localize macropore preferential flow. During water infiltration, strong anisotropy changes were seen in inversion cells with macropore, whereas the cells without macropore showed almost no anisotropic behavior. The results clearly showed that unresolved macropore preferential flow processes appear in the electrical anisotropy. It was concluded that electrical anisotropy should be considered in inversion techniques especially in field applications where heterogeneity and macro-anisotropy are obvious because of soil manipulation by human activity, plants, or soil fauna.

5.2   Outlook

The experimental validation study performed in Chapter 2 would benefit from additional investigations using more complex heterogeneous distributions. In order to ensure better contact between different materials, the use of an improved packing methodology using frozen soil cubes should be explored. The use of a wide range of materials with variable contrast in magnitude and phase angle spectra of complex resistivity would provide deeper insights in the possibilities and limitations of the structural characterization of aquifers using the spectral electrical anisotropy. In addition, such an extended validation would offer the possibility to evaluate the need for alternative mixing models to describe the effective spec-

tral electrical resistivity and alternative relaxation models to describe the spectral electrical resistivity of the individual materials. There is also scope to further improve the synthetic modelling study by considering larger simulation domains because the simulation results for large correlation length ratios presented here were influenced by the relatively small size of the simulation domain. An important next step is to move this type of work to a field application. Here, the use of undisturbed soil in a controlled laboratory set-up is an obvious first step. If the experiments are done in the laboratory, factors that influence the spectral electrical resistivity like temperature and water content can be better controlled. The more important next step is to perform field experiments where heterogeneity is most likely appears in horizontal and vertical direction. In the field, much more complicated heterogeneous distributions are present and a wide range of materials are available.

In Chapter 3 and 4, it was shown that electrical anisotropy associated with macropore flow processes was better investigated using imaging techniques than using direct measurements of electrical resistivity in two perpendicular directions. Therefore, research to further improve electrical anisotropy imaging is essential for this type of research. In particular, attention should be focused on data error quantification analysis, appropriate selection of regularization parameters, and the impact of mesh size on the anisotropic inversion results. In future laboratory experiments, the comparison of measured and modelled electrical anisotropy associated with macropore flow processes can be improved by considering hydraulic properties and petrophysical parameters that are determined directly at soil sample columns. The next important step is to move this type of research to field applications. In a first step, experiments on laboratory columns with disturbed soil could be performed. This would allow extending the analysis and interpretation methods outlined in Chapter 4 from 2D to 3D. Such laboratory experiments would also be useful to investigate the effect of macropore porosity, macropore size, and macropore density on the imaged electrical anisotropy. In a next step, undisturbed soil columns with macropores should be analyzed in controlled laboratory conditions. Such investigations would require the development of 3D anisotropic inversion codes. Evidently, anisotropic electrical imaging poses additional constraints on the speed and geometrical arrangement of the electrical resistivity measurements. The high-speed ERT data acquisition system that was used in the laboratory in this study is available to be used in field experiments. Appropriate field electrode arrangements that allow to image electrical anisotropy ideally include both surface electrodes and electrodes buried in the soil in order to obtain improved on the vertical component of the electrical resistivity tensor. This

could be achieved using electrode strings (e.g. Greve et al., 2012b) or electrode sticks (e.g. Oberdörster et al., 2010).

References

Abou Najm, M. R., J. D. Jabro, W. M. Iversen, R. H. Mohtar, and R. G. Evans (2010), New method for the characterization of three-dimensional preferential flow paths in the field, Water Resources Research, 46(2), W02503, doi:10.1029/2009WR008594.

Ahmed, S., and G. de Marsily (1987), Comparison of geostatistical methods for estimating transmissivity using data on transmissivity and specific capacity, Water Resources Research, 23(9), 1717–1737, doi:10.1029/WR023i009p01717.

Alexander, M., S. J. Berg, and W. A. Illman (2011), Field study of hydrogeologic characterization methods in a heterogeneous aquifer, Ground Water, 49(3), 365–382, doi:10.1111/j.1745-6584.2010.00729.x.

Allaire, S. E., S. C. Gupta, J. Nieber, and J. F. Moncrief (2002a), Role of macropore continuity and tortuosity on solute transport in soils: 1. Effects of initial and boundary conditions, Journal of Contaminant Hydrology, 58(3), 299–321, doi:10.1016/S0169-7722(02)00035-9.

Allaire, S. E., S. C. Gupta, J. Nieber, and J. F. Moncrief (2002b), Role of macropore continuity and tortuosity on solute transport in soils: 2. Interactions with model assumptions for macropore description, Journal of Contaminant Hydrology, 58(3), 283–298, doi:10.1016/S0169-7722(02)00034-7.

Allaire, S. E., S. Roulier, and A. J. Cessna (2009), Quantifying preferential flow in soils: A review of different techniques, Journal of Hydrology, 378(1), 179–204, doi:10.1016/j.jhydrol.2009.08.013.

Archie, G. E. (1942), The electrical resistivity log as an aid in determining some reservoir characteristics, Transactions of the AIME, 146(1), 54–62, doi:10.2118/942054-G.

Bayer, P., P. Huggenberger, P. Renard, and A. Comunian (2011), Three-dimensional high resolution fluvio-glacial aquifer analog: Part 1: Field study, Journal of Hydrology, 405(1), 1–9, doi:10.1016/j.jhydrol.2011.03.038.

Bechtold, M., S. Haber-Pohlmeier, J. Vanderborght, A. Pohlmeier, T. P. A. Ferré, and H. Vereecken (2011), Near-surface solute redistribution during evaporation, Geophysical Research Letters, 38(17), L17404, doi:10.1029/2011GL048147.

Bechtold, M., J. A. Huisman, L. Weihermüller, and H. Vereecken (2010), Accurate determination of the bulk electrical conductivity with the TDR100 cable tester, Soil Science Society of America Journal, 74(2), 495–501, doi:10.2136/sssaj2009.0247.

Bechtold, M., J. Vanderborght, L. Weihermüller, M. Herbst, T. Günther, O. Ippisch, R. Kasteel, and H. Vereecken (2012), Upward transport in a three-dimensional heterogeneous laboratory soil under evaporation conditions, Vadose Zone Journal, 11(2), doi:10.2136/vzj2011.0066.

Beckwith, C. W., A. J. Baird, and A. L. Heathwaite (2003a), Anisotropy and depth-related heterogeneity of hydraulic conductivity in a bog peat. I: laboratory measurements, Hydrological Processes, 17(1), 89–101, doi:10.1002/hyp.1116.

Beckwith, C. W., A. J. Baird, and A. L. Heathwaite (2003b), Anisotropy and depth-related heterogeneity of hydraulic conductivity in a bog peat. II: modelling the effects on groundwater flow, Hydrological Processes, 17(1), 103–113, doi:10.1002/hyp.1117.

Beven, K., and P. Germann (1982), Macropores and water flow in soils, Water Resources Research, 18(5), 1311–1325, doi:10.1029/WR018i005p01311.

Bierkens, M. F. P., and J. W. J. van der Gaast (1998), Upscaling hydraulic conductivity: theory and examples from geohydrological studies, in Soil and Water Quality at Different Scales, *Developments in Plant and Soil Sciences*, vol. 80, edited by P. A. Finke, J. Bouma, and M. R. Hoosbeek, pp. 193–207, Springer Netherlands, doi:10.1007/978-94-017-3021-1_19.

Binley, A., G. Cassiani, R. Middleton, and P. Winship (2002), Vadose zone flow model parameterisation using cross-borehole radar and resistivity imaging, Journal of Hydrology, 267(3), 147–159, doi:10.1016/S0022-1694(02)00146-4.

Binley, A., S. Henry-Poulter, and B. Shaw (1996a), Examination of solute transport in an undisturbed soil column using electrical resistance tomography, Water Resources Research, 32(4), 763–769, doi:10.1029/95WR02995.

Binley, A., and A. Kemna (2005), DC resistivity and induced polarization methods, in Hydrogeophysics, *Water Science and Technology Library*, vol. 50, edited by Y. Rubin and S. S. Hubbard, pp. 129–156, Springer Netherlands, doi:10.1007/1-4020-3102-5_5.

Binley, A., B. Shaw, and S. Henry-Poulter (1996b), Flow pathways in porous media: electrical resistance tomography and dye staining image verification, Measurement Science and Technology, 7(3), 384–390, doi:10.1088/0957-0233/7/3/020.

Breede, K. (2013), Characterization of effective hydraulic properties of unsaturated porous media using spectral induced polarization (SIP), *Schriften des Forschungszentrums Jülich. Reihe Energie und Umwelt / Energy and Environment*, vol. 175, Forschungszentrum Jülich GmbH, Zentralbibliothek.

Breede, K., A. Kemna, O. Esser, E. Zimmermann, H. Vereecken, and J. A. Huisman (2011), Joint measurement setup for determining spectral induced polarization and soil hydraulic properties, Vadose Zone Journal, 10(2), 716–726, doi:10.2136/vzj2010.0110.

Breede, K., A. Kemna, O. Esser, E. Zimmermann, H. Vereecken, and J. A. Huisman (2012), Spectral induced polarization measurements on variably saturated sand-clay mixtures, Near Surface Geophysics, 10(6), 479–489, doi:10.3997/1873-0604.2012048.

Buttle, J. M., and D. G. Leigh (1997), The influence of artificial macropores on water and solute transport in laboratory soil columns, Journal of Hydrology, 191(1), 290–314, doi:10.1016/S0022-1694(96)03079-X.

Cacas, M. C., E. Ledoux, G. de Marsily, A. Barbreau, P. Calmels, B. Gaillard, and R. Margritta (1990a), Modeling fracture flow with a stochastic discrete fracture network: Calibration and validation: 2. The transport model, Water Resources Research, 26(3), 491–500, doi:10.1029/WR026i003p00491.

Cacas, M. C., E. Ledoux, G. de Marsily, B. Tillie, A. Barbreau, E. Durand, B. Feuga, and P. Peaudecerf (1990b), Modeling fracture flow with a stochastic discrete fracture network: Calibration and validation: 1. The flow model, Water Resources Research, 26(3), 479–489, doi:10.1029/WR026i003p00479.

Carrera, J. (1993), An overview of uncertainties in modelling groundwater solute transport, Journal of Contaminant Hydrology, 13(1), 23–48, doi:10.1016/0169-7722(93)90049-X.

Castiglione, P., B. P. Mohanty, P. J. Shouse, J. Simunek, M. T. van Genuchten, and A. Santini (2003), Lateral water diffusion in an artificial macroporous system: Modeling and experimental evidence, Vadose Zone Journal, 2(2), 212–221, doi:10.2113/2.2.212.

Cole, K. S., and R. H. Cole (1941), Dispersion and absorption in dielectrics I. Alternating current characteristics, Journal of Chemical Physics, 9, 341–351, doi:10.1063/1.1750906.

Comunian, A., P. Renard, J. Straubhaar, and P. Bayer (2011), Three-dimensional high resolution fluvio-glacial aquifer analog - Part 2: Geostatistical modeling, Journal of Hydrology, 405(1), 10–23, doi:10.1016/j.jhydrol.2011.03.037.

Cook, A. E., B. I. Anderson, A. Malinverno, S. Mrozewski, and D. S. Goldberg (2010), Electrical anisotropy due to gas hydrate-filled fractures, Geophysics, 75(6), F173–F185, doi:10.1190/1.3506530.

Coscia, I., N. Linde, S. Greenhalgh, T. Günther, and A. Green (2012), A filtering method to correct time-lapse 3D ERT data and improve imaging of natural aquifer dynamics, Journal of Applied Geophysics, 80, 12–24, doi:10.1016/j.jappgeo.2011.12.015.

Dagan, G. (1982), Stochastic modeling of groundwater flow by unconditional and conditional probabilities: 1. Conditional simulation and the direct problem, Water Resources Research, 18(4), 813–833, doi:10.1029/WR018i004p00813.

Dagan, G. (1985), Stochastic modeling of groundwater flow by unconditional and conditional probabilities: The inverse problem, Water Resources Research, 21(1), 65–72, doi:10.1029/WR021i001p00065.

Dai, Z., R. W. J. Ritzi, and D. F. Dominic (2005), Improving permeability semi-variograms with transition probability models of hierarchical sedimentary architecture derived from outcrop analog studies, Water resources research, 41(7), W07032, doi:10.1029/2004WR003515.

Daily, W., A. Ramirez, D. LaBrecque, and J. Nitao (1992), Electrical resistivity tomography of vadose water movement, Water Resources Research, 28(5), 1429–1442, doi:10.1029/91WR03087.

de Marsily, G., F. Delay, J. Gonçalvès, P. Renard, V. Teles, and S. Violette (2005), Dealing with spatial heterogeneity, Hydrogeology Journal, 13(1), 161–183, doi:10.1007/s10040-004-0432-3.

Deiana, R., G. Cassiani, A. Villa, A. Bagliani, and V. Bruno (2008), Calibration of a vadose zone model using water injection monitored by GPR and electrical resistance tomography, Vadose Zone Journal, 7(1), 215–226, doi:10.2136/vzj2006.0137.

Deutsch, C. V., and A. G. Journel (1998), Geostatistical software library and user's guide, Oxford University Press, New York, second edn.

Doetsch, J., N. Linde, M. Pessognelli, A. G. Green, and T. Günther (2012), Constraining 3-D electrical resistance tomography with GPR reflection data for improved aquifer characterization, Journal of Applied Geophysics, 78, 68–76, doi:10.1016/j.jappgeo.2011.04.008.

Duan, Q. Y., V. K. Gupta, and S. Sorooshian (1993), Shuffled complex evolution approach for effective and efficient global minimization, Journal of Optimization Theory and Applications, 76(3), 501–521, doi:10.1007/BF00939380.

Edwards, R. N., D. C. Nobes, and E. Gómez-Treviño (1984), Offshore electrical exploration of sedimentary basins: The effects of anisotropy in horizontally isotropic, layered media, Geophysics, 49(5), 566–576, doi:10.1190/1.1441691.

Ela, S. D., S. C. Gupta, and W. J. Rawls (1992), Macropore and surface seal interactions affecting water infiltration into soil, Soil Science Society of America Journal, 56(3), 714–721, doi:10.2136/sssaj1992.03615995005600030007x.

Feyen, J., D. Jacques, A. Timmerman, and J. Vanderborght (1998), Modelling water flow and solute transport in heterogeneous soils: A review of recent approaches, Journal of Agricultural Engineering Research, 70(3), 231–256, doi:10.1006/jaer.1998.0272.

FitzPatrick, E. A., L. A. Mackie, and C. E. Mullins (1985), The use of plaster of Paris in the study of soil structure, Soil Use and Management, 1(2), 70–72, doi:10.1111/j.1475-2743.1985.tb00660.x.

Flühler, H., W. Durner, and M. Flury (1996), Lateral solute mixing processes - A key for understanding field-scale transport of water and solutes, Geoderma, 70(2), 165–183, doi:10.1016/0016-7061(95)00079-8.

Flury, M., H. Flühler, W. A. Jury, and J. Leuenberger (1994), Susceptibility of soils to preferential flow of water: A field study, Water Resources Research, 30(7), 1945–1954, doi:10.1029/94WR00871.

Fogg, G. E., C. D. Noyes, and S. F. Carle (1998), Geologically based model of heterogeneous hydraulic conductivity in an alluvial setting, Hydrogeology Journal, 6(1), 131–143, doi:10.1007/s100400050139.

Garner, M. R. (1953), The preparation of latex casts of soil cavities for the study of tunneling activities of animals, Science, 118(3066), 380–381, doi:10.1126/science.118.3066.380.

Garré, S., I. Coteur, C. Wongleecharoen, T. Kongkaew, J. Diels, and J. Vanderborght (2013), Noninvasive monitoring of soil water dynamics in mixed cropping systems: A case study in Ratchaburi province, Thailand, Vadose Zone Journal, 12(2), doi:10.2136/vzj2012.0129.

Garré, S., M. Javaux, J. Vanderborght, L. Pagès, and H. Vereecken (2011), Three-dimensional electrical resistivity tomography to monitor root zone water dynamics, Vadose Zone Journal, 10(1), 412–424, doi:10.2136/vzj2010.0079.

Garré, S., J. Koestel, T. Günther, M. Javaux, J. Vanderborght, and H. Vereecken (2010), Comparison of heterogeneous transport processes observed with electrical resistivity tomography in two soils, Vadose Zone Journal, 9(2), 336–349, doi:10.2136/vzj2009.0086.

Gelhar, L. W. (1986), Stochastic subsurface hydrology from theory to applications, Water Resources Research, 22(9), 135S–145S, doi:10.1029/WR022i09Sp0135S.

Gerke, H. H. (2006), Preferential flow descriptions for structured soils, Journal of Plant Nutrition and Soil Science, 169(3), 382–400, doi:10.1002/jpln.200521955.

Ghodrati, M., and W. A. Jury (1992), A field study of the effects of soil structure and irrigation method on preferential flow of pesticides in unsaturated soil, Journal of Contaminant Hydrology, 11(1-2), 101–125, doi:10.1016/0169-7722(92)90036-E.

Glass, R. J., M. J. Nicholl, A. L. Ramirez, and W. D. Daily (2002), Liquid phase structure within an unsaturated fracture network beneath a surface infiltration event: Field experiment, Water Resources Research, 38(10), 17–1–17–16, doi:10.1029/2000WR000167.

Goovaerts, P. (2001), Geostatistical modelling of uncertainty in soil science, Geoderma, 103(1), 3–26, doi:10.1016/S0016-7061(01)00067-2.

Greco, R. (2002), Preferential flow in macroporous swelling soil with internal catchment: model development and applications, Journal of Hydrology, 269(3-4), 150–168, doi:10.1016/S0022-1694(02)00215-9.

Greve, A., M. S. Andersen, and R. I. Acworth (2010a), Investigations of soil cracking and preferential flow in a weighing lysimeter filled with cracking clay soil, Journal of Hydrology, 393(1-2), 105–113, doi:10.1016/j.jhydrol.2010.03.007.

Greve, A. K., R. I. Acworth, and B. F. J. Kelly (2010b), Detection of subsurface soil cracks by vertical anisotropy profiles of apparent electrical resistivity, Geophysics, 75(4), WA85–WA93, doi:10.1190/1.3474590.

Greve, A. K., R. I. Acworth, and B. F. J. Kelly (2012a), 3D cross-hole resistivity tomography to monitor water percolation during irrigation on cracking soil, Soil Research, 49(8), 661–669, doi:10.1071/SR11270.

Greve, A. K., M. S. Andersen, and R. I. Acworth (2012b), Monitoring the transition from preferential to matrix flow in cracking clay soil through changes in electrical anisotropy, Geoderma, 179–180, 46–52, doi:10.1016/j.geoderma.2012.02.003.

Günther, T., C. Rücker, and K. Spitzer (2006), Three-dimensional modelling and inversion of dc resistivity data incorporating topography II. Inversion, Geophysical Journal International, 166(2), 506–517, doi:10.1111/j.1365-246X.2006.03011.x.

Haber-Pohlmeier, S., M. Bechtold, S. Stapf, and A. Pohlmeier (2010), Water flow monitored by tracer transport in natural porous media using magnetic resonance imaging, Vadose Zone Journal, 9(4), 835–845, doi:10.2136/vzj2009.0177.

Herwanger, J. V., C. C. Pain, A. Binley, C. R. E. de Oliveira, and M. H. Worthington (2004), Anisotropic resistivity tomography, Geophysical Journal International, 158(2), 409–425, doi:10.1111/j.1365-246X.2004.02314.x.

Hill, D. G. (1972), A laboratory investigation of electrical anisotropy in Precambrian rocks, Geophysics, 37(6), 1022–1038, doi:10.1190/1.1440311.

Huisman, J. A., C. P. Lin, L. Weihermüller, and H. Vereecken (2008), Accuracy of bulk electrical conductivity measurements with time domain reflectometry, Vadose Zone Journal, 7(2), 426–433, doi:10.2136/vzj2007.0139.

Illman, W. A., S. J. Berg, and M. Alexander (2012), Cost comparisons of aquifer heterogeneity characterization methods, Ground Water Monitoring & Remediation, 32(2), 57–65, doi:10.1111/j.1745-6592.2011.01376.x.

Jacod, J., and P. Joathon (1971), Use of random-genetic models in the study of sedimentary processes, Journal of the International Association for Mathematical Geology, 3(3), 265–279, doi:10.1007/BF02045795.

Jarvis, N. J. (2007), A review of non-equilibrium water flow and solute transport in soil macropores: principles, controlling factors and consequences for water quality, European Journal of Soil Science, 58(3), 523–546, doi:10.1111/j.1365-2389.2007.00915.x.

Johnson, N. M. (1995), Characterization of alluvial hydrostratigraphy with indicator semivariograms, Water Resources Research, 31(12), 3217–3227, doi:10.1029/95WR02571.

Jones, G., P. Sentenac, and M. Zielinski (2014), Desiccation cracking detection using 2-D and 3-D electrical resistivity tomography: Validation on a flood embankment, Journal of Applied Geophysics, 106, 196–211, doi:10.1016/j.jappgeo.2014.04.018.

Jones, G., M. Zielinski, and P. Sentenac (2012), Mapping desiccation fissures using 3-D electrical resistivity tomography, Journal of Applied Geophysics, 84, 39–51, doi:10.1016/j.jappgeo.2012.06.002.

Kaestner, A., E. Lehmann, and M. Stampanoni (2008), Imaging and image processing in porous media research, Advances in Water Resources, 31(9), 1174–1187, doi:10.1016/j.advwatres.2008.01.022.

Kemna, A. (2000), Tomographic inversion of complex resistivity – Theory and application, *Berichte des Institutes für Geophysik der Ruhr-Universität Bochum*, vol. A(56), Der Andere Verlag.

Kemna, A., J. A. Huisman, E. Zimmermann, R. Martin, Y. Zhao, A. Treichel, A. Flores Orozco, and T. Fechner (2014), Broadband electrical impedance tomography for subsurface characterization using improved corrections of electromagnetic coupling and spectral regularization, in Tomography of the Earths Crust: From Geophysical Sounding to Real-Time Monitoring, *Advanced Technologies in Earth Sciences*, vol. 21, edited by M. Weber and U. Münch, pp. 1–20, Springer International Publishing, doi:10.1007/978-3-319-04205-3_1.

Kemna, A., J. Vanderborght, B. Kulessa, and H. Vereecken (2002), Imaging and characterisation of subsurface solute transport using electrical resistivity tomography ERT and equivalent transport models, Journal of Hydrology, 267(3-4), 125–146, doi:10.1016/S0022-1694(02)00145-2.

Kenkel, J., A. Hördt, and A. Kemna (2012), 2D modelling of induced polarization data with anisotropic complex conductivities, Near Surface Geophysics, 10(6), 533–544, doi:10.3997/1873-0604.2012050.

Kenkel, J., R. Martin, and A. Kemna (2013), Anisotropic inversion of induced polarization (IP) data, Near Surface Geoscience 2013 – 19th European Meeting of Environmental and Engineering Geophysics, Bochum, Germany, doi:10.3997/2214-4609.20131433.

Klotzsche, A., J. van der Kruk, G. Meles, and H. Vereecken (2012), Crosshole GPR full-waveform inversion of waveguides acting as preferential flow paths within aquifer systems, Geophysics, 77(4), H57–H62, doi:10.1190/geo2011-0458.1.

Knight, R. (2001), Ground penetrating radar for environmental applications, Annual Review of Earth and Planetary Sciences, 29(1), 229–255, doi:10.1146/annurev.earth.29.1.229.

Knight, R., P. Tercier, and J. Irving (2004), The effect of vertical measurement resolution on the correlation structure of a ground penetrating radar reflection image, Geophysical Research Letters, 31(21), L21607, doi:10.1029/2004GL021112, 2004.

Koestel, J., A. Kemna, M. Javaux, A. Binley, and H. Vereecken (2008), Quantitative imaging of solute transport in an unsaturated and undisturbed soil monolith with 3-D ERT and TDR, Water Resources Research, 44(12), W12411, doi:10.1029/2007WR006755.

Koestel, J., J. Vanderborght, M. Javaux, A. Kemna, A. Binley, and H. Vereecken (2009a), Noninvasive 3-D transport characterization in a sandy soil using ERT: 1. Investigating the validity of ERT-derived transport parameters, Vadose Zone Journal, 8(3), 711–722, doi:10.2136/vzj2008.0027.

Koestel, J., J. Vanderborght, M. Javaux, A. Kemna, A. Binley, and H. Vereecken (2009b), Noninvasive 3-D transport characterization in a sandy soil using ERT: 2. Transport process inference, Vadose Zone Journal, 8(3), 723–734, doi:10.2136/vzj2008.0154.

Köhne, J. M., S. Köhne, and J. Šimůnek (2009a), A review of model applications for structured soils: a) Water flow and tracer transport, Journal of Contaminant Hydrology, 104(1-4), 4–35, doi:10.1016/j.jconhyd.2008.10.002.

Köhne, J. M., S. Köhne, and J. Šimůnek (2009b), A review of model applications for structured soils: b) Pesticide transport, Journal of Contaminant Hydrology, 104(1-4), 36–60, doi:10.1016/j.jconhyd.2008.10.003.

Köhne, J. M., and B. P. Mohanty (2005), Water flow processes in a soil column with a cylindrical macropore: Experiment and hierarchical modeling, Water Resources Research, 41(3), W03010, doi:10.1029/2004WR003303.

LaBrecque, D., D. L. Alumbaugh, X. Yang, L. Paprocki, and J. Brainard (2002), Three-dimensional monitoring of vadose zone infiltration using electrical resistivity tomography and cross-borehole ground-penetrating radar, in Three-

Dimensional Electromagnetics, Proceedings of the Second International Symposium, *Methods in Geochemistry and Geophysics*, vol. 35, edited by M. S. Zhdanov and P. E. Wannamaker, pp. 259–272, Elsevier, doi:10.1016/S0076-6895(02)80097-X.

LaBrecque, D. J., M. Miletto, W. Daily, A. Ramirez, and E. Owen (1996), The effects of noise on occam's inversion of resistivity tomography data, Geophysics, 61(2), 538–548, doi:10.1190/1.1443980.

Lamy, E., L. Lassabatere, B. Bechet, and H. Andrieu (2009), Modeling the influence of an artificial macropore in sandy columns on flow and solute transfer, Journal of Hydrology, 376(3-4), 392–402, doi:10.1016/j.jhydrol.2009.07.048.

Loke, M. H., J. E. Chambers, D. F. Rucker, O. Kuras, and P. B. Wilkinson (2013), Recent developments in the direct-current geoelectrical imaging method, Journal of Applied Geophysics, 95, 135–156, doi:10.1016/j.jappgeo.2013.02.017.

Luo, L., H. Lin, and P. Halleck (2008), Quantifying soil structure and preferential flow in intact soil using X-ray computed tomography, Soil Science Society of America Journal, 72(4), 1058–1069, doi:10.2136/sssaj2007.0179.

Luo, L., H. Lin, and S. Li (2010), Quantification of 3-D soil macropore networks in different soil types and land uses using computed tomography, Journal of Hydrology, 393(1-2), 53–64, doi:10.1016/j.jhydrol.2010.03.031.

McCarthy, J. F. (1991), Analytical models of the effective permeability of sand-shale reservoirs, Geophysical Journal International, 105(2), 513–527, doi:10.1111/j.1365-246X.1991.tb06730.x.

Meadows, D. G., M. H. Young, and E. V. McDonald (2005), A laboratory method for determining the unsaturated hydraulic properties of soil peds, Soil Science Society of America Journal, 69(3), 807–815, doi:10.2136/sssaj2004.0191.

Michot, D., Y. Benderitter, A. Dorigny, B. Nicoullaud, D. King, and A. Tabbagh (2003), Spatial and temporal monitoring of soil water content with an irrigated corn crop cover using surface electrical resistivity tomography, Water Resources Research, 39(5), 1138, doi:10.1029/2002WR001581.

Mooney, S. J., and C. Morris (2008), A morphological approach to understanding preferential flow using image analysis with dye tracers and X-ray computed tomography, Catena, 73(2), 204–211, doi:10.1016/j.catena.2007.09.003.

Moran, C. J., and A. B. McBratney (1992a), Acquisition and analysis of three-component digital images of soil pore structure. I. Method, Journal of Soil Science, 43(3), 541–549, doi:10.1111/j.1365-2389.1992.tb00159.x.

Moran, C. J., and A. B. McBratney (1992b), Acquisition and analysis of three-component digital images of soil pore structure. II. Application to seed beds in a fallow management trial, Journal of Soil Science, 43(3), 551–566, doi:10.1111/j.1365-2389.1992.tb00160.x.

Moysey, S. M. J., and Z. Liu (2012), Can the onset of macropore flow be detected using electrical resistivity measurements?, Soil Science Society of America Journal, 76(1), 10–17, doi:10.2136/sssaj2010.0413.

Mualem, Y. (1976), A new model for predicting the hydraulic conductivity of unsaturated porous media, Water Resources Research, 12(3), 513–522, doi:10.1029/WR012i003p00513.

Müller, K., J. Vanderborght, A. Englert, A. Kemna, J. A. Huisman, J. Rings, and H. Vereecken (2010), Imaging and characterization of solute transport during two tracer tests in a shallow aquifer using electrical resistivity tomography and multilevel groundwater samplers, Water Resources Research, 46(3), W03502, doi:10.1029/2008WR007595.

Murai, T., and Y. Kagawa (1985), Electrical impedance computed tomography based on a finite element model, IEEE Transactions on Biomedical Engineering, BME-32(3), 177–184, doi:10.1109/TBME.1985.325526.

Nimmer, R. E., J. L. Osiensky, A. M. Binley, K. F. Sprenke, and B. C. Williams (2007), Electrical resistivity imaging of conductive plume dilution in fractured rock, Hydrogeology Journal, 15(5), 877–890, doi:10.1007/s10040-007-0159-z.

Oberdörster, C., J. Vanderborght, A. Kemna, and H. Vereecken (2010), Investigating preferential flow processes in a forest soil using time domain reflectometry and electrical resistivity tomography, Vadose Zone Journal, 9(2), 350–361, doi:10.2136/vzj2009.0073.

Olsen, P. A., A. Binley, S. Henry-Poulter, and W. Tych (1999), Characterizing solute transport in undisturbed soil cores using electrical and X-ray tomographic methods, Hydrological Processes, 13(2), 211–221, doi:10.1002/(SICI)1099-1085(19990215)13:2<211::AID-HYP707>3.0.CO;2-P.

Pain, C. C., J. V. Herwanger, J. H. Saunders, M. H. Worthington, and C. R. E. de Oliveira (2003), Anisotropic resistivity inversion, Inverse Problems, 19(5), 1081–1111, doi:10.1088/0266-5611/19/5/306.

Pelton, W. H., S. H. Ward, P. G. Hallof, W. R. Sill, and P. H. Nelson (1978), Mineral discrimination and removal of inductive coupling with multifrequency IP, Geophysics, 43(3), 588–609, doi:10.1190/1.1440839.

Perret, J., S. O. Prasher, A. Kantzas, K. Hamilton, and C. Langford (2000), Preferential solute flow in intact soil columns measured by SPECT scanning, Soil Science Society of America Journal, 64(2), 469–477, doi:10.2136/sssaj2000.642469x.

Rea, J., and R. Knight (1998), Geostatistical analysis of ground-penetrating radar data: A means of describing spatial variation in the subsurface, Water Resources Research, 34(3), 329–339, doi:10.1029/97WR03070.

Renard, P., and G. de Marsily (1997), Calculating equivalent permeability: a review, Advances in Water Resources, 20(5-6), 253–278, doi:10.1016/S0309-1708(96)00050-4.

Richards, L. A. (1931), Capillary conduction of liquids through porous mediums, Physics, 1(5), 318–333, doi:10.1063/1.1745010.

Ritzi, R. W. J. (2000), Behavior of indicator variograms and transition probabilities in relation to the variance in lengths of hydrofacies, Water Resources Research, 36(11), 3375–3381, doi:10.1029/2000WR900139.

Samouëlian, A., I. Cousin, A. Tabbagh, A. Bruand, and G. Richard (2005), Electrical resistivity survey in soil science: a review, Soil and Tillage Research, 83(2), 173–193, doi:10.1016/j.still.2004.10.004.

Schlumberger, C., M. Schlumberger, and E. G. Leonardon (1934), Some observations concerning electrical measurements in anisotropic media and their interpretation, Transactions of the American Institute of Mining Engineers, 100, 159–182.

Schmoldt, J.-P., and A. G. Jones (2013), A novel anisotropic inversion approach for magnetotelluric data from subsurfaces with orthogonal geoelectric strike directions, Geophysical Journal International, 195(3), 1576–1593, doi:10.1093/gji/ggt355.

Simpson, M. J., A. J. Simpson, D. Gross, M. Spraul, and W. L. Kingery (2007), ^{1}H and ^{19}F nuclear magnetic resonance microimaging of water and chemical distribution in soil columns, Environmental Toxicology and Chemistry, 26(7), 1340–1348, doi:10.1897/06-478R.1.

Šimůnek, J., N. J. Jarvis, M. T. van Genuchten, and A. Gärdenäs (2003), Review and comparison of models for describing non-equilibrium and preferential flow and transport in the vadose zone, Journal of Hydrology, 272(1-4), 14–35, doi:10.1016/S0022-1694(02)00252-4.

Šimůnek, J., M. T. van Genuchten, and M. Šejna (2008), Development and applications of the HYDRUS and STANMOD software packages and related codes, Vadose Zone Journal, 7(2), 587–600, doi:10.2136/vzj2007.0077.

Slater, L., A. Binley, R. Versteeg, G. Cassiani, R. Birken, and S. Sandberg (2002), A 3D ERT study of solute transport in a large experimental tank, Journal of Applied Geophysics, 49(4), 211–229, doi:10.1016/S0926-9851(02)00124-6.

Slater, L., A. M. Binley, W. Daily, and R. Johnson (2000), Cross-hole electrical imaging of a controlled saline tracer injection, Journal of Applied Geophysics, 44(2-3), 85–102, doi:10.1016/S0926-9851(00)00002-1.

Slater, L. D., A. Binley, and D. Brown (1997), Electrical imaging of fractures using ground-water salinity change, Groundwater, 35(3), 436–442, doi:10.1111/j.1745-6584.1997.tb00103.x.

Teles, V., F. Delay, and G. de Marsily (2004), Comparison of genesis and geostatistical methods for characterizing the heterogeneity of alluvial media: Groundwater flow and transport simulations, Journal of Hydrology, 294(1-3), 103–121, doi:10.1016/j.jhydrol.2003.11.041.

Teles, V., F. Delay, and G. de Marsily (2006), Comparison of transport simulations and equivalent dispersion coefficients in heterogeneous media generated by different numerical methods: A genesis model and a simple geostatistical sequential gaussian simulator, Geosphere, 2(5), 275–286, doi:10.1130/GES00034.1.

van Genuchten, M. T. (1980), A closed-form equation for predicting the hydraulic conductivity of unsaturated soils, Soil Science Society of America Journal, 44(5), 892–898, doi:10.2136/sssaj1980.03615995004400050002x.

Vanderborght, J., P. Gähwiller, and H. Flühler (2002), Identification of transport processes in soil cores using fluorescent tracers, Soil Science Society of America Journal, 66(3), 774–787, doi:10.2136/sssaj2002.7740.

Vanderborght, J., A. Kemna, H. Hardelauf, and H. Vereecken (2005), Potential of electrical resistivity tomography to infer aquifer transport characteristics from tracer studies: A synthetic case study, Water Resources Research, 41(6), W06013, doi:10.1029/2004WR003774.

Vervoort, R. W., S. R. Cattle, and B. Minasny (2003), The hydrology of vertosols used for cotton production: I. Hydraulic, structural and fundamental soil properties, Australian Journal of Soil Research, 41(7), 1255–1272, doi:10.1071/SR02154.

Wagner, F. M., M. Möller, C. Schmidt-Hattenberger, T. Kempka, and H. Maurer (2013), Monitoring freshwater salinization in analog transport models by timelapse electrical resistivity tomography, Journal of Applied Geophysics, 89, 84–95, doi:10.1016/j.jappgeo.2012.11.013.

Wen, X.-H., and J. J. Gómez-Hernández (1996), Upscaling hydraulic conductivities in heterogeneous media: An overview, Journal of Hydrology, 183(1-2), ix–xxxii, doi:10.1016/S0022-1694(96)80030-8.

Winchen, T., A. Kemna, H. Vereecken, and J. A. Huisman (2009), Characterization of bimodal facies distributions using effective anisotropic complex resistivity: A 2D numerical study based on Cole-Cole models, Geophysics, 74(3), A19–A22, doi:10.1190/1.3113986.

Yeh, T.-C. J. (1992), Stochastic modelling of groundwater flow and solute transport in aquifers, Hydrological Processes, 6(4), 369–395, doi:10.1002/hyp.3360060402.

Zaher, H., J. Caron, and B. Ouaki (2005), Modeling aggregate internal pressure evolution following immersion to quantify mechanisms of structural stability, Soil Science Society of America Journal, 69(1), 1–12, doi:10.2136/sssaj2005.0001.

Zimmermann, E. (2010), Phasengenaue impedanzspektroskopie und -tomographie für geophysikalische anwendungen, Ph.D. thesis, University of Bonn.

Zimmermann, E., J. A. Huisman, W. Glaas, and S. van Waasen (2013), Fast EIT data acquisition for geophysical applications, 7th World Congress on Industrial Process Tomography, Kraków, Poland.

Zimmermann, E., A. Kemna, J. Berwix, W. Glaas, H. M. Münch, and J. A. Huisman (2008a), A high-accuracy impedance spectrometer for measuring sediments with low polarizability, Measurement Science and Technology, 19(10), 105603, doi:10.1088/0957-0233/19/10/105603.

Zimmermann, E., A. Kemna, J. Berwix, W. Glaas, and H. Vereecken (2008b), EIT measurement system with high phase accuracy for the imaging of spectral induced polarization properties of soils and sediments, Measurement Science and Technology, 19(9), 094010, doi:10.1088/0957-0233/19/9/094010.

Zisser, N., and G. Nover (2009), Anisotropy of permeability and complex resistivity of tight sandstones subjected to hydrostatic pressure, Journal of Applied Geophysics, 68(3), 356–370, doi:10.1016/j.jappgeo.2009.02.010.

Sadam Al-Hazaimay

Jan-von-Werth-Str. 82
52428 Jülich, Germany
℘ (+49) 159 0307 8352
✉ sadam1hazaimay@gmail.com

Curriculum Vitae

RESEARCH INTERESTS

Environmental Physics

Hydrogeophysics and Hydrogeology

Preferential Flow Processes in Vadose Zone

Geophysical Tomography and Inversion Techniques

PROFESSIONAL AND RESEARCH EXPERIENCE

Institute of Bio- & Geosciences IBG3, Agrosphere, Forschungszentrum Jülich GmbH, Germany

Oct. 2009 –
March 2013

Research Assistant, Research Group "Vadose Zone Hydrogeophysics".
- Planning and implementation laboratory experiments.
- Development and validation of coupled hydrological-electrical models in 2D and 3D.
- Monitoring and imaging temporal dynamics of macro-anisotropy.
- Data error quantification analysis.

Institute of Environmental Physics IUP, University of Bremen, Germany

Dec. 2007 –
Aug. 2008

Master's Internship/Student Job, Research Group "Fourier Transform InfraRed (FTIR) Spectrometer".
- Conducting measurement spectra using FTIR spectrometer.
- Compiling database and analyzing data.

Ministry of Education MOE, Jordan

Sep. 2003 –
Oct. 2006

Teaching and Laboratory Assistant.
- Teaching physics and general science courses.
- Supervising students' assignments and homework.
- Assisting students' lab work.
- Teaching proper laboratory safety and procedures.
- Experience in public speaking and varied presentation skills.

EDUCATION

Oct. 2009 – June 2015	**PhD in Hydrogeophysics**, *Faculty of Georesources and Materials Engineering*, RWTH Aachen University, Germany.
Title	Using the anisotropy of electrical properties for the characterization of sedimentological structures and preferential flow processes.
Supervisor	Prof. Dr. Johan A. Huisman, Agrosphere Institute IBG3, Forschungszentrum Jülich GmbH, Germany.
Oct. 2006 – Aug. 2008	**MSc in Environmental Physics**, *Institute of Environmental Physics IUP*, University of Bremen, Germany.
Title	Impact of instrumental parameters on atmospheric trace gases retrievals using fourier transform infrared spectrometry.
Supervisor	Prof. Dr. Justus Notholt, Institute of Environmental Physics IUP, University of Bremen, Germany.
Oct. 1998 – July 2002	**BSc in Physics**, *Department of Physics*, Yarmouk University, Jordan.

PUBLICATIONS IN REVIEW & PREPARATION

Al-Hazaimay S., J.A. Huisman, E. Zimmermann, and H. Vereecken. Using electrical anisotropy for structural characterization of sediments: An experimental validation study. Manuscript submitted to Near Surface Geophysics.

Al-Hazaimay S., J.A. Huisman, E. Zimmermann, and H. Vereecken. Investigating preferential flow processes in soils using anisotropy in electrical resistivity. Manuscript submitted to Vadose Zone Journal.

Al-Hazaimay S., J. Kenkel, E. Zimmermann, A. Kemna, H. Vereecken, and J.A. Huisman. Imaging of electrical anisotropy associated with macropore infiltration processes: A 2D laboratory experiment with an artificial macropore. Manuscript will be submitted to Vadose Zone Journal.

ABSTRACTS AT INTERNATIONAL MEETINGS

March 2013	**Al-Hazaimay S.**, Huisman J. A., Zimmermann E., Kemna A., and Vereecken H., *Using the anisotropy of electrical resistivity for the characterization of preferential flow processes*, TR32 International Symposium, Abstract P4-12. Bonn, Germany, March 11-14, 2013.
Dec. 2012	**Al-Hazaimay S.**, Huisman J. A., Zimmermann E., Kemna A., and Vereecken H., *Investigating preferential flow processes in soils using anisotropy in electrical resistivity*, AGU Fall Meeting, Abstract H53I-1640. San Francisco, US, Dec. 3-7, 2012.
April 2012	**Al-Hazaimay S.**, Huisman J. A., Zimmermann E., Kemna A., and Vereecken H., *Investigating preferential flow processes in soils using anisotropy in electrical resistivity*, Joint Workshop HOBE/TR32. Sandbjerg, Denmark, April 1-4, 2012.
March 2012	**Al-Hazaimay S.**, Huisman J. A., Zimmermann E., Kemna A., and Vereecken H., *Electrical anisotropy for the characterization of preferential flow in soil*, German Geophysical Society (DGG), Abstract EM-1.007. Hamburg, Germany, March 4-8, 2012.

April 2011	**Al-Hazaimay S.**, Huisman J. A., Zimmermann E., Kemna A., and Vereecken H., *Using electrical anisotropy for sub-scale structural characterization of sediments: an experimental validation study*, EGU General Assembly, Abstract EGU2011-7347. Vienna, Austria, April 3-8, 2012.
Oct. 2010	Haegel F. H., Zimmermann E., Jablonowski N. D., Linden A., Esser O., **Al-Hazaimay S.**, Huisman J. A., and Vereecken H., *Investigations on Sand-Carbon Mixtures with Spectral Induced Polarisation and Electrical Impedance Tomography*, IP Workshop. Machern, Germany, Oct. 5-6, 2010.

TRAINING

Aug. 2010 – March 2013	**Lecture Series, Integrated Research Training Group (IRTG)**.
	Graduate School, Sonderforschungsbereich Transregio 32, German Research Foundation Project.
	Forschungszentrum Jülich GmbH, RWTH-Aachen University, University of Cologne, and University of Bonn, Germany.
Sep. 2012	**Introductory Statistics Course**.
Instructor	Mort Canty.
	Agrosphere Institute, Forschungszentrum Jülich GmbH, Germany.
March 2012	**How to Write and Publish a Scientific Paper**.
Instructor	Prof. Markus Flury, Washington State University, US.
	Agrosphere Institute, Forschungszentrum Jülich GmbH, Germany.
Nov. 2011	**Writing Scietific Skills**.
Instructor	Anne Wagner.
	University of Cologne, Germany.

LANGUAGES

English	Fluent written and spoken
German	Very good written and spoken
Arabic	Mother tongue

COMPUTER SKILLS

	Certificate of International Computer Driving License (ICDL)
Expert knowledge	Microsoft Windows Operating System (all current and legacy versions), Microsoft Office Professional suite (Word, PowerPoint, Excel, Outlook), MATLAB, HYDRUS, LaTex, Surfer (Golden Software), Endnote & JabRef
Basic knowledge	Linux Operating System (Ubuntu), Microsoft Office Professional suite (Access), CorelDRAW & Inkscape, High Performance & Parallel Computing, Paraview, Octave, Python

EXTRAS

German Driving License, Class B

Annual Safety Work Instructions in Field and Laboratory, Forschungszentrum Jülich GmbH, Germany.

First-Aid Course, Forschungszentrum Jülich GmbH, Germany and Camping Activities, Jordan.

EXTRACURRICULAR ACTIVITIES

2002	The 25th Meeting for the Arab Scouts, Arab Scout Organization, Jordan.
2000	Golden Award, El-Hassan Youth Award, Jordan.
July/Aug. 2000	Adventurer Certificate, Sabelat El-Hassan, Jordan.

- Helping in a scientific research of environmental projects.
- Offering services to villages and providing social interactions.
- Participating in adventurous programs.

Nov. 1999	The First National Meeting of Scouts, Society of Scouts and Guides, Jordan.
April/May 1999	Police Friends Course, Yarmouk University, Jordan.
Dec. 1998	Assistant of Scouts Unit Leader, Athletic Activity Department, Yarmouk University, Jordan.

Band / Volume 274
Thermochemical Modeling of Laves Phase Containing Ferritic Steels
A. Jacob (2015), 200 pp
ISBN: 978-3-95806-070-8

Band / Volume 275
**Lithiumbatterien für stationäre und mobile Anwendungen:
Benchmarking und experimentelle Umsetzung**
T. Bergholz (2015), vi, 387 pp
ISBN: 978-3-95806-071-5

Band / Volume 276
Pyrochlore as nuclear waste form: actinide uptake and chemical stability
S. C. Finkeldei (2015), IX, 155 pp
ISBN: 978-3-95806-072-2

Band / Volume 277
**Herstellung von Elektrodenstrukturen für Lithium-Ionen-
Dünnschichtbatterien**
A. Bünting (2015), v, 151 pp
ISBN: 978-3-95806-073-9

Band / Volume 278
**Keramiken des Monazit-Typs zur Immobilisierung
von minoren Actinoiden und Plutonium**
J. M. Heuser (2015), viii, 212 pp
ISBN: 978-3-95806-076-0

Band / Volume 279
**IEK-3 Report 2015
Systems Research and Engineering for a Sustainable Energy Supply**
(2015)
ISBN: 978-3-95806-077-7

Band / Volume 280
**IEK-3 Report 2015
Systemforschung und –technik für eine nachhaltige Energieversorgung**
(2015)
ISBN: 978-3-95806-078-4

Band / Volume 281
Integration of the German energy transition in the EU-context
A. Ernst (2015), 76 pp
ISBN: 978-3-95806-079-1

JÜLICH
FORSCHUNGSZENTRUM